Petrotectonic Evolution of Ledge Mountain Migmatites, Adirondack Highlands, New York

A Thesis submitted to the faculty of
San Francisco State University
In partial fulfillment of
the requirements for
the Degree

Master of Science

In

Geosciences

by

Michael Wesley Davis

San Francisco, California

May 2021

Certification of Approval

I certify that I have read Petrotectonic Evolution of Ledge Mountain Migmatites, Adirondack Highlands, New York by Michael Wesley Davis, and that in my opinion this work meets the criteria for approving a thesis submitted in partial fulfillment of the requirement for the degree Master of Science in Geoscience at San Francisco State University.

_____

Mary Leech, Ph.D.
Professor,
Thesis Committee Chair

_____

Yadira Ibarra, Ph.D.
Professor

_____

Ellen Metzger, Ph.D.
Professor

Petrotectonic Evolution of Ledge Mountain Migmatites, Adirondack Highlands, New York

Michael Wesley Davis
San Francisco, California
2021

Ledge Mountain migmatites exposed in the Adirondack Highlands, an outlier of the Grenville province, are a part of a classic granulite terrane and represent deep crustal rocks that form modern orogenic roots. This study provides a multifaceted methodology involving detailed petrographic analysis and extensive thermodynamic modeling using Perple_X to reveal a metamorphic history with significantly higher peak P-T conditions than those determined by classical thermobarometry from elsewhere in the region. Ultrahigh-temperature granulite-facies peak metamorphic P-T conditions of 11-18 kbar and ≥960°C are determined using the intersection of peritectic garnet compositions from five samples and garnet isopleth models. Water content is determined to be ~0.12 wt. % based on hydrous mineral volume and T-M_{H2O} modeling. Thermodynamic models test possible protolith compositions and water content to determine whether lower temperature conditions would be produced; all model configurations generate UHT metamorphic conditions. Modeling reveals that 10% to 44% melt may have been produced and subsequently lost during the prograde history. To account for melt loss, prograde compositions are estimated by reintegrating a modeled melt composition back into the bulk composition. A melt-reintegrated pseudosection reveals stable mineral assemblages along the prograde path that are consistent with observed microtextures and melt inclusions within peritectic garnet. From peak conditions, the retrograde path follows a near isothermal decompression path followed by near isobaric cooling to retrograde conditions of 6.5-8 kbar and ~750°-850°C. These retrograde metamorphic conditions align with those reported in other studies as peak metamorphic conditions. This modeling methodology may reveal a hidden P-T history not captured elsewhere in the Adirondack Highlands, and may be applicable more widely to the Grenville province or other orogens containing felsic migmatites.

Acknowledgements

I am extremely grateful to my advisor Dr. Mary Leech for her continuous support, encouragement, and feedback while attaining my masters. She challenged me regularly, pushed me to share my work with others on national stages, and encouraged me to pursue my own ideas to their fullest extent. I would also like to thank Dr. Ellen Metzger for her many contributions to this work and for her collaboration on many Zoom calls. Thank you to Dr. Yadira Ibarra for proofreading and allowing me to use her scanning microscope that was crucial to being able to perform analyses during COVID. Finally, thank you to my fiancé Chrissy for her unwavering encouragement and emotional support over the past two years.

Table of Contents

Certification of Approval iii

Acknowledgements v

Table of Contents vi

List of Tables viii

List of Figures ix

List of Appendices x

Introduction 1

Background 3
- Grenville Province 3
- Adirondack Mountains 4
- Ledge Mountain 9
  - Regional Setting 9
  - Previous Thermobarometry 9

Migmatite Terminology 11

Migmatite Descriptions and Textures 13

Mineralogy and Petrology 21
- Mineralogy and Petrology Methods 22
  - Thin Section Scans and Mineral Mode Analysis 22
  - Electron Microscopy 22
- Melanosome 24
- In-Source Leucosome 31
- Leucocratic Veins 39

Mineral Chemistry 41
- Garnet 41
- Feldspar 45
- Biotite 47

Fe-Ti Oxides 49

Phase Equilibria Modeling 51
Whole Rock Geochemistry 51
Pseudosection Models 51
H_2O content 52
Solution Model Selections 55
Ferric (Fe_2O_3) and Ferrous (FeO) Oxide Content 56
Mineral Isopleths 58
Pseudosection Topologies 58
Estimated Peak conditions 60
Melt Reintegration 67

P-T Path 71

Net-transfer Reactions Along the P-T Path 73
Prograde Net-Transfer Reactions 73
Near-isothermal Decompression Net-transfer Reactions 75
Near-isobaric Cooling Net-transfer Reactions 75

Zircon Analyses 79
Previous Geochronology 79
Ti-in-Zrn Thermometry 79

Discussion 87
Protolith Age and Composition 87
Timing of Metamorphism 88
Timing of Biotite Growth 89
Peak P-T conditions 90
Melting and Crystallization Sequence 91
Prograde Path 91
Near Isothermal Decompression 91
Near Isobaric Cooling 92
Exhumation of a Central Adirondack Gneiss Dome 93
Comparison to other Collisional Orogens and Thermodynamic Models 96

Conclusion 98

References 99

List of Tables

Table 1. Mineral Percentages of Representative Samples 21
Table 2: Kanaya-Okayama Ranges of Select Minerals 24
Table 3. Grossular Content Statistics 62
Table 4. Whole-Rock Data for Samples Used in Model Calculation of the Average Pseudosection Diagram in Figure 24. 65
Table 5. Melt-Reintegration Composition 69
Table 6: Summary of U-Th-Pb SHRIMP Geochronology and Ti-in-Zrn Thermometry of Ledge Mountain Zircons 83
Table 7: Summary of Sensitivities of T_c, Error, and Percentage of Error Contributions. 117

List of Figures

Figure 1. Geologic Map of the Adirondack Highlands 4
Figure 2: Zircon U-Pb Geochronology of Major Units in the Adirondack Highlands 8
Figure 3: In-source Leucosome Adjacent to Melanosome 15
Figure 4: Leucocratic Vein Adjacent to Host Neosome 18
Figure 5: Leucocratic Vein Within Host Neosome 19
Figure 6: Mineral Proportions Within Melanosome 26
Figure 7. Minerals within Opaque Phases 28
Figure 8. Large Garnet in Melanosome 30
Figure 9. Relict Rutile in Garnet 31
Figure 10. Minerals in Leucosome 33
Figure 11. Two Generations of Sillimanite in Leucosome 34
Figure 12. Garnet Breakdown in Leucosome 35
Figure 13. Garnet Breakdown Products within Leucosome Channels 36
Figure 14. Sillimanite, Ilmenite, Hercynite in Leucosome 38
Figure 15. Minerals in Leucocratic Vein 40
Figure 16. Garnet Composition Diagram 42
Figure 17. Mineral Zoning in Garnet 43
Figure 18. Compositional Zoning of Selected Garnet Grains 44
Figure 19. Feldspar Composition Diagram 46
Figure 20. Biotite Composition Diagram 48
Figure 21. Spinel Composition Diagram 50
Figure 22. Water Content 54
Figure 23. Pseudosections of Select Samples with Grossular Isopleths 63
Figure 24. Variation of Peak Fields by Water Content, Comparing Igneous and Metapelitic Model Sets 66
Figure 25. Proposed P-T Path through Prograde and Retrograde Pseudosections 72
Figure 26. Melt and Recrystallization Sequence the along P-T-t path 77
Figure 27: Ti-in-zircon temperatures (° C) vs. age (Ma) for different zircon domains. 86

List of Appendices

Appendix A: Kanaya-Okayama Ranges 108

Appendix B: Methodology for Zircon Analysis (from Metzger et al., in press) 109

Appendix C: Ti-in-Zircon Thermometry Error Analysis 113

Introduction

Ledge Mountain migmatites in the Adirondack Highlands in New York record metamorphic pressure-temperature (P-T) conditions during their petrotectonic evolution. Thermodynamic models reveal the P-T conditions at which observed mineral phase transitions and microstructures occurred during the prograde-, peak-, and retrograde-metamorphic history of Ledge Mountain migmatites. Determining the P-T paths at Ledge Mountain has implications for the evolution of the Adirondack Highlands and Grenville Province, thus improving our understanding of the geologic history of this classic granulite terrane (Chiarenzelli and McLelland, 1991; McLelland et al., 2001, 2004, 2013; Bickford et al., 2008; Rivers, 2009; McLelland and Selleck, 2011; Valentino et al., 2019). Previous studies involving classic thermobarometry place peak P-T conditions at 6.5-9 kbar and ~750°-850° C between upper amphibolite- and granulite-facies (Bohlen, 1987; Florence and Spear, 1995; Spear and Markussen, 1997; Storm and Spear, 2005). Several verified reports of kyanite at Ledge Mountain indicate higher pressures at eclogite-facies/high-pressure granulite-facies conditions (Boone, 1978; Metzger et al., in press). Recent studies involving thermobarometry, diffusion models, and thermodynamic modeling of nearby Gore Mountain (~30 km East of Ledge Mountain) suggests ultrahigh temperature (UHT) metamorphism (Shinevar et al., 2020).

Ledge Mountain is mapped as a granulite basement complex (Geraghty, 1978) while at least 22 vol% partial melting of the host rock indicates Ledge Mountain rocks are migmatites (Metzger et al., in press). To determine the origin and evolution of Ledge Mountain migmatites, I determine peak and retrograde P-T conditions, investigate protolith composition, and

approximate a prograde path using a combination of thermodynamic modeling, petrographic and microstructural analysis, and electron microprobe analysis of mineral compositions. To approximate the prograde path, I reintegrate melt into an average whole-rock composition of Ledge Mountain using a method similar to other melt-reintegration studies (Connolly, 2009; Groppo et al., 2012; Bartoli, 2017).

Background

Grenville Province

The Grenville orogenic belt developed during the assembly of the Rodinia supercontinent and contains middle- to lower-crustal rocks likely exhumed during regional extension associated with collapse of a large, hot orogen (Figure 1A; Rivers, 2012; 2015). Rocks in the Grenville Province experienced two major tectonic events: The Shawinigan (1200-1140 Ma; McLelland et al., 2013; Valentino et al., 2019) and Grenville (1090-980 Ma; Bickford et al., 2008; Rivers, 2009; McLelland et al., 2013) orogens.

The Shawinigan phase was characterized by early subduction of oceanic crust and detachment of the subducting slab, closure of a back-arc basin, intrusion of an anorthosite–mangerite–charnockite–granite (AMCG) plutonic suite and other granitic units, and late orogenic collapse (McLelland et al., 2013; Valentino et al., 2019a; Aleinikoff et al., 2021).

The Grenville orogeny occurred as two separate orogenic events. The earlier Ottawan phase (1090-1020 Ma) involved a contraction phase (1090-1050 Ma), where Amazonia thrusted over Laurentia during the assembly of Rodinia resulting in granulite-facies metamorphism (McLelland et al., 2001; Rivers, 2009), and an extensional phase (1050-1020 Ma) during orogenic collapse and rapid cooling (Figure 1; Wong et al., 2012; Chiarenzelli et al., 2017; Peck et al., 2018; Regan et al., 2019b; Williams et al., 2019). The Rigolet phase (1010-980 Ma), had significant impact in the western Grenville Province but minimal impact in the Adirondacks (Rivers, 2009; Williams et al., 2019).

Figure 1. Geologic Map of the Adirondack Highlands

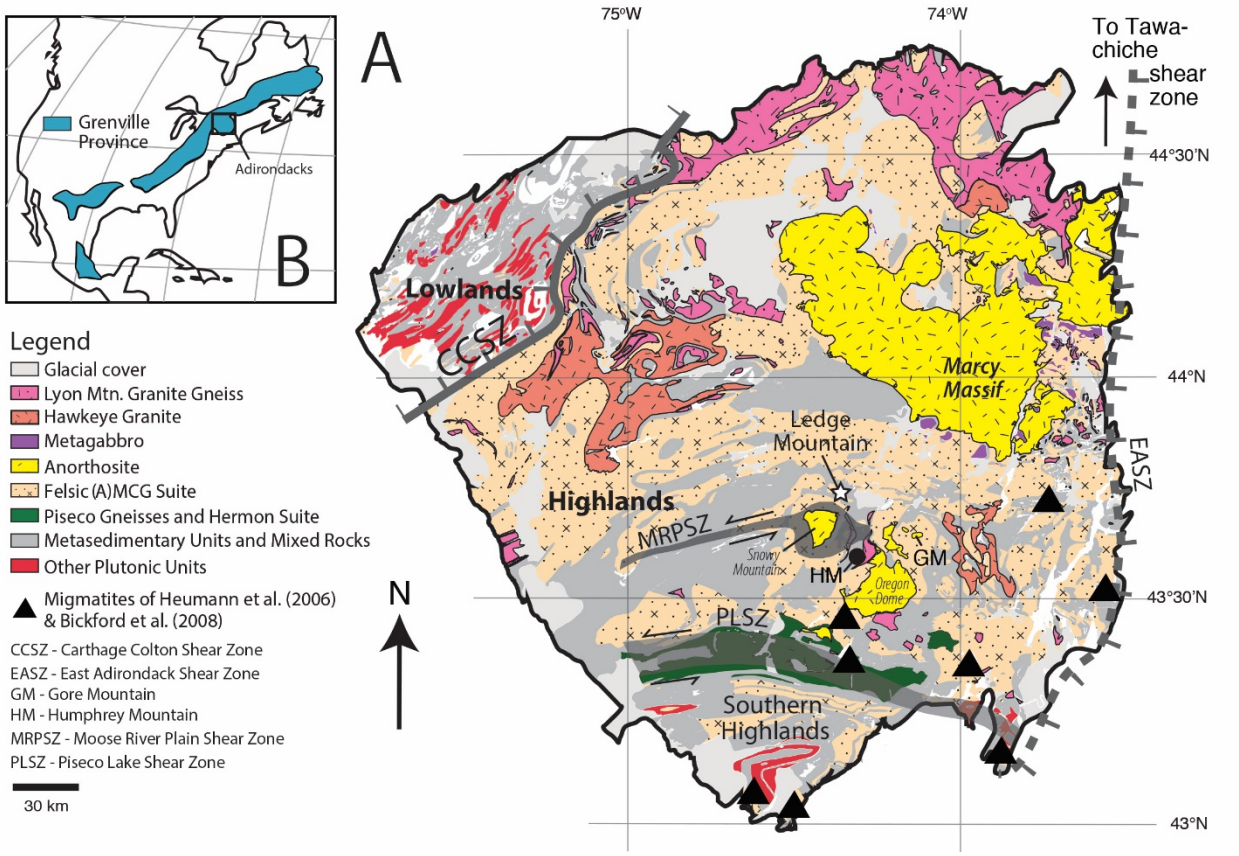

Figure 1. (A) A geologic map of the Adirondack Highlands showing major units, structures, and shear zones, and (B) its context location in the larger Grenville Province. Ledge Mountain (star) is in the central part of the highlands north of the MRPSZ and Snowy Mountain anorthosite. Modified from Wong et al. (2012) *and Peck et al., 2013.*

Adirondack Mountains

The Adirondack Mountains represent the lower plate of a double-thickened crust, which developed along a major crustal-scale thrust system (East Adirondack Shear Zone; Figure 1) during the collision of Laurentia with Amazonia (Spear and Markussen, 1997; McLelland et al., 2001; Rivers, 2009). The Adirondack Mountains are divided into two zones - the Adirondack Highlands and the Adirondack Lowlands - that are separated by the Carthage-Colton shear zone

that dips 45° to the northwest (Figure 1A; Streepey et al., 2001). The Lowlands represent the orogenic lid which overlaid the Highlands prior to the Ottawan when their juxtaposition was facilitated by Carthage-Colton shear zone. The higher topography of the Highlands compared to the Lowlands is controlled by both structure, as normal faulting surrounds the highlands, and lithology, as the Highlands consist of granulite-facies rocks that are more resistant to erosion than the metasedimentary rocks that make up the Lowlands. The Piseco Lake Shear Zone separates the Highlands into the Southern Adirondack terrane and the Adirondack Highlands (Figure 1A; Valentino et al., 2019).

The oldest rocks in the Highlands are 1350-1250 Ma tonalitic and granitic plutons in the southern Adirondacks which may have may have rifted from a 1400-1300 Ma Laurentian margin arc (McLelland et al., 2013). Metasedimentary units in the Adirondack Lowlands and Highlands were deposited 1300-1220 Ma on opposite sides of a back-arc basin and then juxtaposed during the Shawinigan (~1180 Ma), with timing based on ages of detrital zircon (Heumann et al., 2006; McLelland et al., 2013).

The most widespread feature in the Adirondack Highlands is the 1150 Ma AMCG suite derived from mantle or crustal rocks (Figure 1A). Much of the AMCG suite contains only felsic mangerite-charnockite-granite (MCG) components while the largest of the anorthosite domains include the Marcy massif, Oregon dome, and Snowy Mountain dome. Most studies determined crystallization ages of the AMCG plutonic suite in the Highlands at 1165-1140 Ma based on U-Pb zircon SHRIMP analysis (Figure 2; Storm and Spear, 2005; Bickford et al., 2008; Indares et al., 2008; Rivers, 2009; McLelland et al., 2013; Regan et al., 2019; Valentino et al., 2019; Aleinikoff et al., 2021).

The Marcy massif anorthosite dome that dominates the central Adirondack Highlands (crystallization at ~1155 Ma; Peck et al., 2018; Valentino et al., 2019) metamorphosed to peak P-T conditions of 6.5-8 kbar and ~850° C (Spear and Markussen, 1997; Peck et al., 2018) during the early Ottawan orogeny (~1070 Ma; Isachsen et al., 2004; Peck et al., 2018). In-situ monzonite U-Th-Total Pb geochronology of rocks from the Marcy massif detachment zone constrains deformation/exhumation to 1070-1060 Ma (Regan et al., 2019b), while garnet growth continued during rapid cooling from 1050-1035 Ma (Figure 2; Peck et al., 2018).

The Hawkeye Granite Gneiss and Lyon Mountain Granite Gneiss are widespread plutonic units in the Adirondack Highlands (Figure 1A; Postel, 1952; McLelland et al., 1996). Published zircon U-Pb SHRIMP and zircon multi-grain thermal ionization mass spectrometry (TIMS) geochronology of igneous zircon cores leave emplacement ages of intrusive units open to interpretation (McLelland et al., 1988; 2001; Chiarenzelli and McLelland, 1991; Selleck et al., 2005; Bickford et al., 2008; Aleinikoff and Walsh, 2015; Buchanan, 2015; Chiarenzelli et al., 2015; Aleinikoff, 2017). Studies by Chiarenzelli and McLelland (1991) conclude that the strongly deformed Hawkeye Granite Gneiss was emplaced 1100 – 1095 Ma, just prior to the Ottawan orogeny based on TIMS U-Pb analyses. The weakly deformed Lyon Mountain Granite Gneiss, which cross-cuts the Hawkeye Granite Gneiss, intruded 1060 – 1040 Ma during Ottawan according to evidence from SHRIMP analyses of zircon rims (McLelland et al., 2001; Selleck et al., 2005; Chiarenzelli et al., 2017). These studies interpret the zircons cores with age of 1160 – 1140 Ma as inherited from metaigneous country rock (i.e., AMGC suite plutonic rocks; McLelland et al., 2001; Selleck et al., 2005; Chiarenzelli et al., 2017). In contrast to the purely Ottawan ages of previous studies, Aleinikoff et al. (2021) determine a much earlier Shawinigan

emplacement for the Hawkeye Granite Gneiss at 1160-1155 Ma and Lyon Mountain Granite Gneiss 1150-1145 Ma, coeval with emplacement of AMCG plutonic rocks (Figure 2). Aleinikoff et al. (2021) also interpret ~1090-980 Ma zircon rims in both the Hawkeye Granite Gneiss and Lyon Mountain Granite Gneiss as metamorphic in origin, rather than igneous, and formed during multiple pulses during the Ottawan and Rigolet

Figure 2: Zircon U-Pb Geochronology of Major Units in the Adirondack Highlands

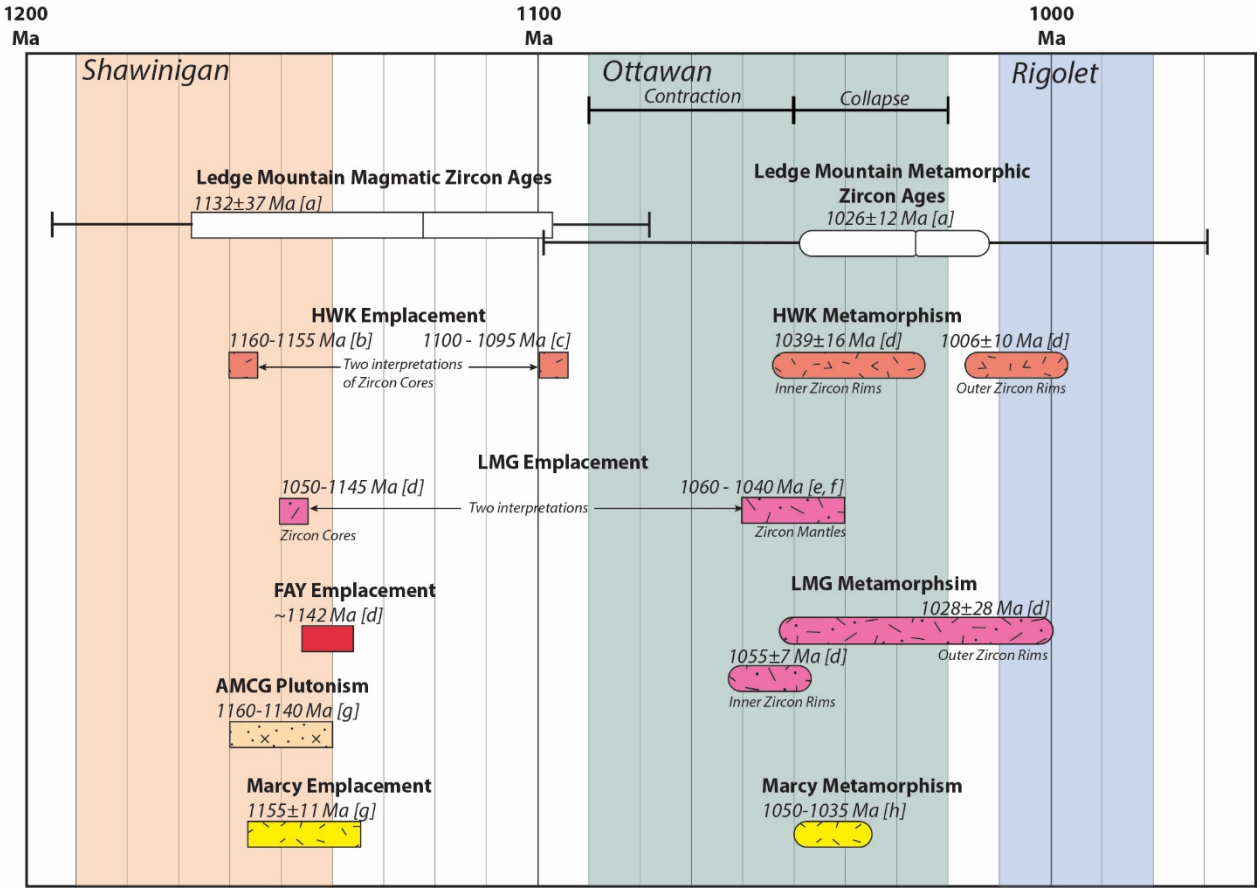

Figure 2. Timing of igneous crystallization and metamorphism for different units in the Adirondack Highlands based on U-Pb zircon geochronology. Orogenic phases are shaded in orange (Shawinigan), green (Ottawan), and blue (Rigolet). There are multiple interpretations of igneous emplacement timings for HWK and LMG. Timing of metamorphism of all units is consistent with occurring during extensional collapse. ***Rectangles****: Ages interpreted to represent igneous crystallization.* ***Capsule shapes****: Ages interpreted to represent metamorphism.* ***Abbreviations****: HWK - Hawkeye Granite Gneiss; LMG – Lyon Mountain Granite Gneiss; FAY – fayalite granite; AMCG – Anorthosite-Margarite-Charnockite-Granite; Marcy – Marcy anorthosite massif. References: [a] Reeder, 2017; [b] Aleinikoff et al., 2021; [c] McLelland et al., 1996; [d] Aleinikoff and Walsh, 2015; [e] Chiarenzelli et al., 2017; [f] Selleck et al., 2005; [g] McLelland et al., 2004; [h] Peck et al., 2018.*

Ledge Mountain

Regional Setting

Ledge Mountain is located between the Moose River plain shear zone and Marcy anorthosite massif in the near geographic center of the Central Highlands, a few kilometers north of the Snowy Mountain anorthosite dome (Figure 1). The Moose River plain shear zone intersects and is deflected by the Snowy Mountain anorthosite. The foliation on the flanks of the Snowy Mountain dome dip concentrically away from the dome center (Gates et al., 2004). The foliations to the north of Snowy Mountain dome extend as at least as far north as Ledge Mountain. Foliations continue to the west of Snowy Mountain within the Moose River plain shear zone (Gates et al., 2004). The region has been deformed by several folds (Geraghty, 1978; Metzger, 1980) and migmatites exposed at Ledge Mountain are surrounded by marble in the core of a recumbent antiform (Figure 1; Geraghty, 1978).

Previous Thermobarometry

Previous studies based on classical thermobarometry estimate metamorphic P-T conditions of 600-850° C and 6-9 kbar for the Adirondack Highlands (McLelland et al., 2013). Boone (1978) applied garnet -aluminosilicate – silica – plagioclase (GASP) barometry and garnet-biotite exchange thermometry to Ledge Mountain rocks to calculate metamorphic conditions of 695°C-700°C and 7.2-8.2 kbar. Early studies involving two-feldspar and Fe-Ti oxide solvus thermometry determine metamorphic temperatures of 700˚ to 750˚C throughout most of the Highlands, and temperatures of 750˚ to 800˚C near the Marcy massif (Bohlen and

Essene, 1977; Bohlen et al., 1980). Florence and Spear (1995) use garnet-biotite thermometry to determine a retrograde metamorphic temperature of 700˚C in the southern Highlands. Thermodynamic modeling with petrographic analysis determined metamorphic temperatures of at least 790˚C in highly retrogressed rocks in the southern Highlands (Storm and Spear, 2005). The highest previously-reported temperatures (~800–850° C at 7-8 kbar) center on the Marcy anorthosite massif in the central Adirondack Highlands (Figure 1) with later metamorphic garnet growth in the anorthosite taking place at lower temperatures (~750-650° C; Spear and Markussen, 1997; Peck et al., 2018). Shinevar et al., (2020) recently reported UHT conditions (950±40° C/8.5-10 kbar) for garnet amphibolite at Gore Mountain (Figure 1) based on thermobarometry, thermodynamic modeling, and diffusion models.

Migmatite Terminology

Migmatites are partially melted metamorphic rocks consisting of two parts: *neosome* represents partially melted portions of the rock, and *paleosome* represents the non-neosome rocks that did not partially melt (Sawyer, 2008). Rocks referred to as "protolith" in my later discussions are precursors to the neosome and are not found *in situ* with migmatites because the protolith partially melted during migmatization. However, protolith analogues may exist externally to migmatite domains in places where P-T conditions did not reach temperatures high enough to cause migmatization. While *protolith* and *paleosome* are both non-partially melted units, the paleosome is often a different, more melt resilient portion of the migmatite with a different composition than the protolith (Sawyer, 2008).

Neosome is further divided into *melanosome*, the more mafic residuum part of the rock that remains after melt has been separated, and *leucosome*, the product of crystallization of anatectic melt that has segregated from its source (Sawyer, 2008). Three types of leucosome are defined to indicate the degree to which melt has separated from residua:

1) *In situ leucosome* has segregated from its residuum but remains at the site where the melt formed (Sawyer, 2008). Contacts between leucosome and melanosome are mm- to cm-scale and diffuse. The bulk rock composition which includes *in situ* leucosome, and its source melanosome represents the original protolith composition if no melt has been lost. If some melt has been lost, then there should be excess residuum relative to the leucosome, and the bulk rock composition represents a melt-depleted protolith composition.

2) *In-source leucosome* has migrated away from its own residuum but remains within its source layer, and contacts between leucosome and melanosome can be diffuse or sharp (Sawyer,

2008). The melanosome adjacent to in-source leucosome is of similar composition to the residuum host, but it is not an exact complement because the host may have melted to a different degree or experienced more or less melt loss than the adjacent melanosome.

3) A *leucocratic vein* typically has sharp contacts and is the recrystallized product of melt that has migrated out of its source layer and was injected into another rock but is still in the region affected by the anatectic event (Sawyer, 2008).

Migmatites can also contain granitic, tonalitic, pegmatitic, or trondhjemitic dikes or sills, or other products of crystallization of a felsic melt that has migrated from its source region completely and is injected into its host rock. These injections usually form sharp contacts and have no petrogenetic relationship with their host rock (Sawyer, 2008).

Migmatite Descriptions and Textures

Thirty-eight samples of Ledge Mountain were collected and include samples of neosome containing in-situ and in-source leucosome and their host melanosome, veins of pegmatitic material and their contact with the host migmatite, and a meta-leucotonalite. Typical Ledge Mountain migmatite is a tan to pink, fine- to medium-grained, and weakly foliated to granoblastic leucocratic gneiss. Quartz, alkali feldspar, and plagioclase are the dominant minerals and vary in their relative proportions. Sillimanite, garnet, biotite, and oxide minerals typically each make up less than 5% of the rock. In places, quartzofeldspathic layers alternate with lenses and layers of sillimanite-quartz that weather in positive relief and, where present, define a foliation. The proportions of sillimanite-quartz concentrations vary, in some locations making up 15-30% of the outcrop and decrease in abundance from west to east across Ledge Mountain (Boone, 1978; McLelland et al., 1978; Metzger, 1980; Swanson, 2019). Migmatite domains are recognized by changes in microtextures, fabric, and grain-size, in addition to subtle changes in minerals modes across domains.

Ledge Mountain neosome contains a weakly foliated, granoblastic melanosome that is enriched in biotite, iron-titanium (Fe-Ti) oxides, and feldspars relative to the surrounding or intermingled leucosome (Figures 3-5).

A typically fine-grained (<1 mm) melanosome coarsens up to ~1-2 mm near veins of recrystallized melt (samples 825, 17LM06, 008B, and 17LM10) and hosts in-situ leucosome, in-source leucosome, and leucocratic veins. In-situ and/or in-source leucosome consisting primarily of quartz and aligned sillimanite form ~0.5-3 cm-wide channels within fine-grained neosome (Figure 3), except for in sample 17LM10 where these channels pervade medium grained

melanosome. Fe-Ti oxides and biotite are usually present in small amounts, but are locally concentrated (Figure 4). Contact with the host melanosome is diffuse and forms channels that traverse entire thin sections, terminate within a thin section, or are lenses completely contained within a thin section. Small lenses of leucosome formed *in-situ,* but longer channels may be *in-situ* if the material came directly from the adjacent melanosome or in-source if the material migrated away from its source along the channel. In either case, *in-situ* or in-source leucosome are compositional derivatives of the surrounding source melanosome (Sawyer, 2008).

Figure 3: In-source Leucosome Adjacent to Melanosome

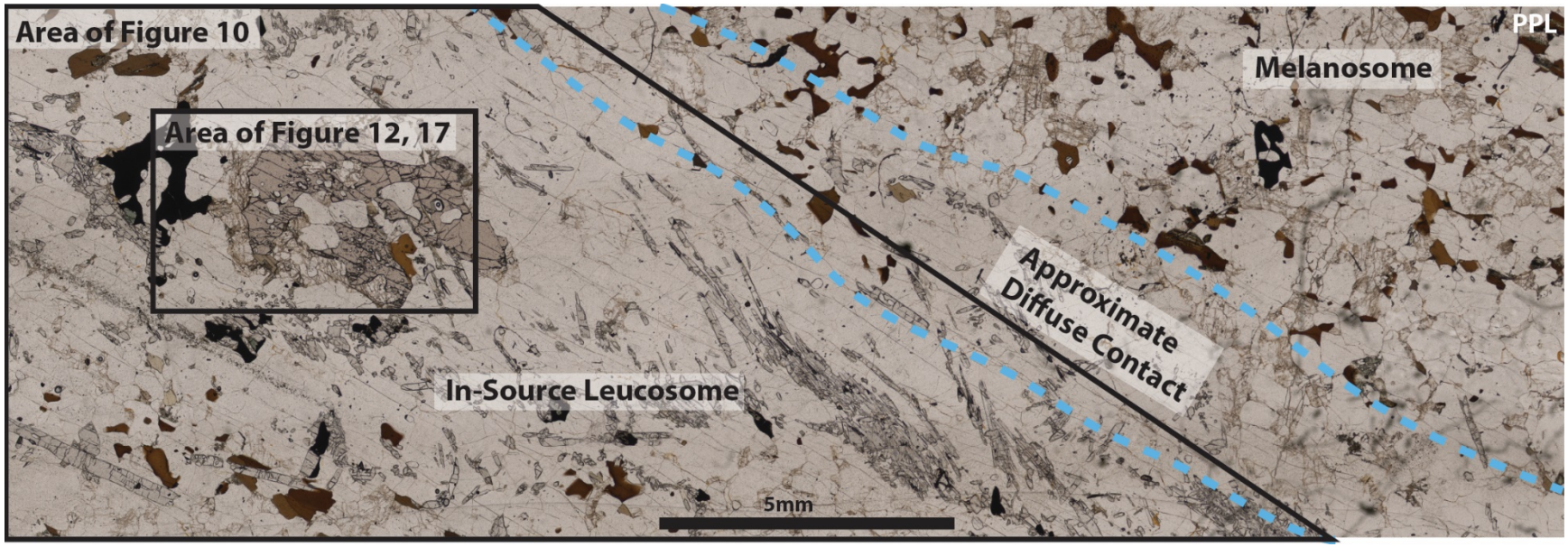

Figure 3. Example of in source leucosome adjacent to melanosome from sample AD-01. The image shows in-source leucosome, host melanosome, and their shared diffuse contact (scanned in PPL). Leucosome contains aligned, fibrolitic sillimanite with accessory feldspar, biotite, gahnite-hercynite series spinel, and opaque minerals in a quartz-dominant matrix. A ~5mm grain of peritectic garnet is shown in compositional x-ray maps in Figures 12 and 17 and a phase map highlighting leucosome minerals is shown in Figure 10. Melanosome contains more biotite and opaque minerals than leucosome.

Largely non-deformed veins of pegmatite-like material composed mainly of large quartz and perthitic K-feldspar crystals (>0.5 mm) is in sharp, concordant contact with the weakly foliated, quartzofeldspathic neosome host. These veins range from 18 cm to 1.8 m in thickness and extend for up to 6 m where they become obscured in the field. Without the ability to trace these veins to their source rock, determining their genetic relationship to the host is difficult. If these veins are the product of crystallization of anatectic melt that migrated out of its source layer but remain in the region that was affected by the anatectic melt, then they should be called *leucocratic veins* (Sawyer, 2008). If the material is a felsic melt that was injected into the host from out of its source region then it should be called a *pegmatite* (Sawyer, 2008). Because pegmatites are injected into cool hosts, they often have fine-grained boarder zones or *chilled margins* (Sawyer, 2008) – a feature that is not observed in any thin sections from Ledge Mountain. Furthermore, there are no crosscutting relationships between the *in-situ/*in-source leucosome and the leucocratic veins, which may indicate that they formed simultaneously. Thus, while these veins and the host neosome have no direct petrogenetic relationship, the age of crystallization of both vein and host are consistent, and the correct term is a *leucocratic vein* (Sawyer, 2008). Leucocratic veins likely intruded from a nearby source outside of the host rock that also experienced the same anatectic event.

Leucocratic veins differ compositionally from the in-situ and/or in-source leucosome described previously, because they contain more K-feldspar, are coarser grained, rarely contain sillimanite, and display sharp contact with the host neosome. Coarse rims of mafic material termed “selvages” (Sawyer, 2008) often form between the leucocratic veins and host neosome. Three main mechanisms for the formation of selvages include (1) reaction with the fluid

exsolved from the leucocratic vein as it crystalized, (2) reactions between minerals in the host and leucocratic vein, and (3) diffusion of components between melt and host (Sawyer, 2008). Selvages in Ledge Mountain rocks appear as 1-2 cm rims of biotite and Fe-Ti oxides that are deficient in quartz and feldspar compared to the host (Figure 4). Figure 4 shows grains of K-feldspar and plagioclase located at the edge of the leucocratic vein that appear to have grown across the biotite selvage. Sawyer (2008) interprets similar textures from migmatites in the Quentico Subprovince, Ontario, Canada, as late grain growth generated from redistribution of plagioclase as the mafic selvage formed. Some smaller leucocratic veins (~0.5-1 cm; Figure 5) contain ilmenite and biotite that might be neosome inclusions.

Figure 4: Leucocratic Vein Adjacent to Host Neosome

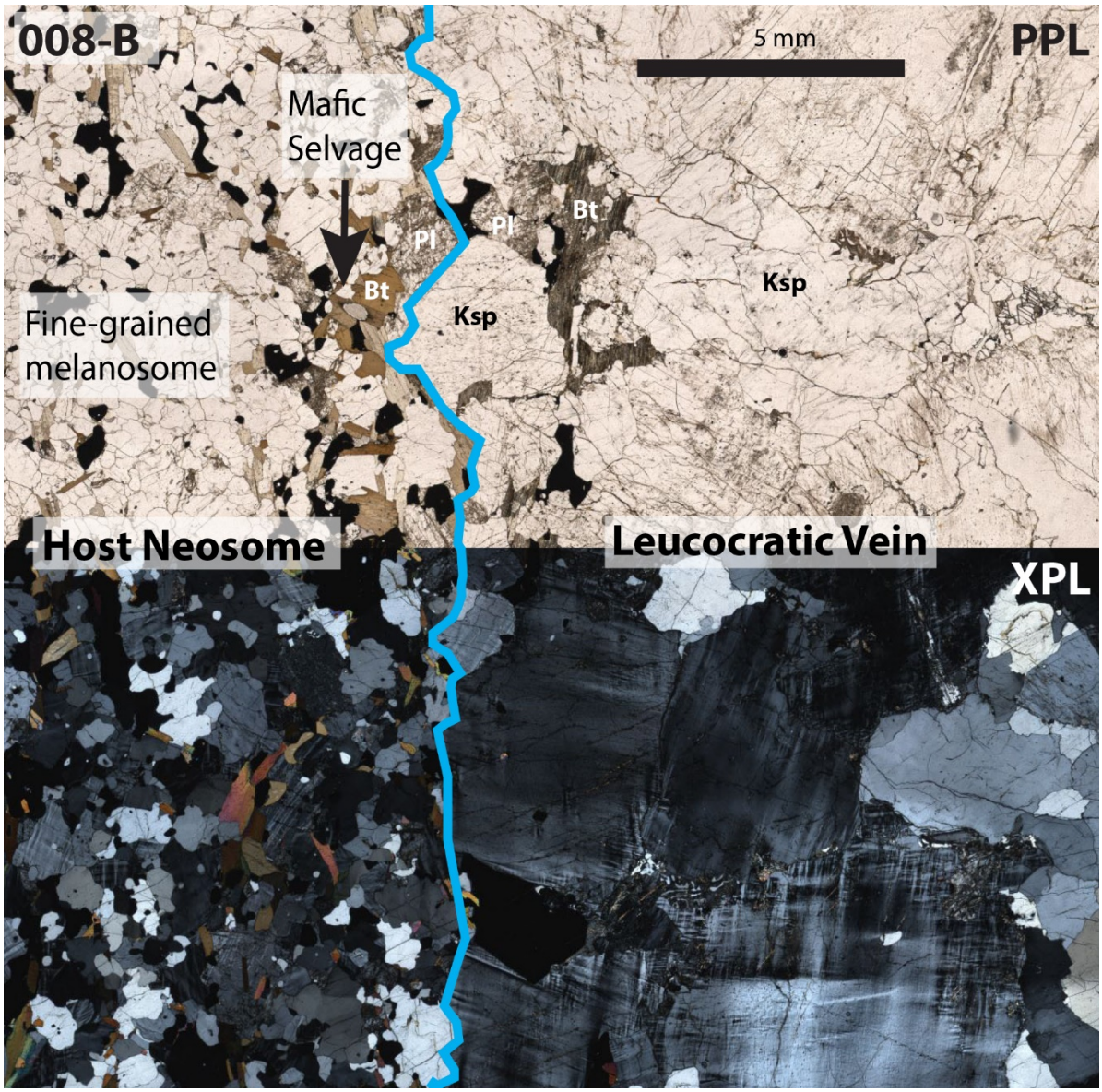

Figure 4. Scanned thin section (sample 008-B) showing the contact between a leucocratic vein and its host neosome. The image is continuous: the top half is shown in PPL and the bottom half is shown in XPL to highlight grain size differences. The host neosome shows the melanosome portion of the migmatite. A mafic selvage separates the neosome and Leucocratic vein, and indicates there was some interaction (diffusion or reaction) between minerals in the leucocratic vein and host (Sawyer, 2008). Abbreviations after Whitney and Evans (2010).

Figure 5: Leucocratic Vein Within Host Neosome

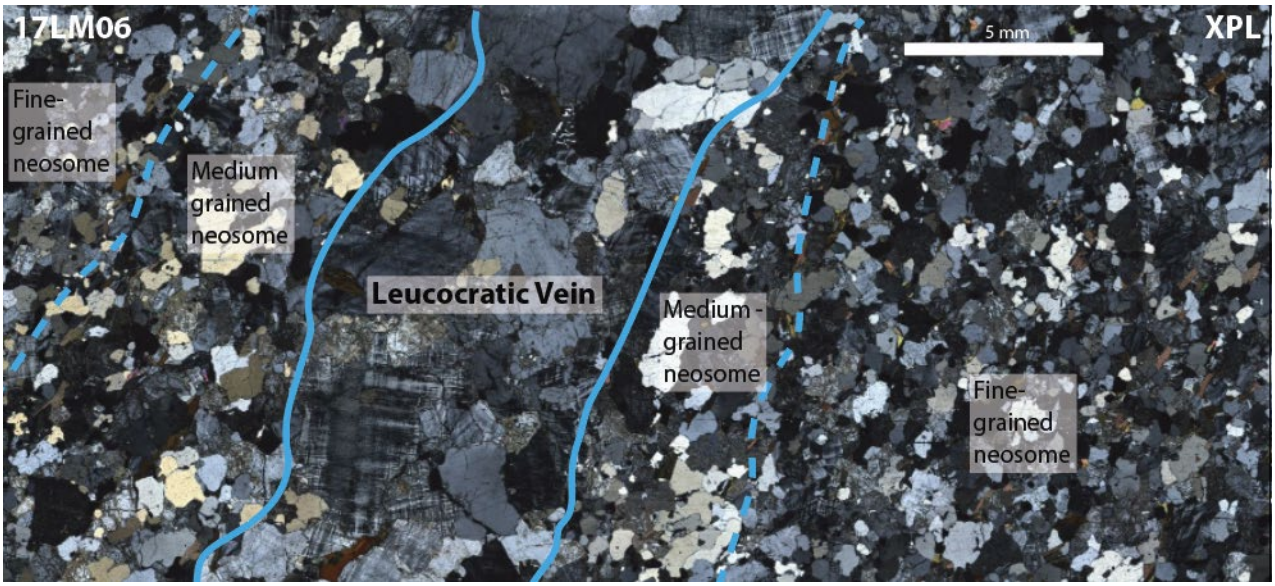

Figure 5. Scanned portion of a thin section showing a leucocratic vein within host neosome (sample 17LM06; XPL). A leucocratic vein with larger grain size cuts across finer-grained neosome. A ~2 mm zone of medium grain neosome borders the leucocratic vein.

Sample 5B has similar composition to the leucocratic veins except that it contains much more K-feldspar and larger grain sizes (>5 cm). The nature of the contact between this product of recrystallized melt and the host rock is obscured, so it is difficult to determine its genetic origin. Metzger (1980) identifies sample 5B as pegmatite body that is discordant to host foliation.

A ~12 x 6 m lens of white, coarse-grained leucotonalite with less than 1% biotite and garnet (sample 11) that differs from the rest of the outcrop was observed at one location (Metzger, 1980; Metzger et al., in press). Its contact with the surrounding rock is obscured, so its genetic relationship to the migmatite remains unclear. Pseudosection analysis (discussed later) shows this sample experienced P-T conditions similar to those of the host migmatite, suggesting this may be an enclave or inclusion that was emplaced before a shared anatectic event.

The outcrops exposed on Ledge Mountain are relatively small and the relationship between leucocratic veins and their source layers is obscured by weathering and vegetation. In some larger outcrops examined by Sawyer (2008), root zones of leucocratic veins show characteristic continuity from *in-situ* leucosome, through in-source leucosome, to the leucocratic veins. It is possible that the *in-situ* and in-source leucosome are petrogenetically related to the leucocratic veins at Ledge Mountain. In at least one thin section (17LM07B), in-source leucosome is concordant with a leucocratic vein, but the genetic relationship remains uncertain.

Mineralogy and Petrology

Microtextures and mineralogy vary within the migmatite domains at Ledge Mountain. Melanosome and leucosome contain abundant textural evidence of former melt and retrograde recrystallization. Across all domains, quartz, K-feldspar, and plagioclase feldspar dominate the mineral assemblage, except for in the meta-leucotonalite (sample 11), which lacks K-feldspar. To quantify the mineralogy of Ledge Mountain rocks, I used a combination of photomicrographs in PPL and XPL, backscattered electron (BSE) images, and electron microprobe analysis to measure the volume of individual phases. Mineralogy for representative samples from each domain is summarized in Table 1.

Table 1. Mineral Percentages of Representative Samples

	Melanosome 5-6	Melanosome 17LM06	Leucocratic Vein 17LM06	In source Leucosome AD01
Quartz (Qz)	62.5	45	31	72.1
Total Feldspar	28.7	48.4	66.7	9.3
Microcline (Ksp)	14.4	9.9	36.5	0.2
Plagioclase (Pl)	2.5	-	9.5	4.0
Feldspar (Ksp or Pl)	11.8	38.5	20.7	5.1
Sillimanite (Sil)	0	0	0	13.5
Mica (Bi, Ms, or Chl)	7.9	2.8	1.3	2.3
Opaques (Ilm, Mag, or Rt)	2	2.5	0.5	2.6
Hercynite-Gahnite Series Spinel (Hc)	0	0	0	0.2

Mineralogy and Petrology Methods

Thin Section Scans and Mineral Mode Analysis

Thin sections were scanned in ultra-high resolution (161 million dpi) in XPL and PPL using the Zeiss Axio Imager M2m optical microscope. To quantify the approximate mineral content in each migmatite domain, individual minerals from representative areas of several thin sections and different migmatite domains were traced and assigned a solid fill color by mineral type (i.e., all microcline was colored with light blue; e.g., Figure 6) in Adobe Illustrator. Opaque phases are not distinguishable with transmitted light microscopy, so are designated "opq" and mineral percentages are considered together. Biotite is often replaced by chlorite and muscovite, and so the percentages for these phases are also combined. Tartan twinning in microcline K-feldspar and polysynthetic "albite" twinning in plagioclase identify some feldspars, but without diagnostic twinning feldspars are indistinguishable and combined as "feldspar". I used ImageJ to calculate the precise area of each mineral-groups' color by adjusting the color thresholds of each color to select individual colors. Then I used the "analyze particles" tool to reveal the percent area occupied by each color (Table 1).

Electron Microscopy

I used electron microscopy to identify some minerals (e.g., Fe-Ti oxides, which appear opaque in visible light) and distinguish compositional zoning on the JEOL JXA-8239 "SuperProbe" electron microprobe at the Stanford University Mineral and Microchemical Analysis Facility. Operating conditions were 15 keV accelerating voltage and 15 nA beam

current with 20 seconds counting time. Backscattered Electron (BSE) images were captured using beam energy of 15keV and working distance of 11mm.

Any electron beam analysis requires careful consideration of the interaction depth (range) of the beam within the specimen. The Kanaya-Okayama (K-O) range gives the interaction depth for 99% of electrons entering the specimen and serves as a proxy for the interaction diameter on the specimen (Kanaya and Okayama, 1972). The K-O range, R, is given by

$$R = \frac{0.0276\ E^{1.67} A}{\rho Z^{0.889}}$$

[Equation 1]

where E is the electron beam energy, ρ is the sample density, A is the atomic weight, and Z is the weighted atomic number. The effective K-O ranges for quartz, feldspar, garnet, biotite, ilmenite, rutile, and magnetite are calculated in Table 2 and range from ~4 to 33 μm. These values are approximate as the inputs vary depending on exact mineral chemistry. Quartz, feldspar, garnet, and biotite grains are generally much larger than their K-O ranges, so their chemistries are accurate. Ilmenite, rutile, and magnetite have K-O ranges of ~5 – 10 μm, which is smaller than most grains, but needs consideration when examining thin lamellae or grains with similar or smaller dimensions. BSE provide Z-contrast imaging that depend on the average atomic number (A); BSE imaging reveals lamellae of different Fe-Ti oxide minerals in the opaque phases. Some lamellae are too fine to determine chemistry directly by the K-O range limitations of microprobe analysis, but Z-contrast can be used to confirm the chemistry of smaller layers or grains (Figure

7). The K-O ranges are the approximate diameters where gray areas in Z-contrast images can be considered accurate for a given mineral. For example, in Figure 7 the lighter linear features in the larger magnetite crystal, and darker features within the garnet are most likely due to cracks in those materials, rather than veins of rutile. Additionally, some of the speckled rims (colored dark blue in Figure 7D) around the Fe-Ti oxides minerals are likely due to edge effects, rather than being thin plagioclase halos. A detailed explanation of how K-O ranges can help to interpret Z-contrast in BSE images is provided in Appendix A.

Table 2: Kanaya-Okayama Ranges of Select Minerals

Mineral	Empirical Formula	ρ (g/cm^3)	A (g/mol)	Z	Range (μm)
Quartz	SiO_2	2.7	60.083	10	**7.1**
Feldspar	$Na_{0.5}Ca_{0.5}Si_3AlO_8$	2.6	270.77	10.3	**32.2**
Garnet (Almendine)	$Fe_3Al_2(SiO_4)_3$	4.1	450.45	12.1	**29.4**
Biotite	$KMg_{2.5}Fe_{0.5}AlSi_3O_{10}(OH)_{1.75}F_{0.25}$	3.1	433.53	36	**14.2**
Ilmenite	$FeTiO_3$	4.6	151.71	14.4	**7.6**
Rutile	TiO_2	4.2	79.88	12.7	**4.9**
Magnetite	Fe_3O_4	5.2	233.8	15.7	**9.6**

Melanosome

Melanosome is characterized by a granoblastic-to-weakly-foliated, fine-grained texture that grades to medium-grained near leucocratic veins (Figure 3-5). Melanosome is relatively homogenous at the scale of a single thin section, but mineral proportions vary between samples. The primary mineral assemblage of quartz + K-feldspar + plagioclase + biotite + Fe-Ti oxides contains accessory chlorite and muscovite, rare sillimanite and gahnite-hercynite series spinel,

and intermittent porphyritic garnet. Representative melanosome samples 5-6 and 17LM06 contain ~45-63% quartz, ~29-48% feldspar (Ksp + Pl) of which at least ~10-14% is K-feldspar, ~3-8% micas (mostly biotite), ~2-2.5% opaque minerals, and >0.1% hercynite-gahnite spinel and sillimanite (Table 1**;** abbreviations hereinafter from Whitney and Evans, 2010).

Figure 6: Mineral Proportions Within Melanosome

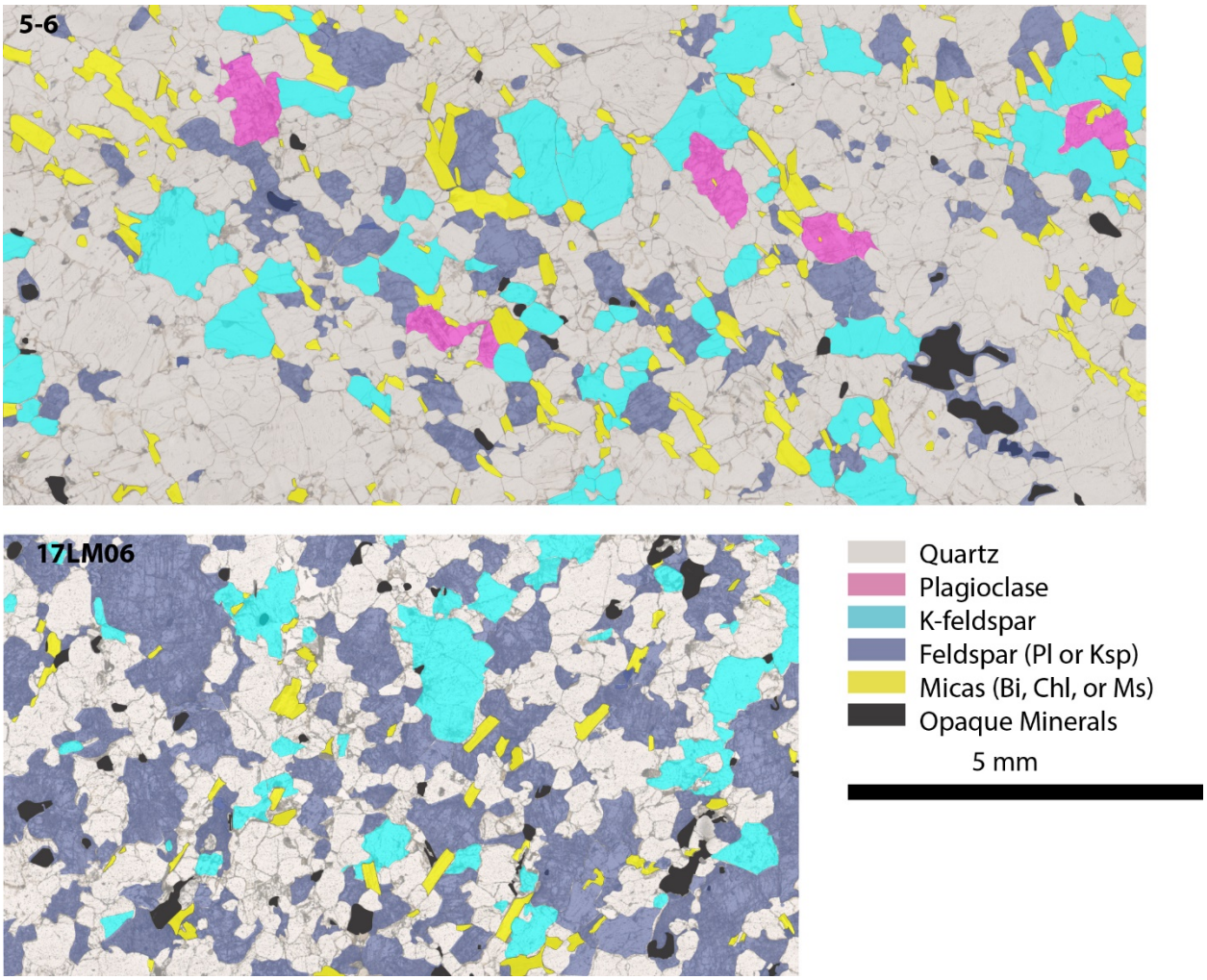

Figure 6: Phase maps overlain on thin sections scanned in PPL and used to quantify mineral modes in representative melanosome samples (samples 5-6 and 17LM06; Table 1). Quartz is not colored. Plagioclase (pink) is identified by albite twinning in XPL. Microcline (light blue) is identified by tartan twinning in XPL. Feldspar without diagnostic twinning (dark blue) could be plagioclase or K-feldspar. Micas (yellow) are mostly biotite with rare muscovite and chlorite.

Irregular quartz grains appear unaltered and display undulatory extinction. Anhedral K-feldspar is microcline because it displays tartan twinning. Anhedral to subhedral plagioclase

feldspar displays polysynthetic albite twins or is untwinned. K-feldspar and plagioclase also appear as rims around garnet and ilmenite, or as inclusions in garnet. Except for feldspar that displays diagnostic twinning, K-feldspar and plagioclase feldspars are texturally indistinguishable, but can be identified with microprobe analysis. Plagioclase grains verified by either microprobe analysis or diagnostic twinning are invariably altered by micaceous sericite. K-feldspar that forms rims around opaque minerals is also sericitized, but K-feldspar inclusions in garnet are not sericitized.

Biotite is easily distinguished in PPL by its brown color, pleochroism, and one perfect cleavage direction, and often exhibits bird's eye texture and parallel extinction. Biotite in the quartz and feldspar matrix is equigranular and euhedral. Biotite is also found as inclusions in feldspar and replacing garnet. Muscovite is rare and only appears with biotite. Both micas are often partially or fully replaced by chlorite.

Opaque minerals form subhedral to euhedral grains adjacent to feldspar and comprise inclusions in feldspar. BSE images reveal opaque minerals are intergrowths magnetite + ilmenite ± rutile in various proportions (Figure 7)**.** Films of K-feldspar and plagioclase often surround the opaque intergrowths -- a microstructure seen in experiments where partial melts are quenched and a thin border of melt-product separates the reactant phases (Figure 7; Sawyer, 2008). In very rare occurrences, hercynite-gahnite series spinel can be found in opaque phases in the melanosome. Fe-Ti-Al oxides exhibit complex intergrowths similar to those reported for UHT aluminous granulites from the Eastern Ghats Belt of India (Bose et al., 2009; Dasgupta et al., 2017).

Figure 7. Minerals within Opaque Phases

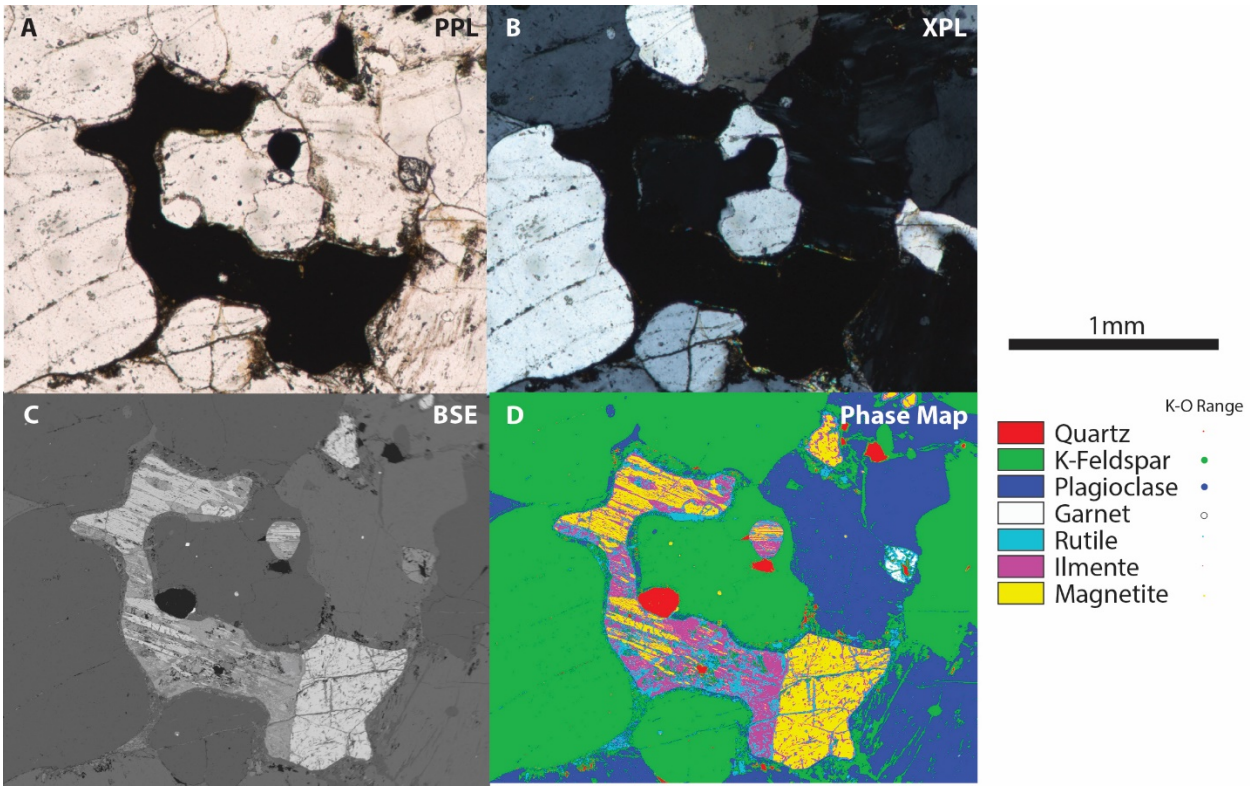

Figure 7. Mineral associations with opaque phases. Photo- and electron- micrographs captured in (A) PPL and (B) XPL, and with (C,D) BSE. D is a colored phase map based on shades of gray in the BSE image. Minerals are identified through a combination of petrographic analysis (quartz and garnet) and electron microprobe analysis (K-feldspar, plagioclase, rutile, ilmenite, and magnetite). Kanaya-Okayama (K-O) ranges are displayed graphically at the same scale as the micrographs. Colored areas smaller than their K-O ranges, or within their K-O range of another colored area, may not accurately identify their associated mineral.

Garnet is observed in all melanosome samples except 17LM03 and 17LM02. Garnet crystals in melanosome are heterogeneously distributed and vary in diameter from 0.1 cm to 2 cm. About 25% of garnet grains are <2 mm (<1 vol. %), 50% are 5 to 7 mm (15 vol. %), and 25% are >1 cm in diameter (85 vol. %). Except for the smallest grain sizes, melanosome garnet

appears as porphyroblasts, some which are aggregates of a few grains. Large poikiloblastic garnets (Figure 8) have monomineralic and polymineralic inclusions of biotite, quartz, feldspar, and Fe-Ti oxides. Quartz inclusions have rounded or lobate shapes. Sericitized feldspar often forms rims on garnet. Sillimanite inclusions are rare. Intergrowths of biotite + sillimanite + quartz + plagioclase often embay garnet edges. Lobate embayments and inclusions of quartz in garnet are consistent with peritectic garnet growth during dehydration melting (Figure 8; Waters, 2001; Groppo et al., 2012). Garnet also forms rims around rutile and opaque minerals (Figure 9**)**.

Figure 8. Large Garnet in Melanosome

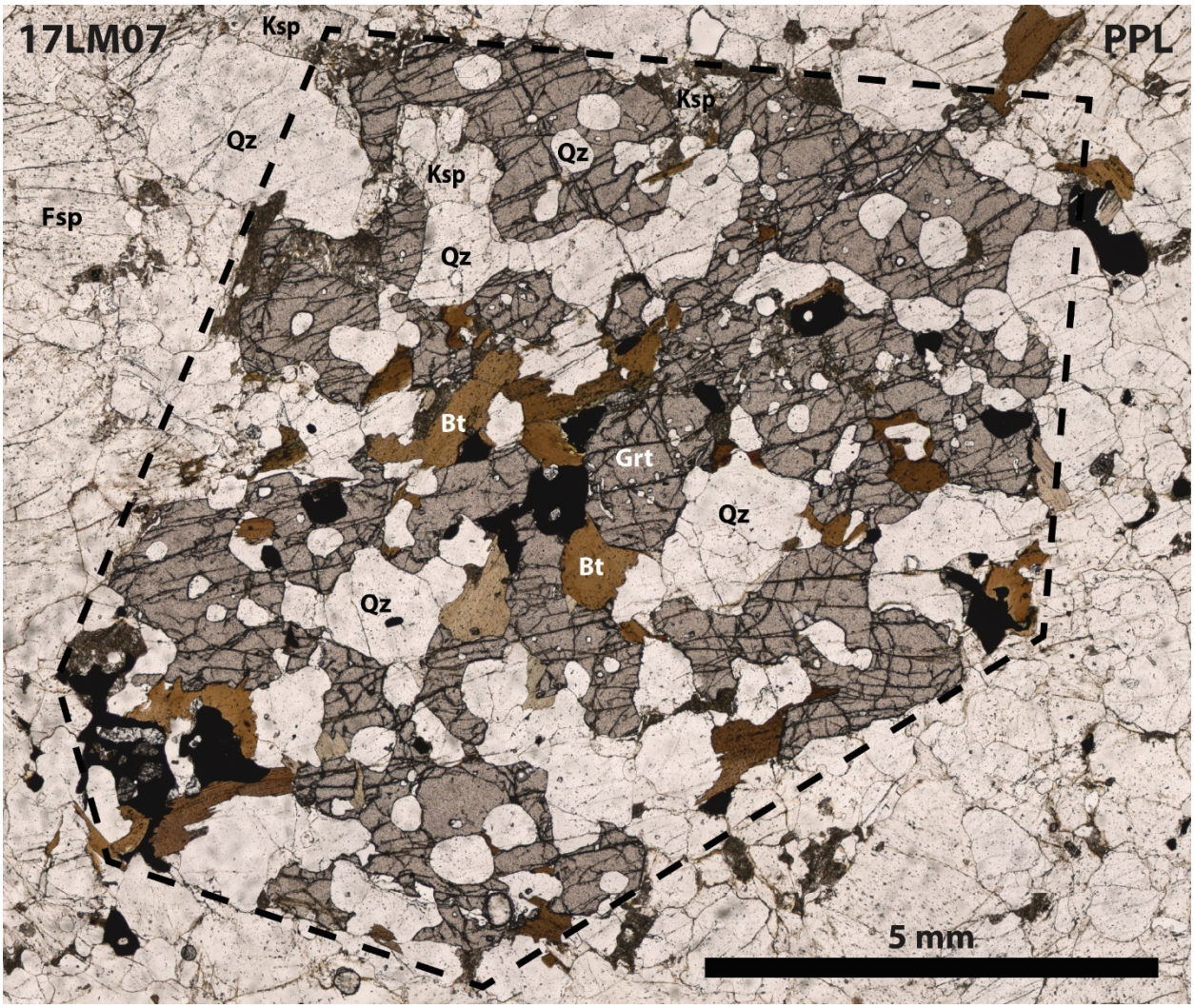

Figure 8. A 1 cm poikiloblastic garnet in melanosome (sample 17LM07). Dotted line approximates former extent of garnet before decomposition. Embayment of quartz has decomposed garnet edges. Quartz inclusions are found throughout, and K-feldspar inclusions are found near the top of the garnet crystal. Biotite and ilmenite are found in the garnet core and along some edges.

Figure 9. Relict Rutile in Garnet

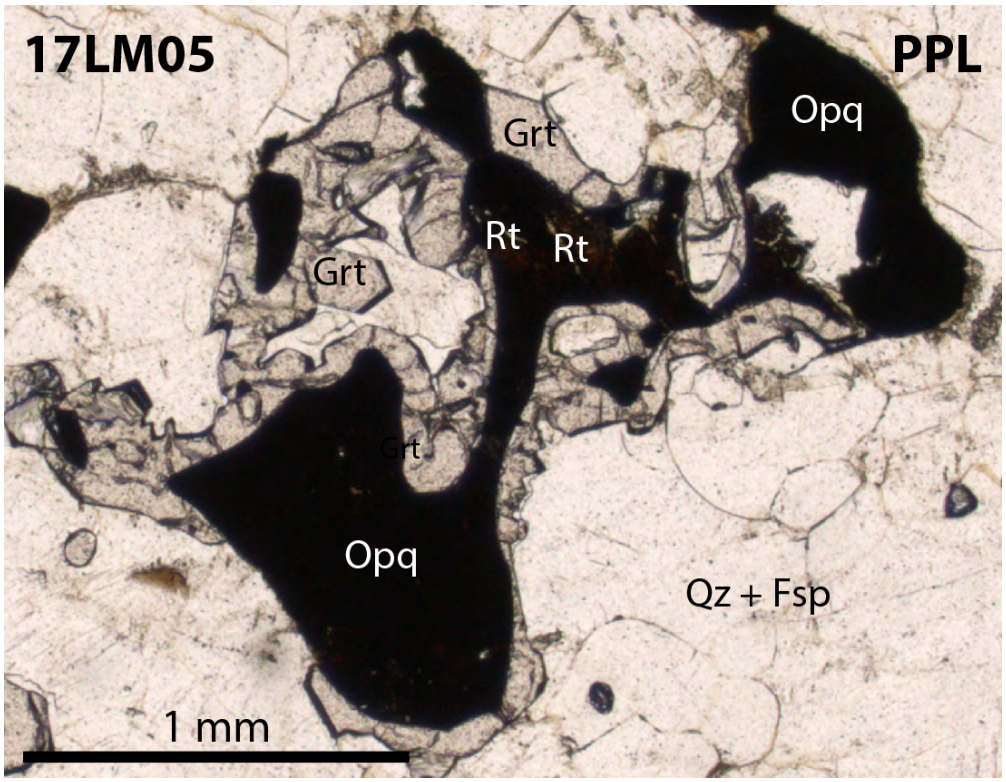

Figure 9. Photomicrograph showing Fe-Ti oxide and garnet corona structure with relict rutile in its core (sample 17LM05).

In-Source Leucosome

Compared to melanosome, in-source leucosome contains far more quartz and sillimanite and less feldspar and micas (Table 1; Figure 10). Quartz in in-source leucosome contains crystals ranging from 0.5 to 5 mm and on average appear slightly coarser than in the melanosome. Sillimanite is found as aligned, fine-grained, elongate crystals and often appears fibrolitic. Two generations of sillimanite growth were confirmed based on cross-cutting relationships and Raman spectroscopy (Figure 11; Metzger et al., in press). Biotite and feldspar in in-source

leucosome are common in diffuse contact zones with melanosome. Biotite and feldspar in these diffusion zones appear similar to those minerals in the melanosome, and are most likely part of the residuum left after extraction of anatectic melt.

Garnet is heterogeneously distributed within in-source leucosome and generally appears more broken-down than garnet in the melanosome. When garnet is in or near leucosome, ilmenite, biotite, and sericitized feldspar are found in increasing abundance near the garnet in one direction in the channel and may indicate they are the products of garnet breakdown **(**Figure 3**,** Figure 12**)**. These breakdown products are also found without significant garnet, except for very small (~200 μm) relicts (Figure 13), indicating a more complete breakdown. In one location, leucosome appears to be deflected around relict garnet and garnet breakdown products, suggesting the garnet predated leucosome development and its subsequent breakdown occurred within a leucosome that flowed around the garnet (Figure 13). Elsewhere in the leucosome a ~5 mm garnet grain contains 50-500 μm polyphase inclusions of quartz + feldspar + biotite ± xenotime, which may represent melt inclusions or "nanogranites" similar to those reported in migmatites from the western Adirondack Highlands (Darling, 2013) and from other migmatite terranes (Figure 12; e.g., Ferri et al., 2020; Gianola et al., 2020; Carvalho et al., 2021). These relict garnets in the leucosome bear some similarities to garnet in the melanosome such as sericitized feldspar along their rims and embayments of biotite + sillimanite + quartz + plagioclase (Figure 8).

Figure 10. Minerals in Leucosome

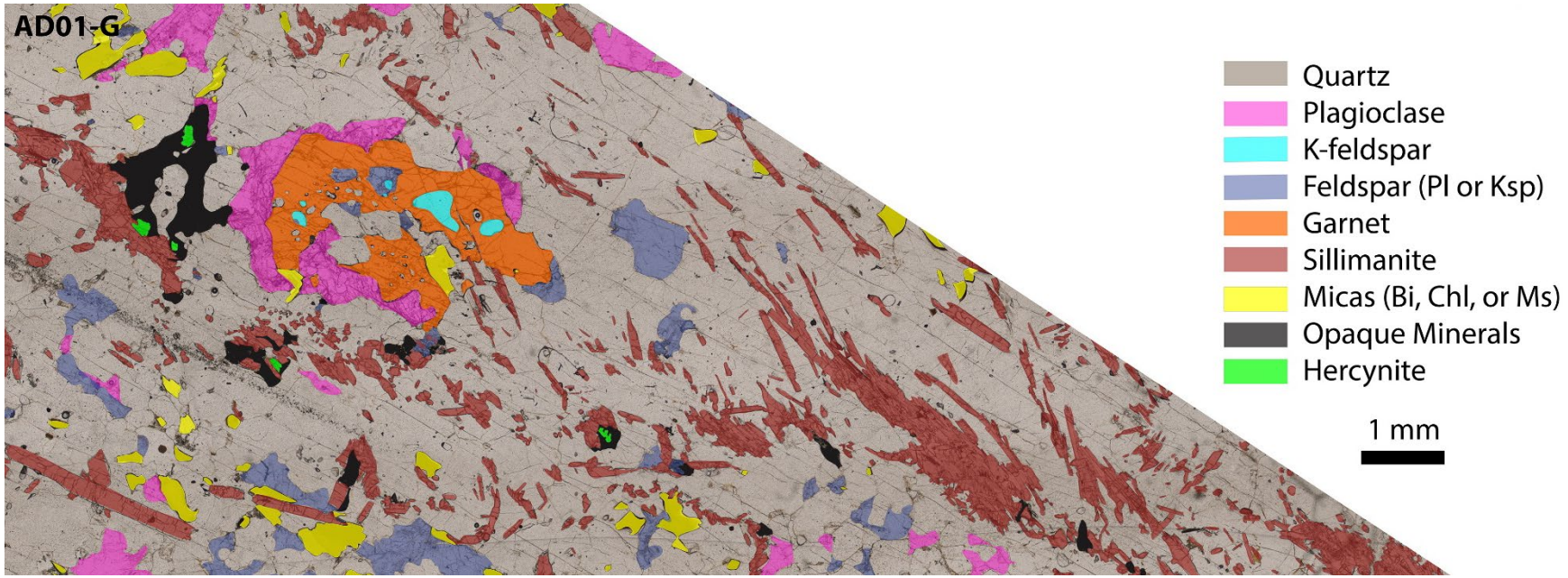

Figure 10. Phase map used to quantify mineral modes in in-source leucosome (sample AD01-G; part of Figure 3). All minerals are shaded according to the key, except quartz which is the unaltered PPL image. Aligned fibrolitic sillimanite in quartz matrix is typical of in-source and in-site leucosome. Hercynite in leucosome is commonly found with opaque phases and sillimanite. Micas are more common near garnet or as garnet breakdown products.

Figure 11. Two Generations of Sillimanite in Leucosome

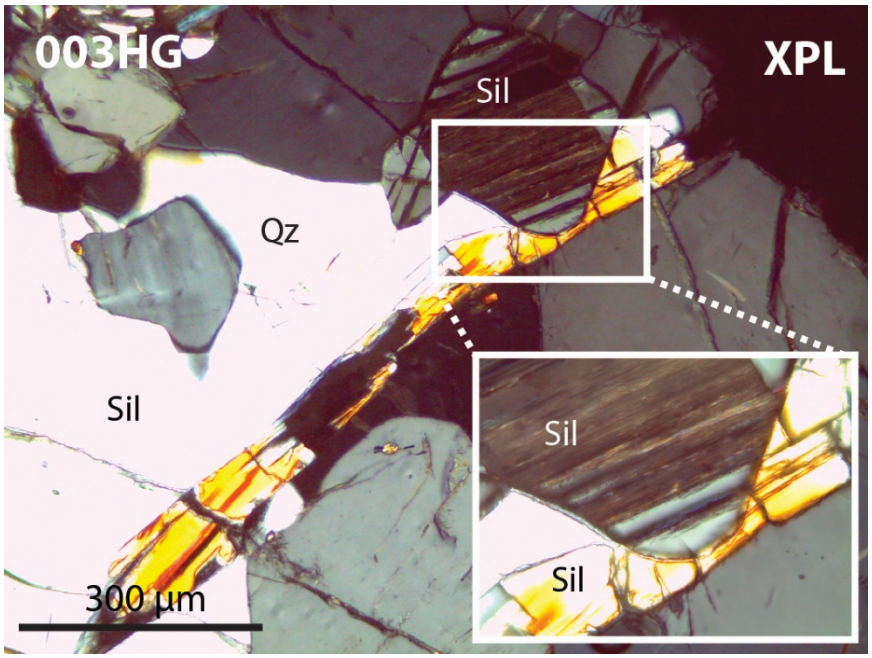

Figure 11. Two generations of sillimanite verified by Raman spectroscopy (Metzger et al., in press). Late blocky sillimanite overgrows elongate sillimanite in leucosome of sample 003HG. Inset shows an enlargement of the overgrowth.

Figure 12. Garnet Breakdown in Leucosome

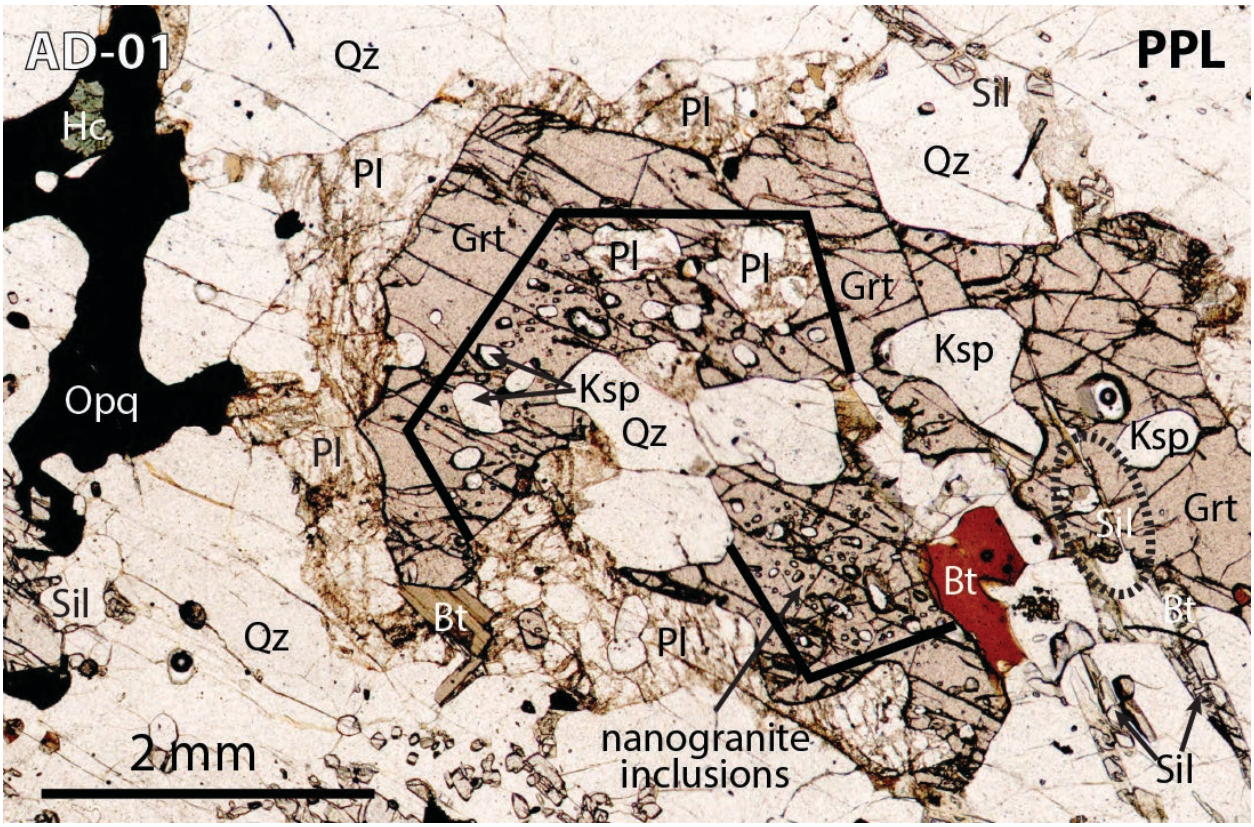

Figure 12. Peritectic garnet in leucosome (sample ADO1). The thick black lines in garnet outline an area that contains more abundant small inclusions of Ksp + Pl + Qz than outside the line. The inner core may represent a garnet that trapped inclusions as is grew around melt. The outer, less-included portion of the garnet may have grown with a less voluminous melt phase.

Figure 13. Garnet Breakdown Products within Leucosome Channels

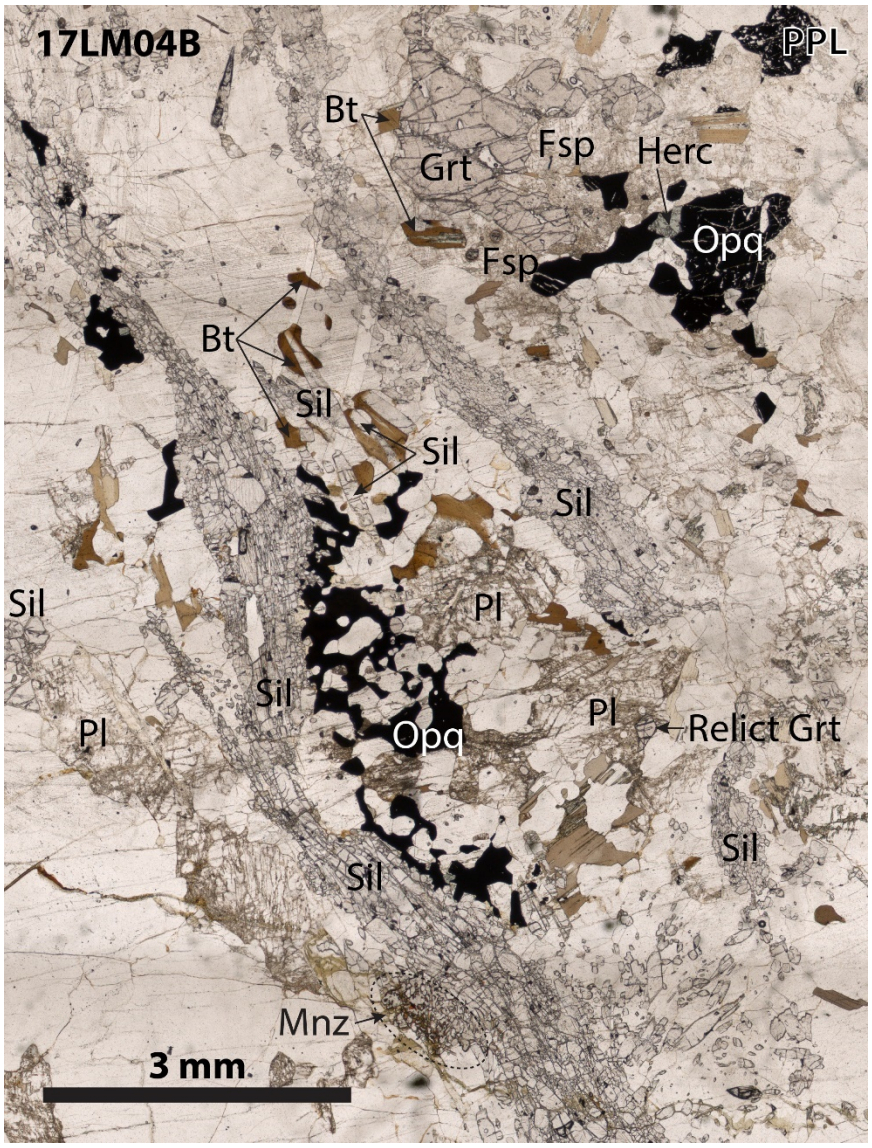

Figure 13. Photomicrograph showing garnet breakdown products found in in-source leucosome (sample 17LM04B). The teardrop shape in the center contains products of Reaction 8 (see Net-Transfer Reactions Along the P-T Path section below) where biotite + sillimanite + plagioclase + quartz form from the breakdown of garnet + ilmenite + K-feldspar during melt recrystallization. A small relict garnet is also present. The leucosome appears to deflect around the "tear drop" indicating the leucosome flowed around a former garnet grain. Another, more intact garnet grain lies just outside the leucosome. The garnet grain within the leucosome may have progressed further in reaction 8 because it had more access to reactant phases (i.e., melt) from the leucosome.

Opaque minerals occur between some sillimanite grains as large, ~2 cm long aggregates adjacent to sillimanite within the leucosome, or as smaller interstitial crystals. As in the melanosome, these opaque phases contain lamellae of magnetite, rutile, and ilmenite. Opaque phases in the leucosome are in direct contact with the surrounding leucosome (Figure 12**,** 13), whereas opaque phases in the melanosome are separated from the matrix by feldspar melt-films (Figure 7).

Hercynite-gahnite series spinel is much more common in the in-source leucosome than in the melanosome and is found exclusively in association with opaque phases. Similar spinel-bearing oxide aggregates found in rocks of the Eastern Ghats Belt have been interpreted as products of the breakdown of primary spinel Ti-Al-Fe-Al spinel during near-peak metamorphism and through retrogression (Bose et al., 2009; Dasgupta et al., 2017).

Figure 14. Sillimanite, Ilmenite, Hercynite in Leucosome

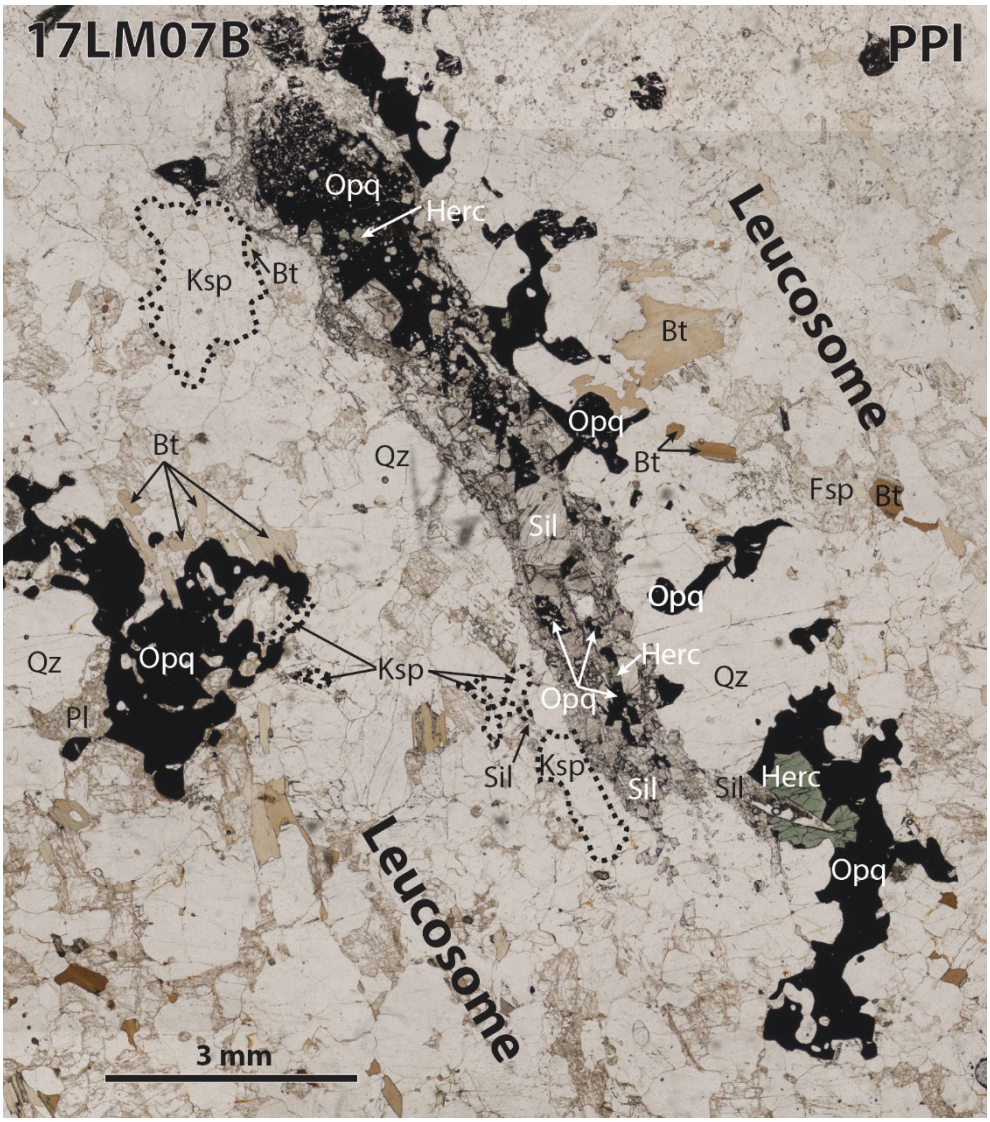

Figure 14. Vein of sillimanite and opaque minerals in quartzofeldspathic leucosome. Biotite and K-feldspar are present adjacent to sillimanite and opaque phases. Hercynitic spinel is found adjacent to opaque phases and within the sillimanite + opaque vein. The textures observed in this area may represent reaction 1 (see discussion of Fe-Ti Oxides in the Mineral Chemistry section below) where biotite and sillimanite are breaking down to form hercynite, K-feldspar, Quartz, and vapor (Montel et al., 1986). Vapor released in the reaction may have contributed to partial melting of the quartz and feldspar matrix (Montel et al., 1986).

Leucocratic Veins

Leucocratic veins range in width from ~5 mm to 2 m (Figures 4, 5, 15). They contain about two-thirds feldspar, which is predominantly K-feldspar, and one-third quartz, with accessory biotite and opaque phases near its neosome host. Generally, the leucocratic veins form sharp contacts with their host. In some places biotite and opaque selvages found at the contact between host and leucocratic vein indicate that the neosome may have reacted with the melt that crystallized to form the leucocratic vein (Sawyer, 2008).

Figure 15. Minerals in Leucocratic Vein

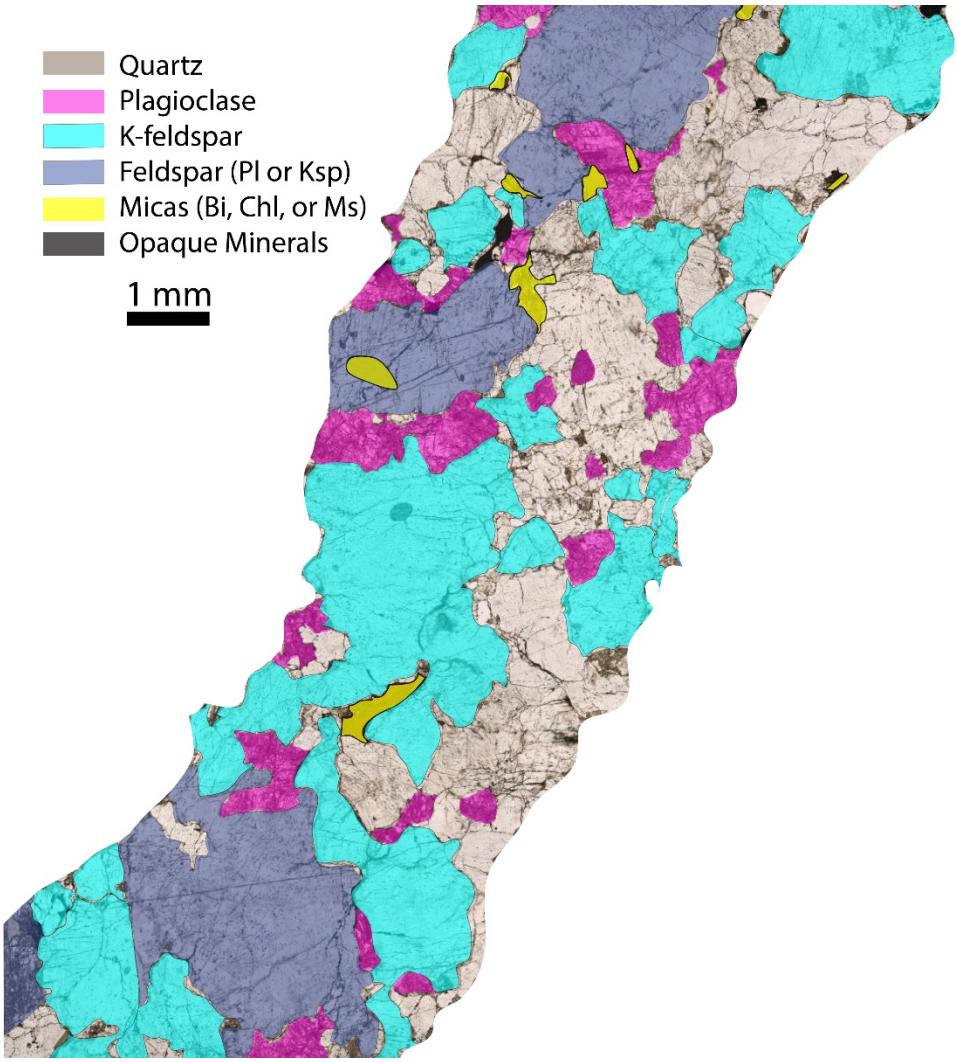

Figure 15. Phase maps used to identify mineral modes in leucocratic vein from Figure 5 (sample 17LM06). Leucocratic veins have much more K-feldspar than other migmatite domains.

Mineral Chemistry

Mineral composition data for select phases were collected to look for compositional zoning in garnet, and to observe compositional differences of feldspar, biotite, and Fe-Ti oxides in different migmatite domains or in various textural relationships with other minerals. Observed mineral compositions of garnet were correlated to compositional isopleths in the phase equilibria models (see Phase Equilibria Modeling below) to better constrain P-T conditions for Ledge Mountain rocks.

Garnet

Garnet exhibits chemical heterogeneity across all samples that contain garnet ($Alm_{66-75}Sp_{11-16}Py_{7-13}Gr_{5-8}$) and have chemical composition similar to garnet found in other granitic and granulitic rocks (Figure 15; Suggate and Hall, 2014), although their manganese content is significantly higher.

Major element zoning is weak to absent as revealed by compositional x-ray maps (Figure 17) and microprobe point traverses (Figure 18). Transects of garnet grains found in the melanosome of sample 5-6 and 17LM04 (Figure 18) give evidence of a slight Fe and Mn increase and corresponding Mg decrease of 1-3% in garnet rims compared to cores. Other garnet transects in both melanosomes and in-source leucosome show variation of less than 0.5% across the entire grain. Transects of a large garnet in 17LM04B gives evidence for both an increase and decrease in Fe of up to 4%, and inverse for Mg across the grain compared to rims. Transects of many garnets (Figure 18) reveal noisy zoning patterns as spot-analyses along a transect may be affected locally by large embayments, inclusions, or breakdown products within the core. Some

garnets appear to be composite grains, which might explain the zoning complexity across larger grains (Figures 8, 18).

Figure 16. Garnet Composition Diagram

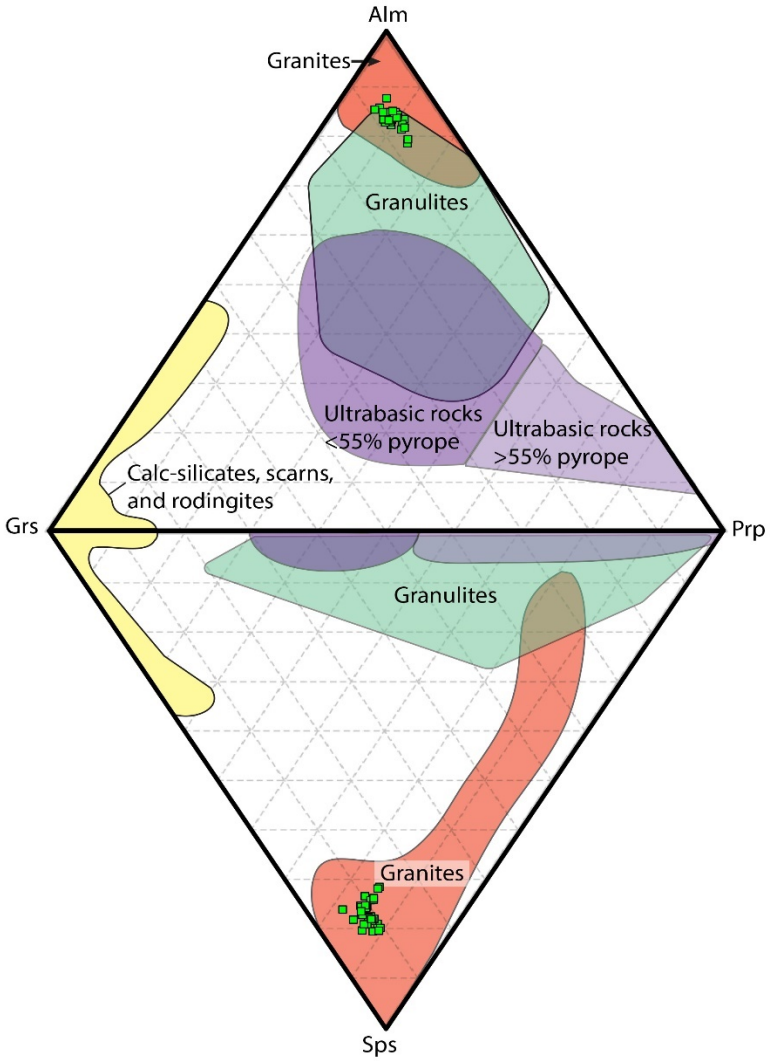

Figure 16. Ternary plots of garnet composition from 29 grains from 7 samples. Colored fields show groupings where 2400 garnets were grouped by parent rock-type (Suggate and Hall, 2014). Garnet compositions plot where the granite and granulite fields overlap in Grs-Alm-Prp space, and in the granite field in Grs-Sps-Prp space. ***Abbreviations:*** *Grs: grossular; Alm: almandine; Prp: pyrope; Sps: spessartine after Whitney and Evans (2010).*

Figure 17. Mineral Zoning in Garnet

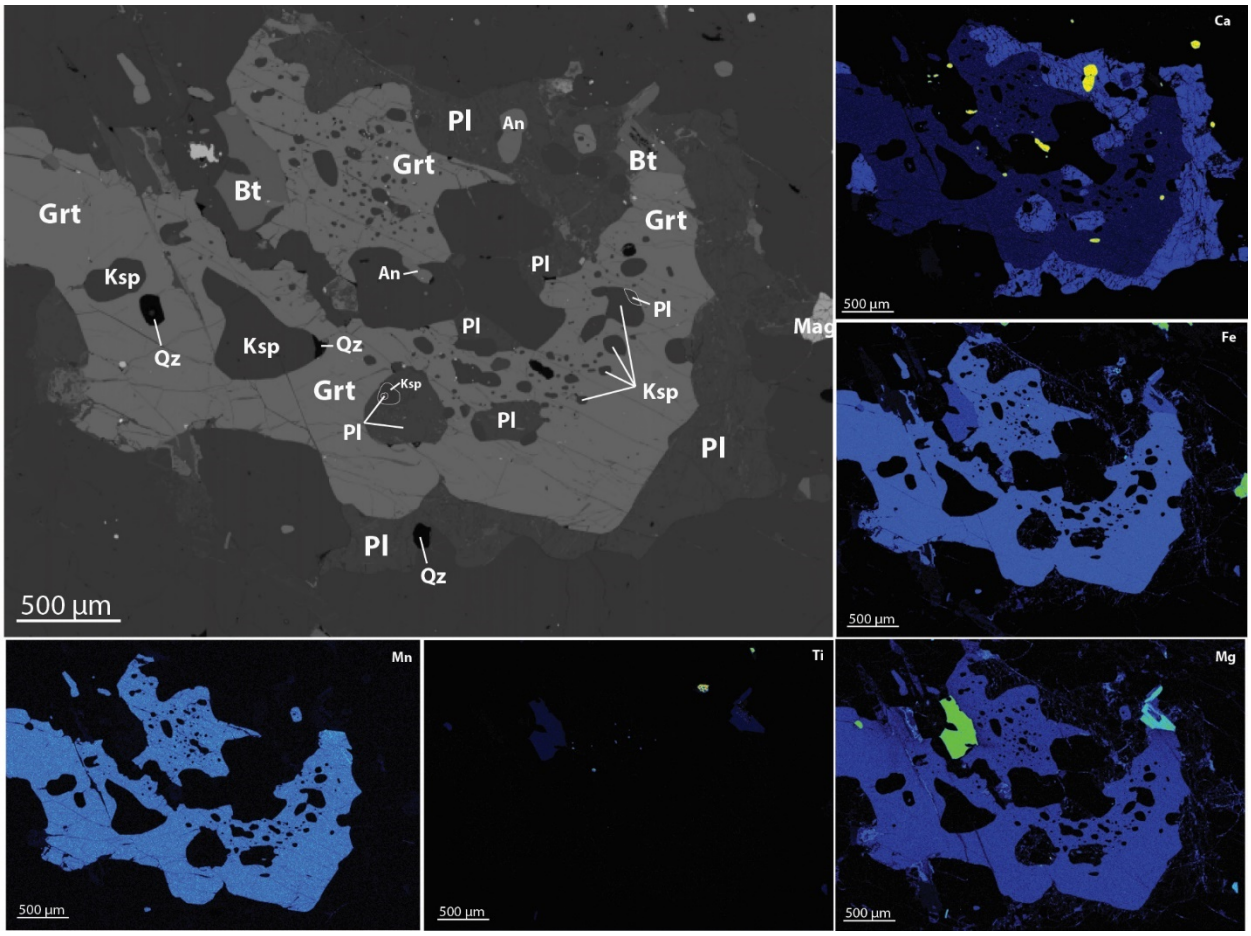

Figure 17. BSE image (upper left) of garnet crystal from Figure 12, and color x-ray maps showing absent zoning.

Figure 18. Compositional Zoning of Selected Garnet Grains

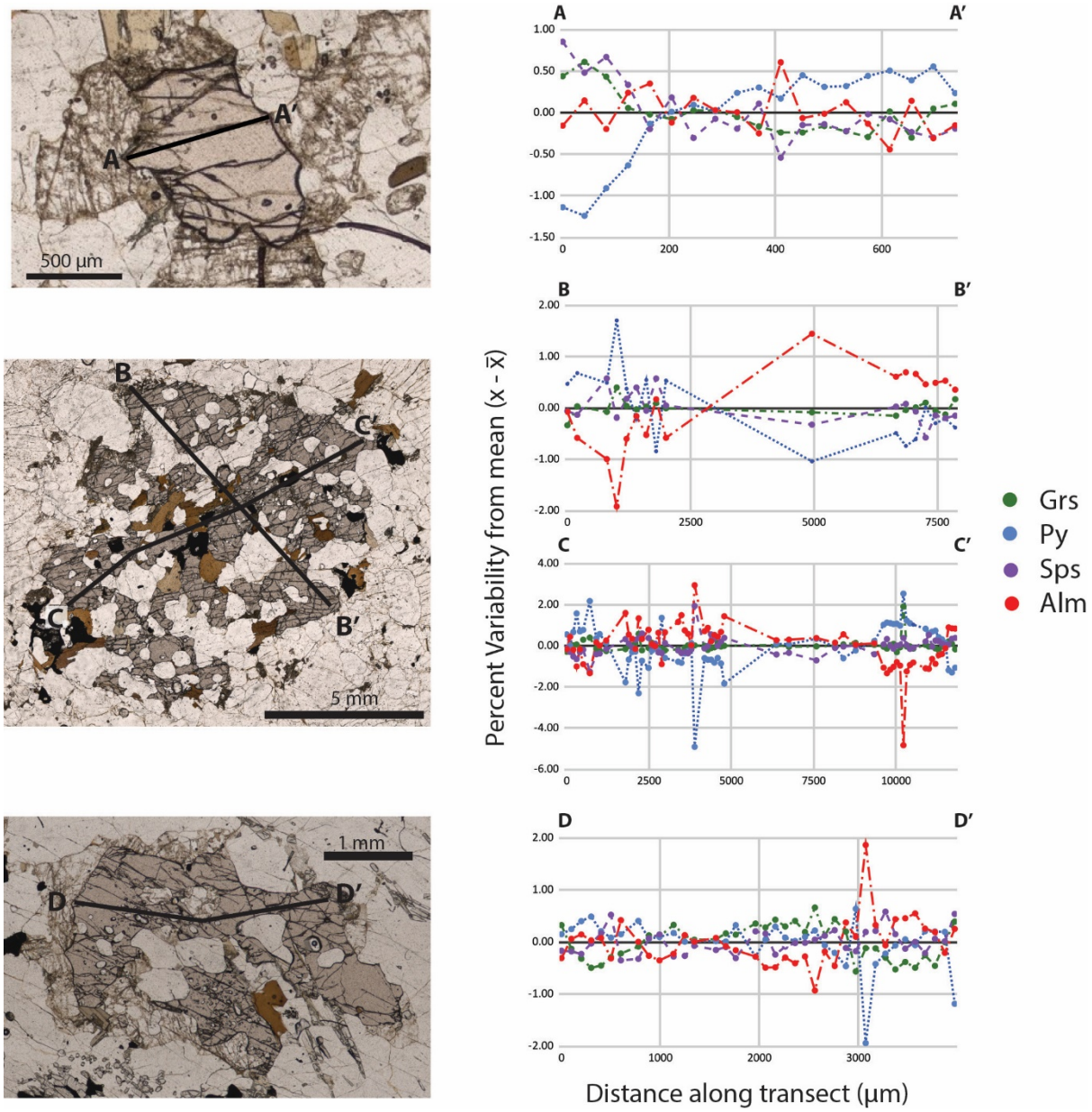

Figure 18. Garnet zoning profiles in samples 17LM04, 17LM07, and AD01. Percentage of garnet end-member compositions are shown in green (Grs), blue (Prp), purple (Sps), and red (Alm). Sample 17LM04 shows a decrease in spessartine and grossular from left to right, and an increase of ~1% in almandine. Transects across 17LM07 show variability range of up to ~7%, but generally within ~3% across the crystal. Sample AD01 shows ~1% variability with no recognizable zoning patterns.

Feldspar

Feldspar compositional ranges vary slightly depending on whether they form rims on garnet or Fe-Ti oxides, are inclusions in garnet, or occur in the matrix of the melanosome. Matrix plagioclase varies in composition from An_{29} to An_{44} (Figure 19). Feldspar rims on Fe-Ti oxides have three compositional groupings: slightly more sodic plagioclase than plagioclase in the matrix ($An_{33} – An_{36}$), albite ($Ab_{82} – Ab_{100}$), and orthoclase ($Or_{80} – Or_{95}$). Feldspar rims around garnet also have compositions that fall into three groupings: similar to matrix plagioclase and occasionally more calcic ($An_{34} – An_{51}$), orthoclase ($Or_{38} – Or_{80}$), and a single anorthite (An_{99}). Most plagioclase grains are homogeneous but a few show slight zoning (~2-3% An), with rims both enriched and depleted in calcium relative to the cores. K-feldspar rims on a plagioclase vary from Or_{84} to O_{90} (Metzger et al., in press).

Figure 19. Feldspar Composition Diagram

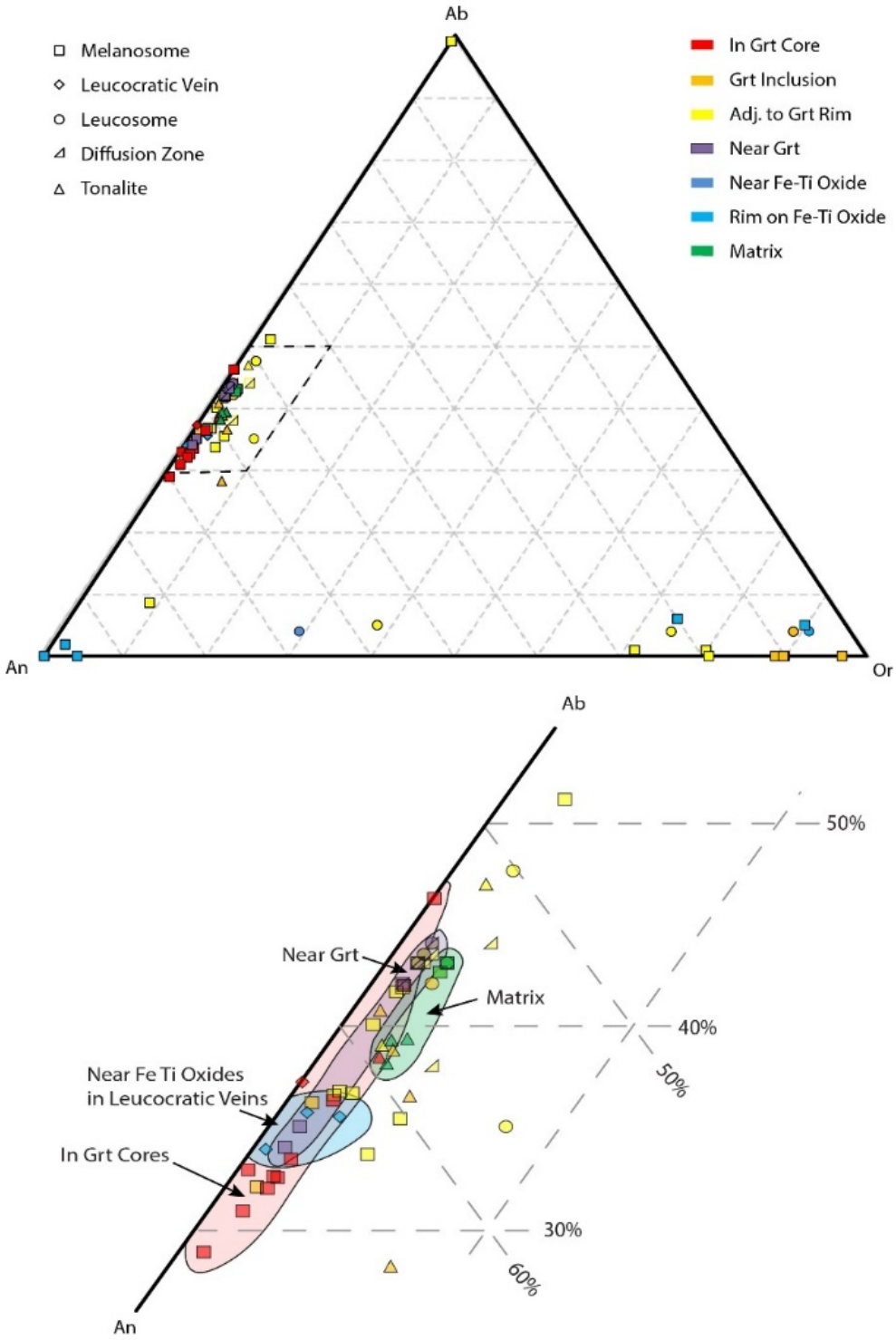

Figure 19. Feldspar compositional diagram comparing feldspars in different migmatite domains and textural settings with garnet and Fe-Ti oxides. The bottom diagram is an inset of the area indicated by the thick dotted line in the upper diagram. Most feldspar compositions cluster between 30-50% Ab with some minor grouping within that range. K-feldspars tend to present as garnet inclusions and on Fe-Ti rims in melanosome. There is no clear pattern between feldspar composition and its proximity to garnet rims.

Biotite

Biotite compositions [X_{FeO*} = (FeO +MnO)/(FeO+MgO+MnO)] depend on which part of the migmatite they are located and core-rim relationships with Fe-Mg bearing minerals (Figure 20). Quartzofeldspathic melanosome host biotite with X_{FeO*} ranging from 0.75 to 0.82 and TiO_2 contents ranging from 5.2-7.4% with most clustering around 5.8-6.2% (Figure 20). Biotite found in Leucosome, adjacent to garnet, within garnet cores, or adjacent to Fe-Ti oxide minerals is more magnesian (X_{FeO*}: 0.68 – 0.78) and has lower Ti than does melanosome biotite. Biotite adjacent to garnet rims (X_{FeO*}: 0.67-0.80) is more ferroan than those found within garnet cores (X_{FeO*}: 0.67-0.73); this compositional difference may be due to the proximity of the garnet-rim biotite to the melanosome matrix. Biotite rims on Fe-Ti oxide minerals have X_{FeO*} values of 0.74 to 0.76 (n = 3).

Figure 20. Biotite Composition Diagram

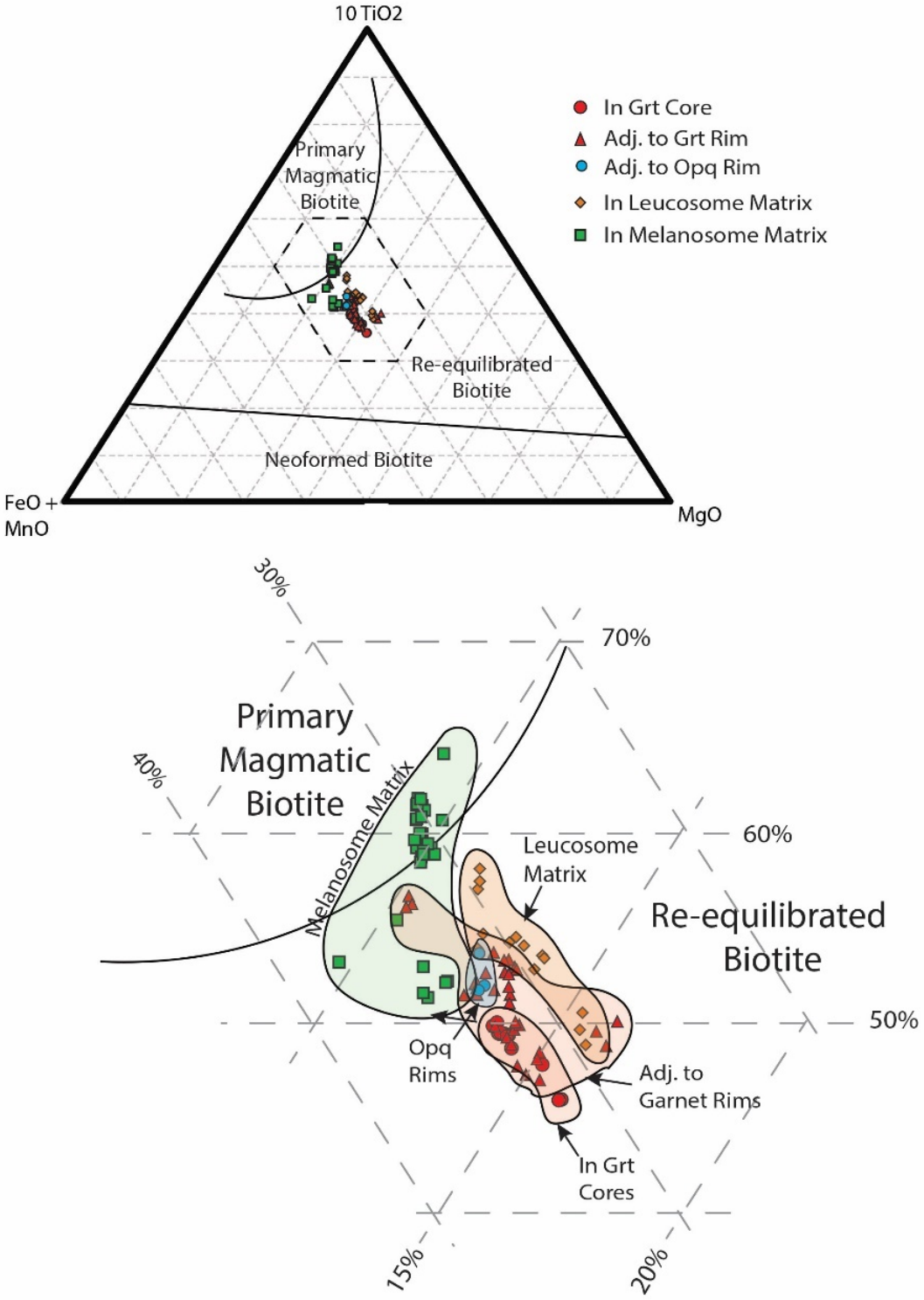

Figure 20. Biotite compositional diagram comparing biotite composition across different migmatite domains and its relationship to garnet and Fe-Ti oxides (opaque minerals). The bottom diagram is an inset of the area indicated by the thick dotted line in the upper diagram. Primary, re-equilibrated, and neoformed biotite fields are from the Nachit et al. (2005) classification that applies to primary magmatic biotite, primary magmatic biotite that has been re-equilibrated by late-magmatic fluid, and biotite that has formed in equilibrium with a hydrothermal fluid. The application of the classification to Ledge Mountain biotite is discussed in the Discussion section. All biotite composition falls between ~3.5-5.5% TiO_2, ~28-38% FeO+MnO, and 18-33% MgO. Biotite in the melanosome matrix has higher TiO_2 contents and lower X_{FeO} values suggesting they may have formed at higher temperatures than biotite found in the leucosome and those associated with garnet or Fe-Ti oxides (Sawyer, 2008).

Fe-Ti Oxides

The oxide minerals in Ledge Mountain migmatites show complex intergrowths and exsolution textures (Figure 21). Electron microprobe analysis verified the presence of both ilmenite, magnetite, and rutile within optically opaque phases. Green hercynite-gahnite series spinel (Figure 21) contains variable amounts of ZnO (11-29 wt. %) and FeO (56-58 wt. %), and little MgO (1-2 wt. %). These spinel compositions are similar to those found in restite enclaves and leucosome from migmatites in Ardèche, France, where biotite + hercynite spinel + sillimanite + ilmenite bearing assemblages stabilize at 5 – 6 kbar and 800˚ - 850˚C (Montel et al., 1986). Montel et al. (1986) describes the breakdown of biotite and sillimanite to produce hercynite spinel according to the reaction:

$$Bt + Sil = Hc + Qz + Ksp + H_2O \qquad \text{[Reaction 1]}$$

Reaction 1 releases vapor and can cause partial melting the adjacent quartzofeldspathic phases, and may be responsible for channels of leucosome adjacent to these phases (e.g., Figure 14).

Figure 21. Spinel Composition Diagram

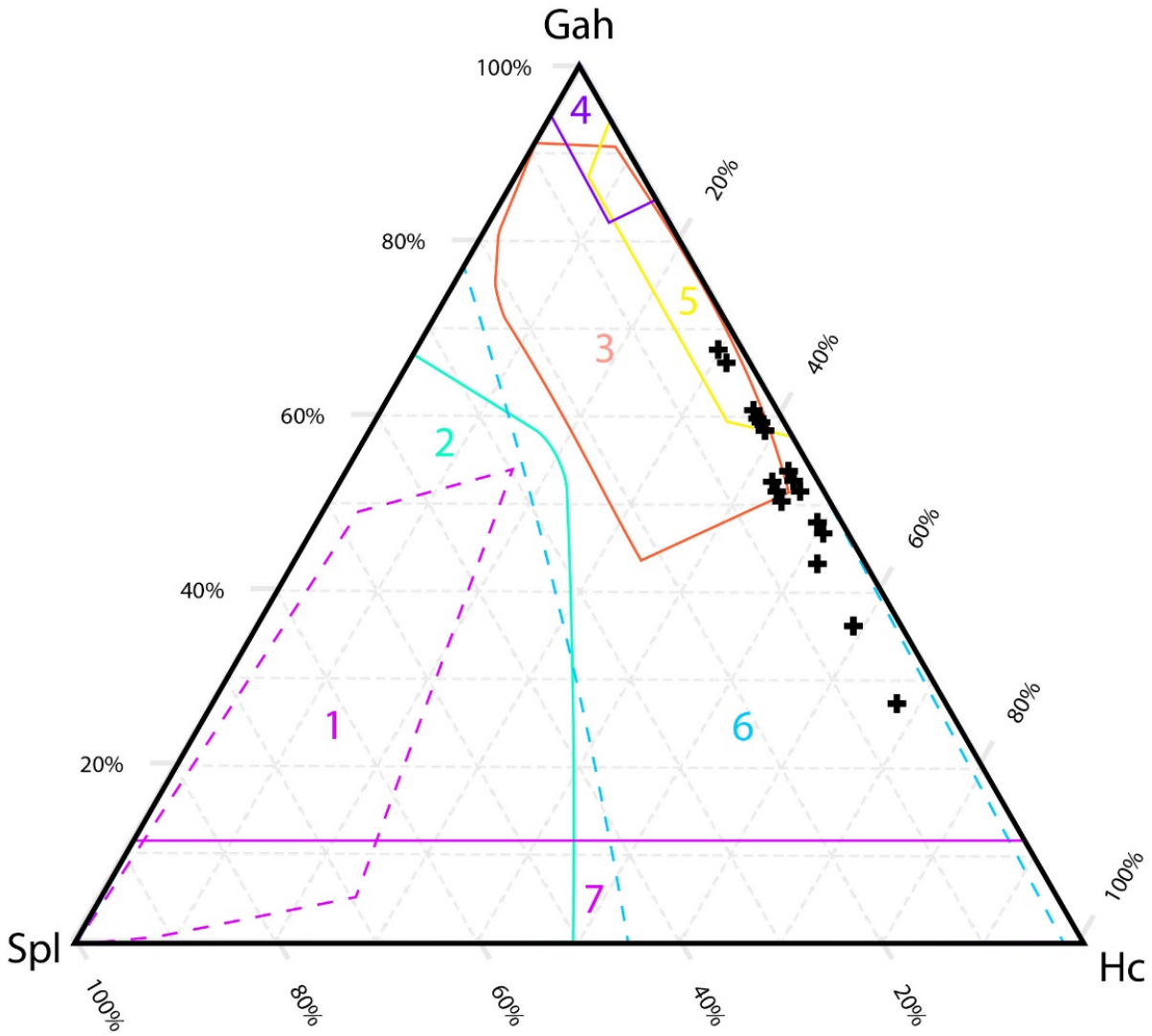

Figure 21. Gahnite (Gah), hercynite (Hc), spinel (Spl) composition diagram showing the composition of hercynite-gahnite series spinel from Ledge Mountain. The outlined fields correspond to Heimann et al. (2005): (1) Marbles, (2) metamorphosed massive sulfide deposits and S-poor rocks in Mg-Ca-Al alteration zones, (3) metamorphosed massive sulfide deposits in Fe-Al metasedimentary and metavolcanic rocks, (4) metabauxites, (5) granitic pegmatites, (6) unaltered and hydrothermally altered Fe-Al-rich metasedimentary and metavolcanic rocks, and (7) Al-rich granulites. Ledge Mountain spinel partially plot in fields 3 and 5, and plot completely within field 6.

Phase Equilibria Modeling

Whole Rock Geochemistry

Whole-rock geochemical analyses were performed on all samples by XRF and ICP-MS at the GeoAnalytical Lab at Washington State University. Johnson et al. (1999) presented a discussion of the precision and accuracy of these methods.

Pseudosection Models

Pseudosections were created using the phase equilibria modeling program *Perple_X* version 6.8.9 (and corresponding data files; Connolly, 2005; 2009), and the internally consistent thermodynamic database for minerals and water (CORK model, Holland and Powell, 1991; 2001; 2011). Pseudosections were constructed using the whole-rock geochemical data from pressures 4 to 20 kbar and temperatures of 600 to 1200° C.

All 38 analyzed samples were modeled using *Perple_X* and five migmatite samples were chosen for more extensive thermodynamic modeling and incorporation of isopleth models of mineral compositions based on their preserved high-grade minerals such as garnet, sillimanite, and rutile and a relative lack of retrogression observed in hand specimen and thin section. Samples 5-6, 17LM04, AD01, and 001HG are granitic migmatites; and sample 11 is a meta-leucotonalite (Connolly, 2005; 2009; Metzger et al., in press). Prominent but localized sillimanite-quartz layers were avoided during sampling.

H_2O content

The H_2O content in geochemical systems largely determines the position of the solidus and phase boundaries in pseudosections, necessitating a more accurate method than using LOI values for determining H_2O content (Hasalová et al., 2007; Bartoli, 2017). Preliminary pseudosections, modeled with the LOI values, indicate that temperatures greater than ~850˚C yield no solid hydrous phases and suggests that all water is fluid at higher temperatures. Samples show little evidence for late retrogression caused by hydrothermal alteration due to infiltration of external fluids; therefore retrograde biotite likely formed during isobaric cooling, obtaining its hydrous chemical component from crystallizing melt rather than external hydrothermal alteration. In the simplest scenario, no melt left the system and the H_2O content directly relates to the modal percentage of biotite observed in thin section. If melt (and therefore H_2O) was lost, the final mineral composition would underrepresent the amount of water present during peak conditions, and therefore must be scaled with melt loss. If biotite was removed from the system with any leucocratic melt loss, then I would underestimate the amount of water present during peak conditions. However, the melanosome is enriched in biotite and did not enter the leucocratic melts thus making the estimate of the biotite percentage a valid proxy for the H_2O content in these rocks.

I estimate the percentage of H_2O in the migmatite samples at 0.12 wt. % based on the amount of biotite they contain (the molar percentage of H_2O in biotite is ~4% g H_2O/g Bt; Lechler and Desilets, 1987; Indares et al., 2008). Except for melanosome domains adjacent to leucocratic veins, biotite comprises ≤1-3% of the volume in all migmatites. Indares et al. (2008) performed forward modeling using 0.35 to 0.62 wt. % H_2O for kyanite-bearing paragneisses

from the central Grenville province that contain slightly more biotite than my samples; given the lesser amount of biotite in my samples, using 0.12 wt. % H_2O in my models is reasonable.

To test this H_2O estimate based on biotite content, I modeled temperature versus molar composition H_2O (T-M_{H2O}; Figure 22) at the pressure containing the current stable solid assemblage in preliminary thermodynamic models (6 kbar) following a method similar to that described by White et al. (2005), Hasalová et al. (2007), and Bartoli (2017). The range of H_2O values is determined where the observed assemblage Ksp + Pl + L + Bt + Ilm + Grt + Sil + Qz stabilizes at lower suprasolidus conditions - at the P-T conditions where the final melt fraction would have crystallized (White et al., 2005). This model yielded H_2O concentrations from 0 to 0.45 wt. % H_2O (Figure 24) which is consistent with the low volume of hydrous minerals (i.e., biotite) observed in Ledge Mountain granulites and includes my best estimated value of 0.12 wt. % H_2O that was derived from the biotite content in my samples (≤3%). Because these two methods for estimating H_2O content produced similar results, I chose to use the far simpler method of calculating H_2O values from the biotite content.

Figure 22. Water Content

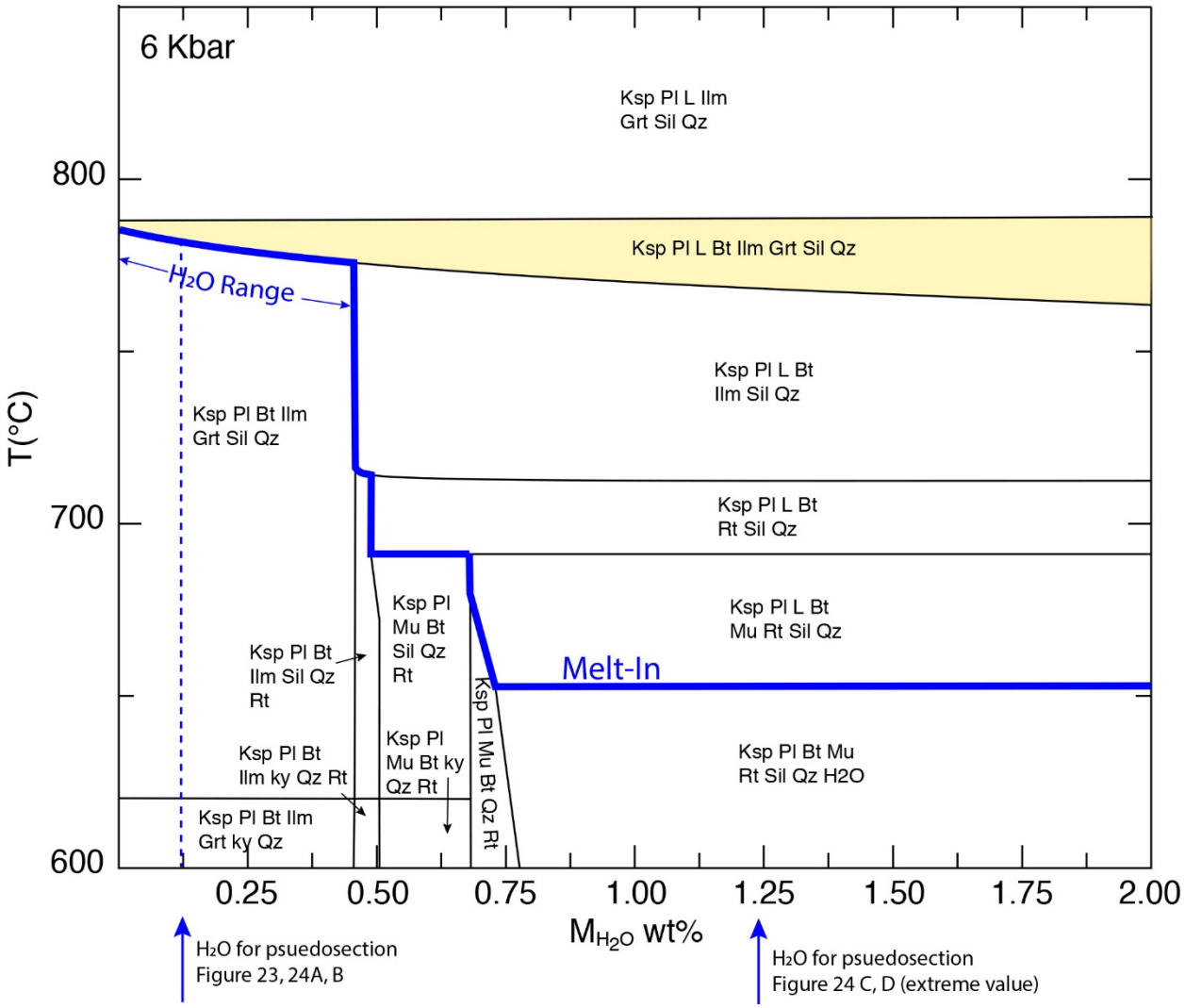

Figure 22. T-M_{H2O} diagram calculated at 6 kbar, using the igneous set (see Solution Model Selections below) of solution models (NCKFMASHT). The range of 0-0.45 wt. % H_2O corresponds to where the observed current solid assemblage (yellow field) stabilizes at the solidus where the last melt fraction crystallizes. Our best estimate of 0.12 wt. % H_2O, calculated from the volume of hydrous minerals observed in thin section, falls within this range and agrees with these results (Figure 24A,B). The high estimate of 1.23 wt. % H_2O falls outside of this model's range - representing a tenfold increase over our best estimate for water content - and was used to test phase equilibria models with a significantly higher water content and that has the effect of reducing the estimated metamorphic temperatures for our peak assemblage (see Figure 24C,D).

To better understand the effect of using higher H_2O estimates, I also ran models with 1.23 wt. % H_2O (Figure 24C, D) that derives from the 1.227 wt. % H_2O value used by Storm and Spear (2005) for metapelitic rocks in the southern Adirondack Highlands. Increasing H_2O content to 1.23 wt. % represents a tenfold increase in H_2O content over my best estimates and overestimates the amount of biotite in Ledge Mountain granulites. I use this high estimate of 1.23 wt. % H_2O to test the reasonable range of P-T conditions for peak metamorphism of Ledge Mountain migmatites.

Using 1.23 wt. % H_2O shifts the peak fields to lower temperatures by ~50° C and shifts the solidus ~100° C to lower temperatures and water saturated conditions. Increasing the amount of water in the models decreases the temperature indicated by the peak fields by ~50-100° C per wt. % H2O. Even adding up to 2 wt. % H_2O to the igneous models - nearly 20x the estimate based on the amount of biotite - shows that Ledge Mountain rocks were still metamorphosed at temperatures over 900° C (UHT granulite-facies conditions). The models required the addition of >3 wt. % H_2O to shift the peak field to sub-UHT conditions.

Solution Model Selections

To account for possible variation in protolith type I use two set of solution models and thermodynamic datafiles (Figure 24): An “igneous set” of data files includes the thermodynamic data file hp633ver.dat (Holland and Powell, 2011; Holland et al., 2018) and solution models for the partial melting equilibria involving basaltic through granitic melts: melt [melt(HGP)], spinel [Sp(HGP)], biotite [Bi(HGP)], and garnet [Gt(HGP): Holland et al., 2018]. A “metapelite set” of

data files includes the thermodynamic data file hp62ver.dat (Holland and Powell, 2011; Green et. al, 2016) and solution models for equilibria in metapelitic bulk compositions: melt [melt(W)], biotite [Bi(W)], garnet [Gt(W)]; White et al. (2014a)], and spinel [Sp(WPC); White et al., 2002]. Biotite is "somewhat reparameterized" from White et al. (2014a). Both model sets also utilize the following solution models: white mica [Mica(W); White et al., 2014a]; ilmenite [Ilm(WPH); White et al., 2000; 2007)]; and ternary-feldspar [feldspar; Fuhrman and Lindsley, 1988]. The margarite ("ma") endmember was excluded from calculations to avoid conflicts with Mica(W). The 'ilm' and 'ilm_nol' solution phases were excluded to use the Ilm(WPH) model, which enables the calculation of ilmenite, hematite, and geikeilite end-members. Calculations using the igneous set were performed in the Na_2O-CaO-K_2O-FeO-MgO-Al_2O_3-SiO_2-H_2O-TiO_2 (NCKFMASHT) model system. Calculations using the metapelite models were extended to include MnO by White et al. (2014b), and were performed in the MnNCKFMASHT system to include spessartine end-member calculations. Calculations used the whole-rock geochemical data from Ledge Mountain for samples 5-6, 17LM04, AD01, 001HG, and 11 (Table 4).

Ferric (Fe_2O_3) and Ferrous (FeO) Oxide Content

Estimation of bulk-rock Fe_2O_3 is problematic, as it is not measured by XRF analysis. In Perple_X, if ferrous/ferric iron is the only redox couple included in calculation, the components are FeO and O_2. FeO represents the total iron component determined from whole rock chemistry analyses, and with additional O_2, Perple_X converts some of the FeO into the ferric component for calculation. Microprobe analyses shows low ferric contents in spinel (0.00-0.03 Fe^{3+} p.f.u.), garnet (0.00-0.05 Fe^{3+} p.f.u), and sillimanite (0.00-0.27 Fe^{3+} p.f.u.), and suggests that the bulk

rock composition is similarly low in ferric iron (Sarkar and Schenk, 2014; Walsh et al., 2015; Metzger et al., in press). Magnetite ($Fe^{+2}O{\bullet}Fe_2^{+3}O_3$) and hematite ($Fe_2^{+3}O_3$) are possible major ferric-iron-bearing oxides, and microprobe analyses suggest they comprise <1% of the modeled rocks. Assuming the ferric iron comes largely from magnetite, the concentration of O_2 (P_{O_2}) to use in perplex can be calculated using:

$$P_{O_2} = P_{magnetite}\left(\frac{M_{O_2}}{M_{Fe_3O_4}}\right) \qquad \text{[Equation 2]}$$

where $P_{magnetite}$ is the percentage of magnetite in the sample, and M_{O_2} and $M_{Fe_3O_4}$ are the molar weights of molecular oxygen and magnetite, respectively. If I assume as much as 1% magnetite in the bulk rock, then the O_2 component is no more than 0.069%; 0.1% O_2 is used in models to account for uncertainty in the amount of magnetite present.

Incorporating O_2 in the models requires using a solution model for magnetite [Mt(W)] which is valid from 800˚C to 1300˚C (Wood et al., 1991). Adding 0.1% O_2 to correct for ferric iron resulted in only rare magnetite in the models, irregular phase boundaries and islands, destabilization of rutile (TiO_2) across the P-T range, and the appearance of several minerals (e.g., Zo) across the pseudosection at low P-T conditions that have not been observed in thin section. Kendrick and Indares (2018) reported that increasing O_2 in phase equilibria models for anatectic aluminous granulites from the central Grenville Province had little effect on the overall topologies for the relevant assemblages. For these reasons, no ferric iron (O_2 component in *Perple_X*) was used in my models.

Mineral Isopleths

To understand how individual minerals changed with changing P-T conditions, isopleth models for mineral compositions were generated in *Perple_X* and overlaid onto the pseudosections. Garnet end-members (Fe, Mg, Ca) were selected for isopleth contouring in order to isolate P-T conditions of garnet formation. Modal percentages of garnet and sillimanite were also modeled to confirm that low modal percentages observed in petrographic analysis matched the modeled percentages at peak conditions. I modeled K-feldspar and plagioclase compositions, but I did not include feldspar isopleths because it is unclear texturally which feldspar grains grew during peak conditions and which grains may have resulted from retrograde reactions. Isopleths for biotite endmembers and modal percentages were not included because the retrograde fields for biotite already fall into a narrow P-T range.

Pseudosection Topologies

Two groups of similar pseudosection topologies in these five samples: models AD01, 17LM04, and 11 are similar (Figure 23A); and models 5-6 and 001HG are similar (Figure 23B). I distinguish the two different topologies based on the general shape of the stability fields and the location (in P-T space) of the major metamorphic reactions, but the two groups nevertheless yield similar P-T conditions for the peak and retrograde metamorphic events. I use sample 11 as an example of Group 1 models and sample 001HG to represent Group 2 models in Figure 23.

Peak metamorphic conditions in all samples are represented by the assemblage Pl + Ksp + Qz + Grt + Sil ± Rt + Melt. In all samples, retrograde overprint conditions are represented by the Bt-bearing assemblages at low P-T conditions, and are represented by the assemblage Bt + Pl

+ Ksp + Qz + Grt + Ilm ± Sil + Melt. Petrography shows that biotite is not in equilibrium texturally with the peak mineral assemblages, and biotite only appears at lower P-T conditions in pseudosection models (<~800° C). All models show that abundant melt is present at peak conditions through retrograde conditions of c. 800˚C.

Group 1 samples (AD01, 17LM04, and 11; Figure 23A,B**)** are Sil-bearing migmatites. Sample 11 is mineralogically different from AD01 and 17LM04 because it contains more plagioclase, no K-feldspar, and less accessory Bt and Ilm, but pseudosection topologies for these three samples are nearly identical. Group 2 samples (5-6 and 001HG; Figure 23C,D**)** are fine- to medium-grained, K-feldspar-rich migmatites. Sample 001HG differs from 5-6 in that it does not contain sillimanite, but the pseudosection topologies for these two samples are nearly identical.

Major element zoning in garnets in all samples is absent, showing no systematic pattern (Figures 17, 18). Modal estimates are based on hand specimens and petrography. Samples selected for thermodynamic modeling all have low modal percentages (<5%) of the key minerals garnet and sillimanite. I do not attempt to assess precise percentages for these and other accessory minerals and do not rely on calculated modal percentages to constrain peak P-T conditions. Rather, calculated garnet and sillimanite isopleths are overlain on modeled phase equilibria, and are used to check whether isopleth models are consistent with the low modal percentages of these minerals that I observed in the rocks). In all samples, retrograde conditions are represented by the chlorite- and biotite-bearing overprinting assemblages at low P-T conditions; petrography shows that biotite is not in equilibrium texturally with the peak mineral assemblage. The general consistency between the pseudosection topologies, textural data, and mineral compositions suggests that the pseudosection approach is suitable for inferring P–T

conditions in these migmatitic felsic granulites (Indares et al., 2008). A first set of pseudosections was constructed using the measured bulk composition of each sample that represents the final rock composition, and not the prograde evolution, because early melt was likely lost on the prograde path and prograde minerals were overprinted during peak temperature conditions and/or retrograde metamorphism. However, forward modeling demonstrates that different scenarios of melt loss do not have a significant effect on the supra-solidus topologies or on the compositions of solid phases (e.g., Groppo et al., 2012). Therefore, this set of pseudosections allows the exploration of the phase equilibria at near-peak granulite-facies conditions.

Estimated Peak conditions

The inferred peak assemblage of Pl ± Kfs + Qz + Grt ± Sil + L + Ilm ± Rt is stable from the solidus at amphibolite-facies conditions through UHT granulite-facies conditions, and so the peak P-T conditions cannot be inferred from the stable mineral assemblage alone. Overlaying isopleths for the grossular component of garnet from several samples should show peak P-T conditions where grossular isopleths intersect the peak mineral assemblage (Li et al., 2019). Calcium diffusion in garnet is much slower than Fe and Mg resulting in little change from peak conditions, whereas Fe and Mg diffusion rates are higher and probably capture retrograde conditions at the solidus (Chakraborty and Ganguly, 1992; Hollis et al., 2006; Li et al., 2019). I replicated this method using grossular isopleths for the five modeled samples (5-6, 11, 17LM04, AD01, 001HG) to find the P-T region of their intersection (e.g., Figure 23B,D). Figure 23E shows grossular isopleths that trace 95% confidence intervals for mineral composition data from

those five modeled samples (Table 3); these isopleths intersect in the region of ~1025°-1190° C and 12.5-18.5 kbar indicating that peak metamorphism took place at UHT granulite-facies conditions.

The igneous set of solution models and 0.12 wt. % H_2O were used to generate pseudosection and isopleth models (e.g., Figure 24A,C). The "peak" P-T field is determined at the approximate intersection of the peak mineral assemblage with the 95% confidence intervals for the grossular isopleths, and is limited in pressure to the Sil stability field. This process was repeated with 1.23 wt. % H_2O and using the metapelite set of solution models with both 0.12 and 1.23 wt. % H_2O. The estimated peak metamorphic conditions fall within the UHT granulite facies in all cases (e.g., Figure 24E).

Table 3. Grossular Content Statistics

Sample	Grs Mean across single grains (n)				Mean across all grains (N)		d.o.f	two-tailed t-test statistic	95% CI (incl. Mn)	95% CI (w/o. Mn)
	grain number	n	M_n	SD_n	M_N	SD_N	ν	$t_{\alpha=0.05,\nu}$	Grs/(Grs+Alm+Prp+Sps)	Grs/(Grs+Alm+Prp)
5-6	N=1	4	5.2	0.2	--	--	3	3.18	4.9 - 5.5	5.8-6.5
AD-01	1	37	7.54	0.33	7.25	0.18	14	2.16	7.4-7.7	8.3-8.8
	2	8	7.31	0.12						
	3	12	7.23	0.23						
	4	10	7.3	0.17						
	5	5	7.05	0.32						
	N=6	5	7.09	0.23						
17LM04	1	19	7.11	0.26	7.47	0.44	5	2.57	7.2-7.8	8.2-9.1
	2	15	7.07	0.23						
	3	3	7.08	0.12						
	4	3	7.64	0.04						
	5	3	8	0.12						
	6	3	8.16	0.05						
	7	2	8.04	0.31						
	8	3	7.55	0.09						
	9	3	7.46	0.19						
	10	4	7.33	0.23						
	11	4	7.52	0.24						
	N=12	14	6.72	0.24						
001-HG	1	2	5.97	0.16	5.87	0.13	1	12.07	4.7-7.1	5.4-8.2
	2	8	7.31	0.12						
11	1	2	6.99	0.56	6.56	0.4	2	4.3	5.7-7.4	6.6-8.6
	2	2	6.61	0.41						
	3	2	6.6	0.3						
	N=4	2	6.03	0.04						

Table 3. Approximate 95% confidence intervals are reported for garnet systems with and without spessartine (Mn endmember). Means across all grains are the average of means of single grains within a sample. Degrees of freedom (D.o.f) are estimated using the following: $\nu = n - 1$ *sample 5-6;* $\nu = N - 1$ *sample 001-HG ;* $\nu = \left(\sum {SD_n}^2/n\right)^2/(\sum {SD_n}^2/(n(n-1)))$ *samples 17LM04, AD-01, 11. 95% confidence intervals are determined as* $M \pm t_{\alpha,\nu} SD_N/\sqrt{N}$.

Figure 23. Pseudosections of Select Samples with Grossular Isopleths

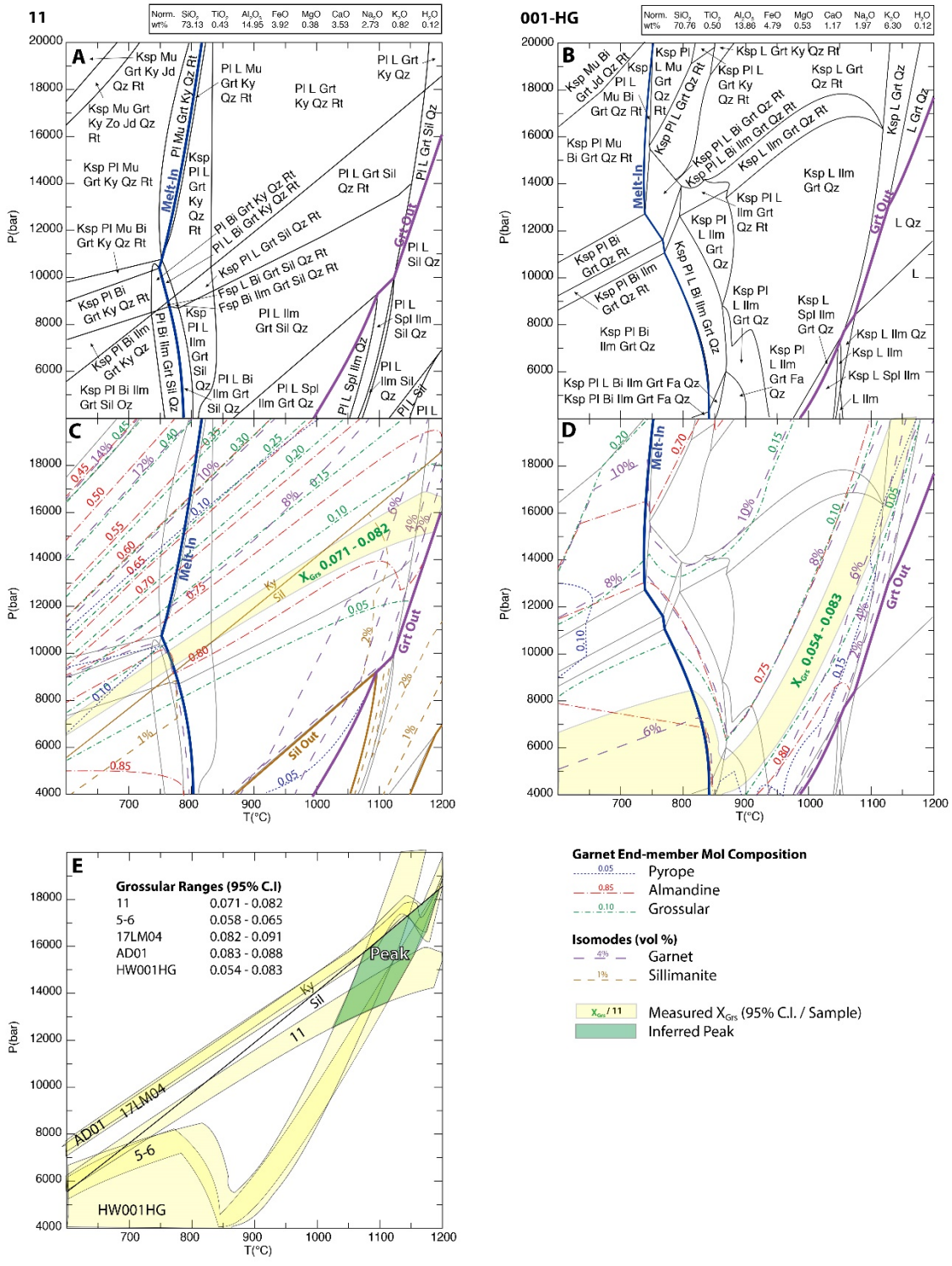

Figure 23. Pseudosections (A and C) calculated using the "igneous set" of solution models (see text) for representative samples 11 (A, B) and 001HG (C, D) showing equilibrium mineral assemblages across the range 600-1200° C and 4-20 kbar. B and D) Garnet end-member isopleths and modal percentages of sillimanite and garnet are superimposed on pseudosections A and B (mineral assemblages are removed for clarity). Yellow fields represent the 95% confidence intervals for the grossular component of garnet from mineral composition data (Table 3). E) Grossular components (95% C.I.) of garnets from samples 11, 001HG, AD01, 17LM04, and 5-6 compiled to show the region of intersection that represents the P-T conditions for peak metamorphism. Pseudosections and grossular data for AD01, 17LM04, and 5-6 are calculated but not shown; only their Grs ranges are shown in E.

A second set of pseudosections was generated using an average composition of select Ledge Mountain samples to better capture a whole-outcrop composition. The average migmatite composition is based on 11 granitic migmatite samples - 001HG, 003HG, 5-6, AD01a,b, 17LM02,-03,-04,-05,-06, and -07 (Table 4, Figure 24) that are all similar mineralogically and texturally. The "peak" fields in Figure 24E represent the combined results of all model sets (igneous and metapelite) and water contents (0.12 and 1.23 wt. %). Models based on this average composition are similar to those calculated for individual migmatite samples (e.g., Table 4).

Table 4. Whole-Rock Data for Samples Used in Model Calculation of the Average Pseudosection Diagram in Figure 24.

SAMPLE #	SiO_2	TiO_2	Al_2O_3	FeO	MnO	MgO	CaO	Na_2O	K_2O	P_2O_5
001-HG	70.04	0.5	13.72	4.74	0.03	0.52	1.16	1.95	6.24	0.1
003-HG	70.74	0.55	13.65	5.2	0.06	0.24	1.93	2.33	4.33	0.11
5-6	66.1	0.61	15.89	5.05	0.15	0.33	2.01	2.83	5.3	0.12
AD01a	71.71	0.59	14.08	4.53	0.08	0.5	1.94	1.78	3.59	0.11
AD01b	71.72	0.65	14.57	4.77	0.07	0.48	1.8	1.56	2.88	0.12
17LM02	70.52	0.57	13.78	4.03	0.02	0.28	0.76	2.23	6.37	0.08
17LM03	71.19	0.53	13.74	4.44	0.03	0.2	0.61	1.62	6.11	0.09
17LM04	69.34	0.64	15.42	4.72	0.09	0.56	1.93	1.76	3.99	0.12
17LM05	70.92	0.6	13.26	4.63	0.15	0.21	1.98	2.33	4.39	0.11
17LM06	70.15	0.55	13.98	4.55	0.03	0.45	1.07	2.5	5.06	0.09
17LM07	71.55	0.65	13.26	5.2	0.22	0.27	0.27	0.88	6.47	0.13
Mean	70.36	0.59	14.12	4.71	0.08	0.37	1.41	1.98	4.98	0.11
σ	1.6	0.05	0.85	0.35	0.06	0.14	0.65	0.54	1.23	0.01

Figure 24. Variation of Peak Fields by Water Content, Comparing Igneous and Metapelitic Model Sets

	SiO2	TiO2	Al2O3	FeO	MnO*	MgO	CaO	Na2O	K2O	H2O
Wt %	70.36	0.59	14.12	4.71	0.08	0.37	1.41	1.98	4.98	var

*Metapelite sets only

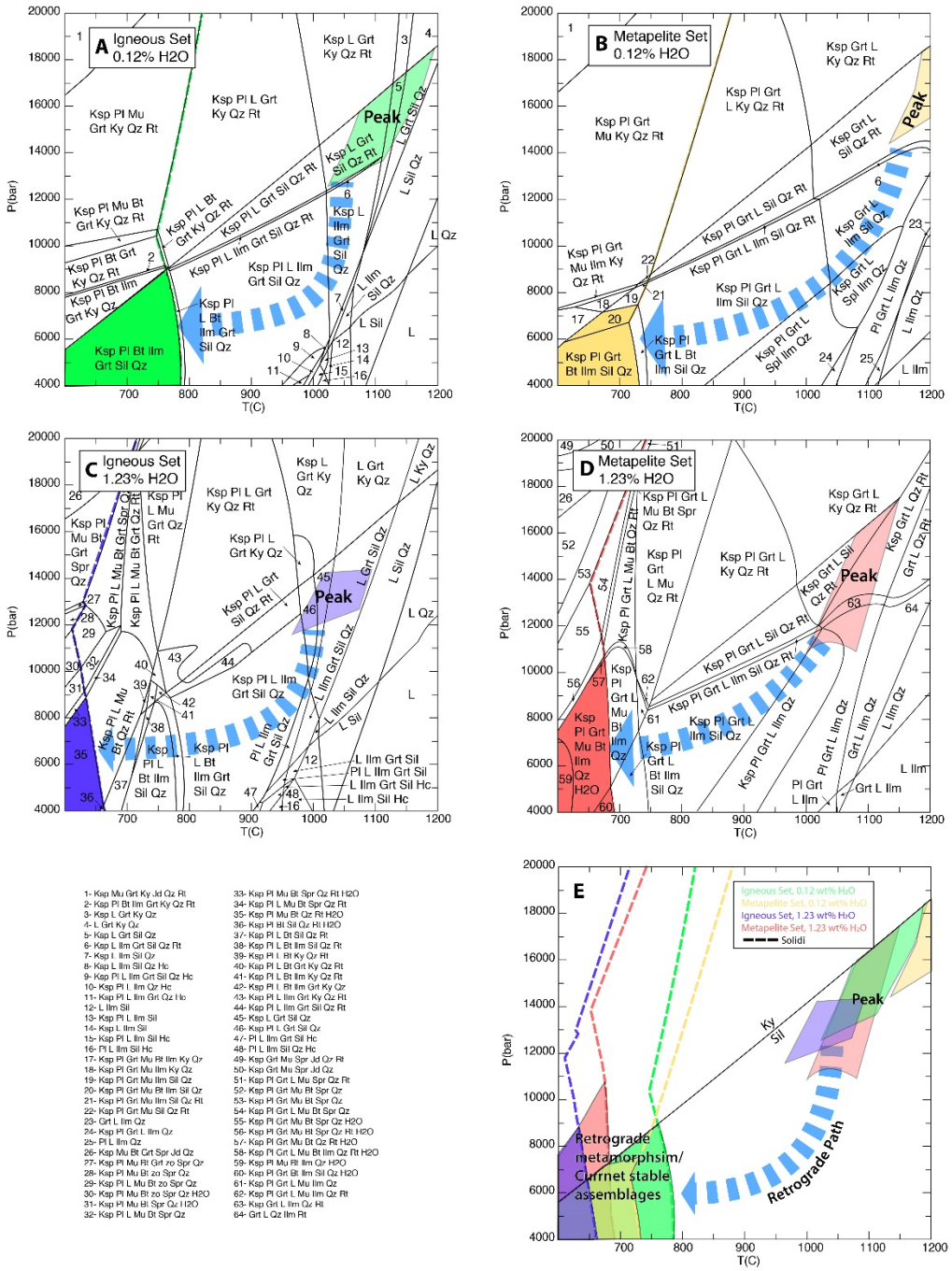

Figure 24. Pseudosections (A and C) calculated using the "igneous set" of solution models (see text) for representative samples 11 (A, B) and 001HG (C, D) showing equilibrium mineral assemblages across the range 600-1200° C and 4-20 kbar. B and D) Garnet end-member isopleths and modal percentages of sillimanite and garnet are superimposed on pseudosections A and B (mineral assemblages are removed for clarity). Yellow fields represent the 95% confidence intervals for the grossular component of garnet from mineral composition data (Table 3). E) Grossular components (95% C.I.) of garnets from samples 11, 001HG, AD01, 17LM04, and 5-6 compiled to show the region of intersection that represents the P-T conditions for peak metamorphism. Pseudosections and grossular data for AD01, 17LM04, and 5-6 are calculated but not shown; only their Grs ranges are shown in E.

My best estimate for peak metamorphism of Ledge Mountain migmatites is 1025-1190° C and 12.5-18 kbar that was established using the igneous solution models and 0.12 wt. % H_2O water (Figure 24A). Models using the metapelite set of solution models and 0.12 wt. % H_2O results in increased peak temperatures to >1140° C and represent maximum P-T conditions of metamorphism for Ledge Mountain migmatites (Figure 24B). Increasing water content to 1.23 wt. % in the igneous models resulted in a 60° C decrease in peak temperatures to a minimum of 960° C (Figure 24C). Combining the igneous model set with 1.23 wt. % H_2O lowered the peak metamorphic pressure to a minimum of 11 kbar (Figure 24D). For all models, the minimum conditions for peak metamorphism are 960° C and 11 kbar based on 1.23 wt. % water (Figure 24C, D). Results are summarized in Figure 24E.

Melt Reintegration

Observations of Ledge Mountain migmatites in thin section indicate evidence for at least 15-30% melt in most rocks. Migmatites begin to lose their pre-anatectic structures and develop flow foliations when they meet a critical melt fraction between 0.26 and 0.40 (also the melt escape threshold); in some

cases, this critical melt fraction is as low as 0.20 and is not normally more than 0.70 (Sawyer, 2008). The pseudosection models shown in Figures 23 and 24 are intended to represent the peak/high-temperature metamorphic history of Ledge Mountain migmatites, rather than the prograde history. If leucosome is in situ and no melt has been lost, then the bulk composition of homogenized migmatite samples represents the original protolith chemistry. If melt has been lost, the bulk composition of homogenized migmatite represents a melt depleted version of the protolith.

In Ledge Mountain samples, the melt volume observed in thin section and in models indicates that at least some melt has segregated away from its source, and up to 36% of the anatectic melt may have been lost from the system entirely (Sawyer, 2008). Furthermore, the topologies in the lower-temperature, higher-pressure part of the pseudosections do not account for melanosome biotite with higher TiO_2 contents, which may be of primary magmatic source (Figure 20), because biotite does not appear at prograde conditions in any pseudosections models (Figures 23, 24).

Melt reintegration approximates the prograde metamorphic history by revealing the estimated protolith composition and likely melt-loss volume on the P-T-t path (Bartoli, 2017). I use the single-step melt reintegration approach described by Bartoli (2017) and developed by Indares et al. (2008). Melt is reintegrated by adding fractions of the molar composition of the melt modeled at estimated peak P-T conditions (14 kbar, 1050˚C) back into the measured whole-rock composition using progressively higher melt fractions. Melt compositions can be estimated from nanogranite inclusions in large peritectic garnet grains using electron microprobe mineral composition data. I used the composition of the melt being generated at the estimated peak P-T conditions for Ledge Mountain migmatites (14 kbar, 1050^{o}C; Table 5). I reintegrated from 5% to 80% melt, corresponding to 4.8-44 vol. % melt loss, into the homogenized migmatite composition to test the effect on pseudosections of reintegrating melt.

Table 5. Melt-Reintegration Composition

	Homogenized Migmatite (Table 4) mol %	Melt Composition mol %	Melt-reintegrated Composition mol%	Melt-reintegrated Composition wt%
SiO_2	77.64	71.36	74.85	69.08
TiO_2	0.49	1.09	0.76	0.93
Al_2O_3	9.18	10.18	9.63	15.07
FeO	4.35	3.34	3.90	4.30
MgO	0.61	0.51	0.56	0.35
CaO	1.67	1.95	1.79	1.54
Na_2O	2.12	2.90	2.47	2.35
K_2O	3.50	4.66	4.02	5.82
H_2O	0.44	4.02	2.03	0.56

Table 5. Homogenized migmatite composition is recalculated as mol % from Table 4. Melt composition is determined form the homogenized migmatite composition at the inferred peak P-T conditions at 14 kbar, 1050˚C. Melt-reintegrated compositions calculated as Homogenized Migmatite + 0.80 Melt Composition in mol% and wt% are used for generating the prograde potion of the combined pseudosection in Figure 25.

Reintegrating 80% of the calculated melt composition into the modeled whole rock composition represents a protolith composition from which ~44 vol. % (80% melt/(80% melt+100% original whole-rock) was lost from the modeled rock. In the peak region, the minimum metamorphic temperature for the peak assemblage decreased 30° C to ~1020° C after reintegrating 80% melt, and the maximum pressure decreased by ~500 bars (Figure 25). While melt reintegration results in minor shifts in the pseudosection fields, the field representing the peak mineral assemblage is largely unchanged. I therefore infer that the modeled compositions do not differ significantly from the protolith composition, and the whole-rock compositions I used are a good proxy for peak compositions, even if significant melt (~44%) was lost from the system. Peak conditions are largely unchanged and are therefore reliable if modeled with the melt-depleted homogenized whole-rock chemistry.

The results show that reintegrating significant melt into the homogenized bulk rock chemistry stabilizes prograde biotite at higher pressures near the solidus along the presumed prograde path. I chose the 14 kbar isobar to represent prograde pressures so they match peak pressures. Pressure may have been higher or lower than 14 kbar during prograde metamorphism, but this is a reasonable estimate given the lack of constraints on prograde pressure. Before melt reintegration, biotite is stable at ~11 kbar (Figure 24A). With melt-reintegration, biotite stabilizes at 11 kbar + 1 kbar per 10% reintegrated melt. The biotite stability field reaches estimated prograde pressure (14 kbar) with ~30% reintegrated melt (8% melt loss model). At 80% melt reintegration, biotite appears near the solidus at higher pressures (up to ~19 kbar). To produce a pseudosection with a large biotite stability field at higher pressures, I chose the 80% melt-reintegrated pseudosection (44% melt-loss model) to represent prograde conditions. Melt-reintegration suggests that a minimum 8% melt was lost from the bulk-rock during prograde conditions, but the actual amount of melt lost could be much higher. Changing the amount of reintegrated melt (30-80%) has the effect of changing the size of the stability fields along the presumed prograde path, but not the stable minerals within the fields; the melt-reintegrated pseudosection allows for quantitative interpretation of the stable prograde assemblages.

P-T Path

I propose a clockwise P-T path consistent with prograde heating of mid-deep crustal rocks, peak conditions near 1050˚C and 14 kbar, near isothermal decompression, followed by near isobaric cooling (Figure 25).

The prograde path is approximated along the 14 kbar isobar starting at 600˚C and continuing to peak conditions. To satisfy the condition that some primary biotite is present in Ledge Mountain rocks, the prograde path passes through a biotite field at ~700˚C after crossing the solidus (Figure 20, 25). The slope of the prograde path is not meant to suggest that the prograde path was necessarily isobaric. If some decompression or burial occurred while heating, there would be little difference in the mineral assemblages along the prograde path. Without diagnostic evidence other than the possible presence of magmatic biotite, there is no way to determine the pressure/depth prior to peak conditions.

The retrograde path has two components. The near-isothermal decompression path begins at peak conditions and decreases in pressure and pressure by 6 kbar and 50˚C. The slope of the path is drawn approximately parallel to garnet mineral isopleths in Figure 23 to reflect the lack of garnet zoning in samples. The near-isobaric cooling path begins at the end of the near-isothermal decompression path at 8 kbar and 1000˚C and continues through the solidus ending at 6.5 kbar and 700˚C.

Figure 25. Proposed P-T Path through Prograde and Retrograde Pseudosections

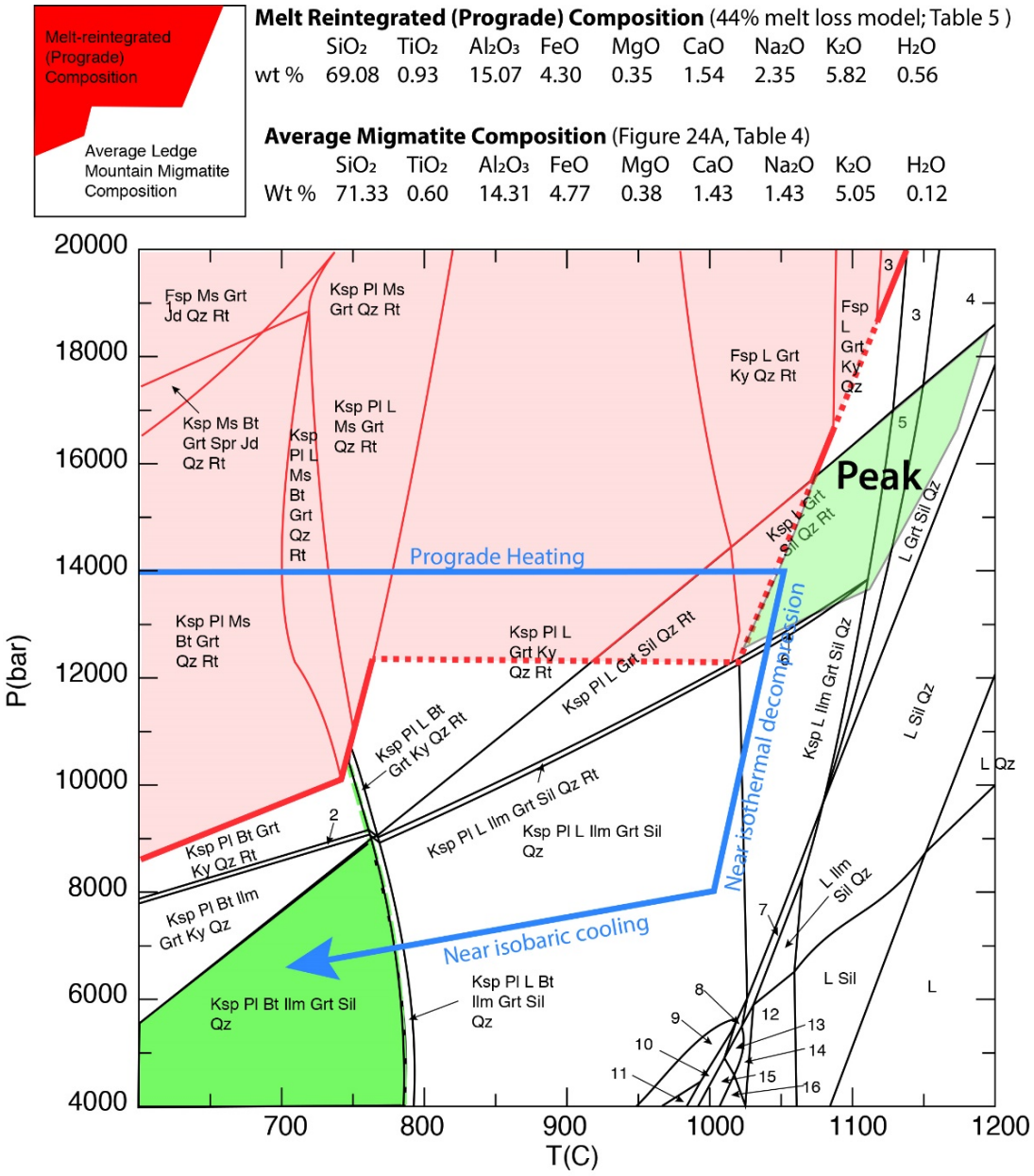

Figure 25. Proposed P-T path overlaid onto combined melt-reintegrated (red; Table 5) and homogenized whole-rock pseudosections (white; Table 4). The prograde path is contained in the melt-reintegrated portion of the pseudosection. The peak field, near-isothermal decompression path, and near-isobaric cooling path are contained within the homogenized whole-rock pseudosection. The red line shows the extent of melt-reintegrated pseudosection overlay; where it is dotted, the stable assemblage is the same on both sides of the line.

Net-transfer Reactions Along the P-T Path

I model melt and mineral modes along the proposed P-T path (Figure 25) to understand which metamorphic reactions may have occurred during the petrotectonic history of Ledge Mountain, I determine melt and mineral modes that appear in the modeled stable assemblages along the proposed P-T path (melt, Qz, Pl, Ksp, Grt, Bt, Ms, Ky, Sil, Ilm, and Rt; Figures 25, 26). Increasing and decreasing phase modes are assumed to assumed to be products and reactants respectively. Net-transfer reactions are identified along the prograde, near-isothermal decompression, and near-isobaric cooling parts of the presumed P-T path (Figure 25).

Prograde Net-Transfer Reactions

Melt and mineral modes along the prograde path are largely determined by how much melt I reintegrated back into the homogenized migmatite chemistry (80% melt reintegrated), and should not be taken literally because the degree of melt loss is highly uncertain. Melt volume grows steadily with increasing temperature after passing the solidus during prograde heating. At the solidus, the prograde segment of the P-T path passes through the assemblage Qz + Ksp + Pl + Grt + Bt + Ms. As heating continues four net-transfer reactions (2-5 below) occur during the prograde evolution.

From the solidus (~700˚C) to the point where biotite is no longer stable (~730˚C), garnet and K-feldspar volumes increase and mica, quartz and plagioclase volumes decrease (Figure 27). The modeled stable assemblage is consistent with vapor-absent dehydration melting of biotite and (rarely) muscovite to produce melt, with garnet and K-feldspar as peritectic phases:

Bt + Ms + Qz + Pl = Grt + Kfs + Melt [Reaction 2]

At ~730˚C garnet changes from growing to melting. Muscovite continues to undergo dehydration melting until ~790˚C where it destabilizes and a small volume of kyanite is produced. K-feldspar continues to grow with melt until ~790˚C. From ~730˚ to ~790˚C, garnet and muscovite melt to produce K-feldspar and an aluminosilicate (kyanite at these pressures) as peritectic phases:

Ms + Grt + Qz + Pl = Kfs + Ky + Melt [Reaction 3]

From ~790˚C to ~990˚C, garnet continues melting, K-feldspar maintains consistent volume, and kyanite melts slightly. No peritectic or solid phases are produced during this interval:

Grt + Ky + Qz + Pl = Melt [Reaction 4]

At 990˚C, the prograde path crosses from the kyanite stability field to the sillimanite stability field. The total volume of aluminosilicate increases and peritectic sillimanite is produced. Garnet and K-feldspar melt until modeled peak conditions (1050˚C):

Grt + Ky + Qz + Ksp = Sil + Melt [Reaction 5]

Near the end on the prograde history, a sharp increase in melt volume and large decrease in volume of all major phases should not be taken literally (Figure 26). The single step melt reintegration approach applies the same conditions along the entire prograde history (e.g., Groppo et al., 2012). In reality, the prograde composition close to peak conditions is closer to the composition prior to melt reintegration (i.e., after melt loss). In addition, the large discontinuities of all phase modes at peak P-T conditions do not reflect a rapid change in those mineral modes, but rather the abrupt change in modeled compositions.

Near-isothermal Decompression Net-transfer Reactions

During the entire near-isothermal decompression path, melt volume is relatively constant (~12±1 vol. %). Minor mineral modes are also relatively constant except when pressures decrease to ~12.5 kbar where sillimanite, ilmenite, and quartz grow at the expense of garnet and rutile (Figure 26):

Grt + Rt = Sil + Ilm + Qz [Reaction 6]

From ~10.5 to 8 kbar, a ~5 vol % decrease in K-feldspar corresponds to a similar magnitude increase in plagioclase volume.

Near-isobaric Cooling Net-transfer Reactions

Along the near-isobaric cooling path from 1000˚C to 790˚C plagioclase, quartz, and garnet crystalize from melt. K-feldspar decreases in volume over this interval, and its potassium

component must enter the melt phase at a slower rate than overall melt recrystallization, so overall melt remains a reactant phase:

Melt + Ksp = Pl + Qz + Grt [Reaction 7]

At 790˚C the retrograde path crosses into the biotite stability field, and reaches the retrograde solidus at ~775˚C. During this interval, garnet, ilmenite, and K-feldspar break down and the last fraction of melt recrystallizes to form biotite, sillimanite, plagioclase, and quartz.

Melt + Grt + Ilm + Ksp = Bt + Sil + Pl + Qz [Reaction 8]

Figure 26. Melt and Recrystallization Sequence the along P-T-t path

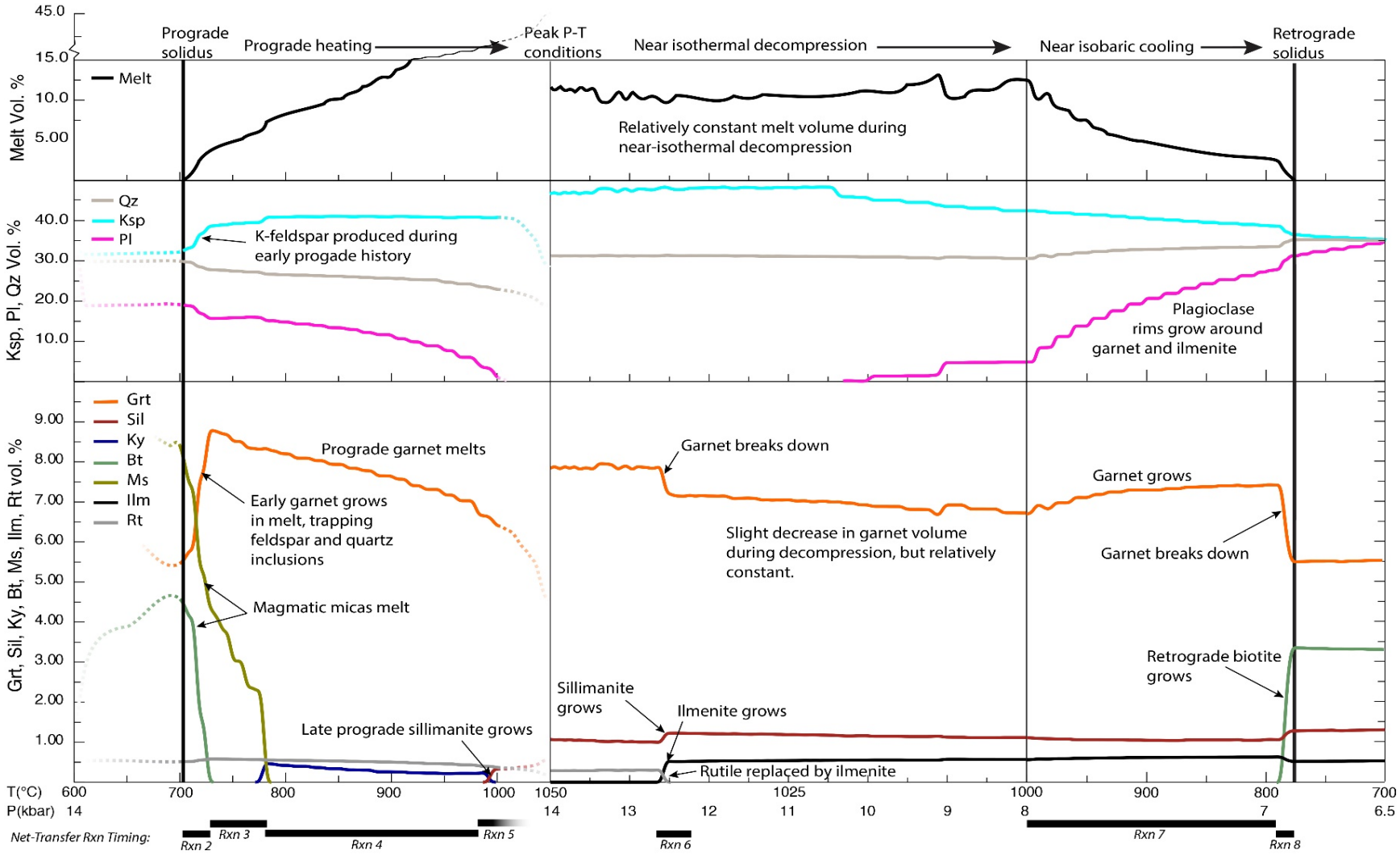

Figure 26. Melt and mineral modes modeled along the P-T-t path shown in Figure 25. The prograde section from 600˚C to 1050˚C (at 14 kbar) is modeled using the melt-reintegrated composition (44% melt loss model) and offers a qualitative assessment of mineral modes because the degree of melt loss (i.e., melt reintegrated) is highly uncertain. Melt and mineral modes after peak P-T conditions offer quantitative estimates assuming no additional melt-loss occurred. Relative timing of net-transfer reactions along the P-T-t path are indicated below the graph.

Zircon Analyses

Metzger et al. (in press) conduct U-Pb geochronology and trace element analyses of zircon on the Stanford-USGS SHRIMP-RG. Zircon domains are classified by texture: "magmatic" zircons exhibit oscillatory or sector zoning; "metamorphic" zircon have minimal cathodoluminescence; "anatectic" zircons have complex or chaotic zoning. Metamorphic and anatectic zircon have similar zoning patterns and ages, so these are combined. For detailed methodology for zircon analyses from Metzger, et al. (in press) see Appendix B.

Previous Geochronology

Dates for magmatic zircon domains range from early Shawinigan to early Ottawan (1176 Ma to 1079 Ma; Table 6; Figure 27; Reeder, 2017; Metzger et al., in press) with three exceptions found in sample HW008: two zircon cores within a leucocratic vein post-date the Rigolet phase, and one zircon rim in melanosome post-dates the Ottawan phase (Table 6; Figure 27; Reeder, 2017; Metzger et al., in press). Dates for zircon domains interpreted as metamorphic/anatectic range from just prior to the Ottawan phase to after the Rigolet phase (1099 to 832 Ma) except for an inherited zircon in melanosome (1144 Ma; Table 6; Figure 27; Reeder, 2017; Metzger et al., in press).

Ti-in-Zrn Thermometry

Experiments performed by Watson and Harrison (1983) predict the temperature of zircon crystallization based on the exchange reaction:

$$ZrSiO_4 + TiO_2 = ZrTiO_4 + SiO_2 \qquad \text{[Reaction 9]}$$

Assuming ideal fluid behavior where the activities of SiO_2 and TiO_2 are zero, then the relationship between the concentration of ^{48}Ti (P, in ppm) in zircon as a function of temperature (T_o, in Kelvin) is

$$T_o = \frac{E}{\log_{10}(P) - D} \quad \text{[Equation 3]}$$

where values for E = -4800±86 and D = 5.711±0.072 (Watson and Harrison, 1983). E and D are determined from a log(P) versus 1/T linear regression of the experimental results. Reported uncertainties are 95% confidence intervals (Watson and Harrison, 1983).

Ferry and Watson (2007) improved Equation 4 by adding corrections that included the activity of silica (a_{SiO_2}) and rutile (a_{TiO_2}):

$$T_c = \frac{E}{\log_{10} P - \log_{10} a_{TiO_2} + \log_{10} a_{SiO_2} - D} \quad \text{[Equation 4]}$$

The $\log(a)$ terms are considered corrections that account for activities less than 1. For simplicity, I will refer to T_o as the "uncorrected" temperature and T_c as the "corrected" temperature.

Ferry and Watson (2007) initially assumed that a_{TiO_2} varies between 0.6 and 0.9 and is rarely below 0.5 in rocks lacking rutile. However, model calculations of 14 different granite types at various pressures show a_{TiO_2} values fell far below 1 (~0.1 to 0.6; Ferry and Watson, 2007). Temperature corrections based on activity of rutile ($\Delta T_{a_{TiO_2}}$) and silica ($\Delta T_{a_{SiO_2}}$) can be approximated directly as

$$\Delta T_{a_{TiO_2}} = \frac{E}{-\log_{10} a_{TiO_2} - D} + \frac{E}{D}$$ [Equation 5]

and

$$\Delta T_{a_{SiO_2}} = \frac{E}{\log_{10} a_{SiO_2} - D} + \frac{E}{D}$$ [Equation 6]

Applying Equation 6 to the original a_{TiO_2} values of 0.6 and 0.9 only necessitates corrections of 34˚C and 7˚C, respectively. Including a_{TiO_2} values as low as 0.1, which is typical for some A-type, and a few I-type granites, results in corrections of up to 178˚C. Thus, the final corrected zircon temperatures from granites largely depends on the activity of rutile (Ferry and Watson, 2007; Schiller and Finger, 2019). Typical a_{SiO_2} values in granites are usually close to 1 (0.97 – 1.00), and result in corrections of no more than -2˚C (Equation 6). For simplicity, I assume a_{SiO_2} values of 1 for Ledge Mountain rocks.

Affinity values (A) are directly related to the activities (a) at the uncorrected temperatures (T_o) by

$$a = e^{\frac{-A}{RT_o}}$$ [Equation 7]

where R is the gas constant (8.314 J mol^{-1} K^{-1}). Substituting Equation 7 into Equation 4 with $a_{SiO_2} = 1$ yields:

$$T_c = \frac{E}{\log_{10} P + \frac{kA_{TiO_2}}{T_o} - D}$$ [Equation 8]

where $k = 1/(Rln10)$. I calculated affinity values with Rhyolite-MELTS (Table 6; Gualda et al., 2012; Ghiorso and Gualda, 2015). A sequence of activities from 11 to 15 kbar are generated in 0.2 kbar increments at the uncorrected temperature (T_o) using the average compositions from Table 4. Two zircon analyses (HW007B-38.1 and HW005A-5.1) had T_o values below 700°C which is outside the range of Rhyolite-MELTS, so those results were omitted.

Table 6: Summary of U-Th-Pb SHRIMP Geochronology and Ti-in-Zrn Thermometry of Ledge Mountain Zircons

	Spot Name	Zircon Domain	U-Th-Pb Dating Age (Ma)	^{48}Ti ppm	Uncorrected Temperature T_0 (˚C)	A_{TiO2} (J)	Corrected Temperature Tc (˚C).
Magmatic	HW001-1.1	Core	1097	16.9	797	1436	844
	HW005A-19.1	Mantle	1159	16.4	794	1389	865
	HW005A-9.1	Mantle	1152	10.4	750	986	817
	HW005B-37.1	Mantle	1107	10.2	747	959	814
	HW006A-34.2	Core	1123	11.3	757	870	825
	HW006A-36.2	Mantle	1079	9.6	742	923	809
	HW006B-30.1	Mantle	1176	17.6	802	1510	872
	HW006B-8.1	Core	1195	42.8	904	5575	981
	HW008A-2.1	Mantle	1099	8.0	725	858	808
Metamorphic/Anatectic	HW001-33.1	Rim	1060	9.9	745	3918	790
	HW004-10.1	Rim	1034	7.9	724	856	734
	HW004-13.1	Rim	1015	9.3	739	903	749
	HW004-24.1	Rim	1067	8.7	733	877	743
	HW004-27.1	Rim	1038	9.7	743	3882	788
	HW005A-10.1	Rim	969	9.4	739	913	750
	HW005A-24.1	Rim	1085	10.7	752	991	764
	HW005A-6.1	Rim	969	8.1	727	860	736
	HW005B-15.1	Rim	1026	8.3	729	867	738
	HW005B-3.1	Rim	1014	8.7	733	877	743
	HW005B-34.1	Rim	1049	8.8	734	884	744
	HW005B-9.1	Rim	1055	10.7	752	991	764
	HW006A-34.1	Rim	1009	9.8	744	3918	789
	HW006A-36.1	Rim	979	8.3	728	867	738
	HW006B-31.1	Rim	1033	9.7	743	3882	788
	HW006B-33.1	Rim	1038	10.5	750	976	762
	HW007A-1.1	Rim	1054	11.0	754	838	764
	HW007A-14.1	Rim	1012	12.3	766	997	777
	HW007A-19.1	Rim	1012	12.5	768	1012	779
	HW007A-24.1	Rim	1017	10.5	750	976	762
	HW007A-28.1	Core	1070	8.4	729	870	739
	HW007A-29.1	Rim	1040	12.8	769	1043	782
	HW007A-3.1	Rim	1026	9.8	744	3918	789
	HW007A-35.1	Mantle	900	8.1	726	860	736
	HW007A-8.1	Rim	996	10.4	749	969	761
	HW007B-1.1	Rim	972	8.6	732	877	742
	HW007B-1.2	Rim	1027	9.2	738	903	748
	HW007B-13.1	Rim	1023	11.0	755	838	764
	HW007B-18.1	Rim	1045	10.3	749	969	760

	HW007B-19.1	Rim	1041	11.0	755	838	764
	HW007B-24.1	Mantle	1052	10.5	751	976	762
	HW007B-23.1	Rim	1064	10.3	749	969	760
	HW007B-24.2	Core	1027	9.6	742	3882	787
	HW007B-26.1	Rim	1023	12.3	766	997	777
	HW007B-3.1	Rim	1043	10.4	750	969	761
	HW008A-10.1	Rim	996	8.0	726	858	735
	HW008A-25.1	Rim	1019	8.9	734	888	745
	HW008A-3.1	Rim	1012	12.0	763	952	774
	HW008A-5.1	Rim	1003	12.6	768	1028	780
	HW008B-19.1	Rim	1052	10.3	748	969	760
	HW008B-2.1	Rim	1099	11.4	758	879	768
	HW008B-25.1	Rim	1019	12.2	765	981	776
	HW008B-32.1	Rim	1049	11.0	755	838	764
	HW008B-39.1	Rim	991	11.9	763	937	773
Igneous	HW004-16.1*	Core	1101	9.8			
	HW005B-26.1*	Core	1144	13.9			
	HW008A-11.1*	Rim	1164	80.5			
	HW008A-23.1*	Rim	1017	11.4			
	HW008B-1.1*	Core	803	171.0			
	HW008B-24.1*	Core	654	150.1			
Metamorphic/Anatectic	HW001-20.1*	Rim	1006	0			
	HW001-29.1*	Rim	1042	11.8			
	HW001-30.1*	Rim	1017	12.7			
	HW001-4.1*	Rim	1008	10.0			
	HW001-7.1*	Core	935	25.8			
	HW004-20.1*	Core	948	19.0			
	HW005B-2.1*	Rim	936	9.1			
	HW008B-36.1*	Mantle	979	15.2			
	HW007B-38.1	Rim	1044	3.2			
	HW005A-5.1	Rim	959	5.2			

*Table 6. *Temperatures not determined due to bad Fe scans or Fe/Ti too high.*

Ti-in-zircon temperature estimates for magmatic zircon domains range from 809° to 981° C (Table 6; Figure 28), and record zircon closure temperatures during crystallization of magma (Corfu, 2003; Metzger et al., in press). Ti-in-zircon temperature estimates for metamorphic/anatectic zircon crystallization fall between 734° and 790˚C (Table 6; Figure 28), results that are ~200˚C cooler than estimated peak temperature conditions based on thermodynamic modeling. Ti-in-zircon thermometry is often applied to estimate peak

metamorphic conditions in granulites, but temperature results are often lower than those determined by Ti-in-rutile thermometry, Al-in-orthopyroxene thermobarometry, and thermodynamic modeling (Baldwin et al., 2007; Ewing et al., 2013; Kelsey and Hand, 2015; Clark et al., 2019). Several studies of UHT granulites show that zircon crystallization takes place on the retrograde cooling path at temperatures ~100-200˚C cooler than peak conditions (Baldwin et al., 2007; Ewing et al., 2013; Kelsey and Hand, 2015; Clark et al., 2019). The 734˚ to 790˚C temperatures for metamorphic/anatectic zircon growth are interpreted to represent zircon crystallization along the retrograde P-T-t path. A comprehensive error analysis of Ti-in-zircon temperatures is provided in Appendix C.

Figure 27: Ti-in-zircon temperatures (° C) vs. age (Ma) for different zircon domains.

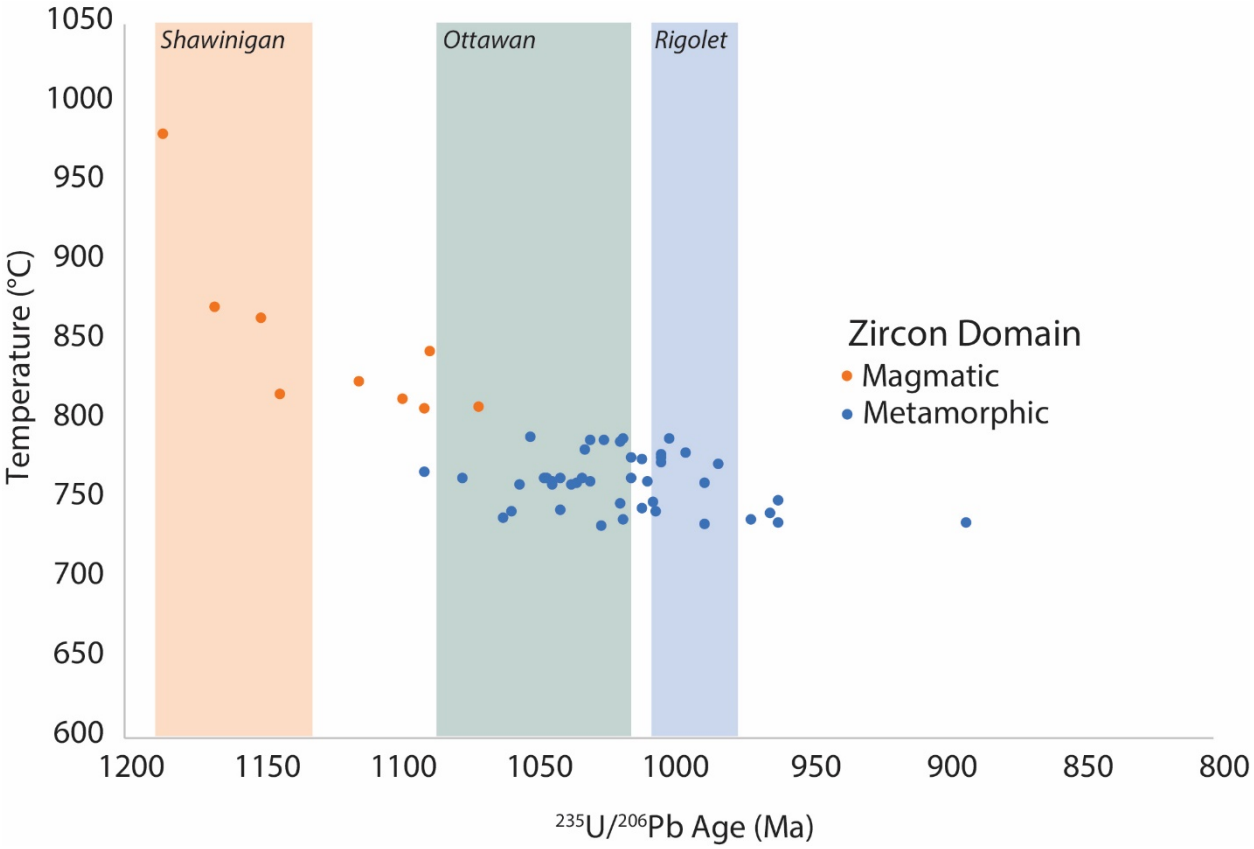

Figure 27. Metamorphic/anatectic zircons fall between 734° and 790° C. Zircon textures suggest Shawinigan to late-Ottawan "magmatic" zircon domains are magmatic in origin. The Ottawan to Rigolet-age domains have characteristics of metamorphic and/or anatectic zircon growth, and likely record retrograde temperature conditions from along the P-T-t path.

Discussion

Protolith Age and Composition

The U-Pb ages of zircons with magmatic origin from Ledge Mountain range from Shawinigan to early Ottawan (1195 – 1079 Ma), and are consistent with several possible interpretations for the protolith of Ledge Mountain migmatites. During the Shawinigan phase of the Grenville orogeny (1190 – 1140 Ma), the Adirondack Highlands experienced widespread intrusion of AMCG plutonic units (1180 – 1150 Ma; Chiarenzelli and McLelland, 1991; McLelland et al., 2004; Aleinikoff et al., 2021), emplacement of the Piseco Lake Gneiss (1200 – 1180 Ma; Valentino et al., 2019), and emplacement of the Marcy massif anorthosite (~1155 Ma; Peck et al., 2018). Recent evidence also suggests the Hawkeye Granite Gneiss (1160 – 1155 Ma), Lyon Mountain Granite Gneiss (1150 – 1145 Ma), and fayalite granite (~1145 Ma) intruded during the Shawinigan following AMCG plutonism (Aleinikoff et al., 2021), although other studies suggest Ottawan ages for these units (e.g., Chiarenzelli et al., 2017). If magmatic zircons represent the primary crystallization of a magma body that became the Ledge Mountain protolith, then emplacement of Ledge Mountain protolith occurred during the Shawinigan towards the end of emplacement of these plutonic units.

Other studies that determine Ottawan emplacement ages for the Lyon Mountain Granite Gneiss (~1050 Ma; Selleck et al., 2005; Chiarenzelli et al., 2017) and near-Ottawan emplacement of the Hawkeye Granite Gneiss (~1095 Ma; McLelland et al., 2004) suggest crustal reworking and emplacement of these granites was widespread during the waning stages of the Ottawan collisional orogeny (e.g., Selleck at al., 2005) and that Shawinigan aged zircon cores in those units are inherited from the partial melting of older plutonic rocks. The major and trace element whole rock geochemistry of Ledge Mountain migmatites closely resemble the Lyon

Mountain Granite Gneiss. Like the Lyon Mountain Granite Gneiss, xenocrystic zircon cores as old as 1195 Ma from Ledge Mountain migmatites are probably derived by partial melting of older plutonic rocks (Chiarenzelli et al., 2017).

Major and trace element whole-rock geochemistry of Ledge Mountain (Metzger et al., in press) closely resembles the Lyon Mountain Granite Gneiss and Hawkeye Granite Gneiss (Valley et al., 2011) and is consistent with an igneous protolith for Ledge Mountain migmatite. If Ledge Mountain had a metasedimentary protolith, then inherited zircon ages would be older to align with the ages of metasedimentary units in the Adirondack Highlands (>1220 Ma; Lupulescu et al., 2011; McLelland et al., 2013).

Ledge Mountain migmatites primarily represent an igneous protolith that partially melted in a deep crustal environment. Ledge Mountain migmatite is peraluminous while the Lyon Mountain Granite Gneiss is metaluminous (Metzger et al., in press). Frost and Frost (2011) suggest granitoids formed by partial melts of tonalites to granodiorites are more metaluminous at low pressures and more peraluminous at high pressures. Partial melting of Ledge Mountain migmatite at higher pressure conditions than for the Lyon Mountain Granite Gneiss could explain the peraluminous nature of the Ledge Mountain migmatite (Frost and Frost, 2011).

Timing of Metamorphism

U-Pb zircon ages interpreted as metamorphic in origin extend nearly continuously from the early Ottawan (1099 Ma) to post-Ottawan (969 Ma), except for a younger outlier dated 900 Ma. The ages indicate that Ledge Mountain experienced Ottawan to post-Ottawan metamorphism and anatexis (1099 to 969 Ma; Table 6; Figure 27). Post-Ottawan ages could either record the final crystallization of anatectic melt produced during metamorphism or

hydrothermal alteration that is reported elsewhere in the Highlands (e.g., McLelland et al., 2002). Hydrothermal alteration is unlikely because (1) zircons lack the textures typical of crystallization from hydrothermal fluids (Metzger et al., in press) and (2) Ledge Mountain biotite compositions do not plot in the "neoformed biotite" range on the Nachit et al. (2005; Figure 20) classification diagram, as would be the case if hydrothermal alteration had occurred. The lack of evidence for hydrothermal alteration suggests that zircon dates record the final crystallization of anatectic melt.

Timing of Biotite Growth

The compositional differences between biotite in different migmatite domains suggests differences in the timing and conditions of their formation. Biotite grains found in the melanosome matrix have higher TiO_2 contents and lower Mg numbers than those found in leucosome or associated with the breakdown products of garnet. The classification by Nachit et al. (2005) applies to primary magmatic biotite, primary magmatic biotite that has been re-equilibrated by late-magmatic fluids, and biotite that formed in equilibrium with hydrothermal fluids. The exact limits for each region may be unreliable given Ledge Mountain rocks experienced secondary heating and partial melting that were not considered in the Nachit et al. (2005) study. Sawyer (2008) recognizes similar trends in migmatites where primary biotite tends to have higher TiO_2 content and lower X_{FeO} values than those that formed or reequilibrated at lower temperatures. These compositional trends observed in Ledge Mountain biotite suggest grains found in the melanosome matrix formed at higher temperatures than those found in the leucosome or when garnet was breaking down.

Pseudosection modeling along the P-T path indicates one growth event of biotite during its metamorphic history, which occurs at lower-temperature, retrograde conditions (Figure 27). This event is represented by Reaction 8 where biotite forms at the expense of garnet. If there had been a higher temperature biotite growth event, it is not captured by pseudosection modeling during the metamorphic history, and may suggest that matrix biotite in the melanosome is an igneous relict, which formed before Ledge Mountain experienced metamorphism.

Peak P-T conditions

Estimated peak P-T conditions for the sillimanite-bearing migmatites ranged from 960° to >1200°C and 11-18 kbar, based on pseudosection models using both igneous and metapelite solution models, grossular isopleths, and variable H_2O contents (Figures 23, 24). The metapelite solutions models yield higher temperatures (1000˚ to >1200˚C; Figure 24B,D,E) than igneous models (960˚C to 1100˚C; Figure 24A,C,E). The upper bounds of both of these temperature ranges are among the highest reported for UHT terranes worldwide (e.g., Harley, 2004; Kelsey and Hand, 2015) and therefore seem unlikely for the Adirondack Highlands. However, minimum peak conditions of 960° – 1025˚C and 11 – 12.5 kbar determined using the igneous solution models (Figures 23, 24) – are consistent with recently reported P-T estimates of 950±40°C and 8.5-10 kbar for nearby Gore Mountain amphibolite based on conventional thermobarometry and thermodynamic modeling (Shinevar et al., 2020).

These estimates of peak conditions are compatible with extensive petrographic evidence for melting, and represent significantly higher metamorphic temperatures and pressures than previously reported for the Adirondacks Highlands (600-850° C and 6-8 kbar; e.g., Bohlen et al.,

1985; Spear and Markussen, 1997; Storm and Spear, 2005). These lower temperature conditions are used to constrain the retrograde conditions for Ledge Mountain granulites.

Melting and Crystallization Sequence

Prograde Path

Pseudosection modeling along the prograde path indicates large volumes of melt are generated due to dehydration melting of both biotite and muscovite (Reaction 2 and 3). Garnet generated early in the prograde history (Reaction 2; ~700˚ to 725˚C, 14 kbar) is consistent with the observed inclusions of plagioclase, k-feldspar, and quartz within some garnet cores (Figure 12), as garnet grew around those phases. However, subsequent melting from ~725˚C to modeled peak temperatures (1025˚C; Figure 27) indicates that much of the garnet generated early in the prograde history likely subsequently melted (Reactions 3-5). Late in the prograde history, sillimanite is produced along with a melt phase, and probably marks the first generation of sillimanite (Figure 11).

Near Isothermal Decompression

The observed mineral assemblages and pseudosection models suggest that the peak conditions start in the sillimanite stability field at UHT conditions (minimum 1050˚C, 11 kbar; Figure 24). Peak metamorphism and anatexis is followed by near isothermal decompression where the P-T path encounters Reaction 6 and garnet and rutile breakdown to form sillimanite, quartz, and rutile (Figure 27). This decompression reaction is indicated by the presence of ilmenite lamellae in rutile (Figure 7), relict rutile in garnet that is replaced by an opaque phase (likely ilmenite; Figure 9), and embayments of quartz in garnet (Figure 12). It is also possible

that this reaction marks the second generation of sillimanite growth (Figure 11), although models indicate a third possible episode of sillimanite growth closer to the solidus (Figure 27).

Near Isobaric Cooling

Near isothermal decompression is followed by isobaric cooling to retrograde conditions compatible with other studies in the Adirondack Highlands (600-850°C and 6-8 kbar; e.g., Bohlen et al., 1985; Spear and Markussen, 1997; Storm and Spear, 2005). The first reaction (7) encountered along the near isobaric cooling path is represented by the recrystallization of melt to form plagioclase. This is indicated by petrography showing rims of plagioclase on Fe-Ti oxides (Figure 7) and garnet (Figures 12, 17). Reaction 7 also suggests a second episode of garnet growth occurred during near isobaric cooling, with the first episode occurring during early prograde conditions. This may be captured in Figure 12, where a garnet grain has abundant inclusions in its core and few inclusions along its rim. The inclusion-rich core may represent prograde growth while the less-included rim may represent retrograde growth. Conversely, two episodes of garnet growth is not consistent with the observed lack of compositional zoning in garnet (Figure 17); and the slight ~1% increase garnet volume produced by Reaction 7, would likely be erased by subsequent garnet retrogression caused by Reaction 8.

Just before cooling to subsolidus temperatures, the last fraction of melt crystalizes and garnet, ilmenite, and K-feldsar break down to form biotite, sillimanite, plagioclase and quartz (Reaction 8). This final reaction in anatectic melt is indicated by relict garnet near its breakdown products within leucosome channels (Figure 12, 13), and biotite forming on the rims of more-intact garnet grains. Much of the biotite and sillimanite found in in leucosome channels was

likely produced by Reaction 8 during amphibolite-facies retrograde conditions from 775˚C to 750˚C and ~7 kbar (Figures 20, 27).

Exhumation of a Central Adirondack Gneiss Dome

Gravitational collapse and extension of orogenic belts causes vertical flow and exhumation of lower crustal rocks and has led to the formation of gneiss domes or double gneiss domes cored by high-grade metamorphic rocks including migmatites or granitoid rocks (e.g., (Whitney et al., 2004; Rey et al., 2011). Within the central Adirondack Highlands, Regan et al. (2019b) provided evidence that the Marcy anorthosite massif (Figure 1) is structurally overlain by a domal detachment zone that formed during the Ottawan phase 1070-1060 Ma and facilitated exhumation of lower crustal rocks.

Bohlen et al., (1985) report an 800˚C temperature anomaly ~5 km northeast of the Snowy Mountain anorthosite dome (Figure 1). Near Ledge Mountain and the Snowy Mountain anorthosite, Gore Mountain amphibolite experienced UHT granulite facies metamorphism (9–10 kbar, 950±40˚C; Shinevar et al., 2020). These exposures of anorthosite are evidence of a second, smaller, exposure of lower structural rocks that experienced granulite to UHT granulite facies metamorphism in the central Adirondack Highlands.

Ledge Mountain is surrounded by structures that are consistent with its development as a part of a domal structure in the Adirondack Highlands. A weak NE-dipping foliation indicates Ledge Mountain sits on the northern flank of the dome formed by Snowy Mountain (Figure 1 ; Geraghty, 1978). The Moose River Plain shear zone (MRPSZ) wraps around the Snowy Mountain dome then extends east toward Gore Mountain until its exposure is finally obscured. Chiarenzelli et al. (2007) and Valentino et al. (2008) suggest that the Snowy Mountain

anorthosite dome was exhumed by sinistral transpression along the MRPSZ. Similarly, migmatitic gneiss domes in the south Karakoram Mountains (northwest Himalaya, Pakistan) were exhumed mostly vertically with some sinistral movement in a compressional regime (Mahéo et al., 2004).

The Snowy Mountain and Oregon dome anorthosites, and the Gore Mountain amphibolite experienced granulite-facies metamorphism during the Ottawan orogeny at ca. 1031±30 Ma, 1048±10 Ma, and 1041±6 Ma, respectively (Hamilton et al., 2004). Similar timing for Gore Mountain garnets of 1047±6 Ma is supported by a Lu-Hf isochron age (Connolly, 2005; McLelland and Selleck, 2011). Ledge Mountain migmatites (ca. 1047.0±4.6 Ma; Metzger et al., in press) along with these other deep crustal rocks experienced high-grade metamorphism and melting during the Ottawan orogeny (Chiarenzelli and McLelland, 1991; Hamilton et al., 2004; McLelland and Selleck, 2011). The lower crust in the central Highlands at this time may have been weakened by anatexis and decompression melting which would have helped drive buoyant exhumation of these high-grade rocks (Rey et al., 2009; Vanderhaeghe, 2009), or pressure gradients developed by the onset of extension alone drove exhumation (Rey et al., 2009; Rey et al., 2011).

Two-dimensional numerical models of crustal extension demonstrate that converging viscous flow in the deep crust can lead to double gneiss domes separated by a high-strain zone (Rey et al., 2011). In the Rey et al. (2011) models, buoyancy driven uplift modeled with 34% melt at the onset of extension tended to develop a single dome regardless of extension rate (Rey et al., 2011). Exhumation controlled by pressure gradients, where buoyant forces are low and/or extension is fast, leads to double domes (Rey et al., 2011). At Ledge Mountain, the presence of in-situ melt and results of pseudosection modeling suggests that at least ~12% (up to 30+%) melt

was present at the onset of isothermal decompression, which is below the 34% modeled by Rey et al. (2011). The melt volume retained during isothermal decompression at Ledge Mountain exceeds the 5-7% melt connectivity transition required for ductile flow of these rocks, and initiate their buoyant uplift, but fall below the solid-to-liquid rheological transition that starts at 25-40% melt (Rosenberg and Handy, 2005). If melt fractions are on the high end of the modeled range (>30% melt), buoyancy would likely drive exhumation and would result in Ledge Mountain forming as a single dome structure, separate from the Marcy massif (Rey et al., 2011). A double dome can develop if extension, not buoyancy, is the primary driver of vertical flow, like the Montagne Noire in the French Massif Central or the Naxos dome (Cyclades Islands, Greece; Whitney et al., 2004; Rey et al., 2011). If Ledge Mountain is part of a double dome structure with the Marcy massif, it will be important to locate and document a high strain zone between the two.

Exposures of high-grade metamorphic rocks in large anorthosite bodies (Snowy Mountain, Oregon dome, and Humphrey Mountain), the Gore Mountain amphibolite, Lyon Mountain Granite Gneiss, and the Ledge Mountain migmatites, represent lower crustal rocks that exhumed together during Ottawan extension forming a second dome or sub dome in the central Adirondack Highlands. This broad domal region lies between the between the MRPSZ to the north and the Piseco Lake shear zone (a crustal-scale sinistral shear zone) to the south, and follows the structural grain of large-scale folds in the surrounding metasedimentary rocks (Figure 1).

Comparison to other Collisional Orogens and Thermodynamic Models

Collisional orogens worldwide that have experienced high pressure and/or UHT metamorphism show petrotectonic similarities to Ledge Mountain, the Adirondacks, and larger Grenville Province. The Bohemian massif of the Variscan orogen experienced P-T conditions of ~14 kbar and 900˚ to 1000˚C and has a peak mineral assemblage of Pl + Ksp + Qz + Grt + Ky + Rt (O'Brien, 2008; Kotková and Harley, 2010). Like the P-T-t history of Ledge Mountain, the Bohemian massif experienced dehydration melting of muscovite to produce kyanite as a peritectic phase (Reaction 3; Kotková and Harley, 2010) during prograde metamorphism, followed by isothermal decompression and isobaric cooling. Any kyanite present in Ledge Mountain migmatites converted to sillimanite at higher temperatures (Reaction 5); the abundant sillimanite and scarcity of kyanite in Ledge Mountain rocks is evidence that Ledge Mountain rocks experienced slightly higher-temperature peak metamorphic conditions than the Bohemian massif. The migmatitic gneisses of the Antarctic UHT granulite-facies terraces also experienced UHT metamorphic conditions (12 kbar, 1050˚C) similar to those experienced by Ledge Mountain migmatites and followed similar isothermal decompression and cooling paths (Harley, 1998, 2008). The felsic granulites of the Eastern Ghats, India, also follow a clockwise P-T path with UHT peak metamorphic conditions (~7–8 kbar and 950˚ –1030°C; Kelsey et al., 2017).

Thermomechanical modeling of lower crust within a Grenville-type orogenic core yields peak metamorphic P-T conditions of 11.9 kbar and 985˚C and steep, near-isothermal decompression paths during exhumation resulting from vertical ductile thinning (Jamieson and Beaumont, 2011). Similar models of Greater Himalayan Sequence rocks yield a similar counter-clockwise P-T-t path, but predicts conditions less than UHT metamorphism (Jamieson et al., 2007). Ledge Mountain migmatites represent rocks that were metamorphosed lower in the crust

and at hotter conditions than the Greater Himalayan Sequence rocks, consistent with our modeled peak metamorphic P-T conditions. UHT metamorphism and the clockwise P-T-t path reported for Ledge Mountain are consistent with supercontinent assembly (e.g., Santosh et al., 2011; Touret et al., 2016) and the Large Hot Orogen model explains the prolonged metamorphism during the Grenville orogeny (Harley, 2008; Rivers, 2009, 2012, 2015).

Conclusion

A multifaceted approach involving mineral chemical analysis, petrography, thermodynamic pseudosection modeling, and Ti-in-zircon thermometry reveals a clockwise P-T-t path where Ledge Mountain migmatites experienced prograde heating, peak metamorphic P-T conditions of ≥960°C and 11 to 18 kbar, near isothermal decompression, and isobaric cooling. Zircon geochronology and major and trace element analyses suggest an igneous protolith to the Ledge Mountain migmatites was emplaced toward the end-of and following the Shawinigan after AMCG plutonism and close in timing to the emplacement of other intrusive units (e.g., Lyon Mountain Granite Gneiss and Hawkeye Granite Gneiss) throughout the Adirondack Highlands. Zircon geochronology also suggests that Ledge Mountain migmatites were metamorphosed during the Ottawan-aged contraction and exhumation driven by buoyancy and/or pressure gradients related to regional extension. Structures surrounding Ledge Mountain and the results of this study suggest that Ledge Mountain sits on the flanks of a dome that is cored by rocks that experienced UHT metamorphism and may be part of a double dome with the Marcy anorthosite massif. Further field work conducted between Ledge Mountain and Marcy massif would help to clarify their relationship.

References

Aleinikoff, J., and Walsh, G., 2015, A new interpretation for the ages of Adirondack plutonism: Implications for the nature and timing of Mesoproterozoic deformation and plutonism, *in* Geological Society of America Abstracts with Programs, v. 47, p. 722.

Aleinikoff, J.N., Walsh, G.J., and McAleer, R.J., 2021, New interpretations of the ages and origins of the Hawkeye Granite Gneiss and Lyon Mountain Granite Gneiss, Adirondack Mountains, NY: Implications for the nature and timing of Mesoproterozoic plutonism, metamorphism, and deformation: Precambrian Research, v. 358, p. 106112, doi:10.1016/j.precamres.2021.106112.

Baldwin, J.A., Brown, M., and Schmitz, M.D., 2007, First application of titanium-in-zircon thermometry to ultrahigh-temperature metamorphism: Geology, v. 35, p. 295, doi:10.1130/G23285A.1.

Barth, A.P., and Wooden, J.L., 2010, Coupled elemental and isotopic analyses of polygenetic zircons from granitic rocks by ion microprobe, with implications for melt evolution and the sources of granitic magmas: Chemical Geology, v. 277, p. 149–159, doi:10.1016/j.chemgeo.2010.07.017.

Bartoli, O., 2017, Phase equilibria modelling of residual migmatites and granulites: An evaluation of the melt-reintegration approach: Journal of Metamorphic Geology, v. 35, p. 919–942, doi:10.1111/jmg.12261.

Bickford, M.E., McLelland, J.M., Selleck, B.W., Hill, B.M., and Heumann, M.J., 2008, Timing of anatexis in the eastern Adirondack Highlands: Implications for tectonic evolution during ca. 1050 Ma Ottawan orogenesis: Geological Society of America Bulletin, v. 120, p. 950–961, doi:10.1130/B26309.1.

Black, L.P. et al., 2004, Improved 206Pb/238U microprobe geochronology by the monitoring of a trace-element-related matrix effect; SHRIMP, ID–TIMS, ELA–ICP–MS and oxygen isotope documentation for a series of zircon standards: Chemical Geology, v. 205, p. 115–140, doi:10.1016/j.chemgeo.2004.01.003.

Bohlen, S.R., and Essene, E.J., 1977, Feldspar and oxide thermometry of granulites in the Adirondack Highlands: Contributions to Mineralogy and Petrology, v. 62, p. 153–169, doi:10.1007/BF00372874.

Bohlen, S.R., Essene, E.J., and Hoffman, K.S., 1980, Update on feldspar and oxide thermometry in the Adirondack Mountains, New York: GSA Bulletin, v. 91, p. 110–113, doi:10.1130/0016-7606(1980)91<110:UOFAOT>2.0.CO;2.

Bohlen, S.R., Valley, J.W., and Essene, E.J., 1985, Metamorphism in the Adirondacks. I. Petrology, Pressure and Temperature: Journal of Petrology, v. 26, p. 971–992, doi:10.1093/petrology/26.4.971.

Boone, G.M., 1978, Kyanite in Adirondack Highlands sillimanite rich gneiss and PT estimates of metamorphism: Geological Society of America Abstracts with Program, v. 10.

Bose, S., Das, K., Ohnishi, I., Torimoto, J., Karmakar, S., Shinoda, K., and Dasgupta, S., 2009, Characterization of oxide assemblages of a suite of granulites from Eastern Ghats Belt, India: Implication to the evolution of C–O–H–F fluids during retrogression: Lithos, v. 113, p. 483–497, doi:10.1016/j.lithos.2009.05.029.

Carvalho, B.B., Bartoli, O., Satish-Kumar, M., Kawakami, T., Hokada, T., Alvaro, M., and Cesare, B., 2021, Generation of highly silicic magmas at ultra-high temperature conditions: evidence from melt inclusions in peritectic garnet: , p. 1.

Chakraborty, S., and Ganguly, J., 1992, Cation diffusion in aluminosilicate garnets: experimental determination in spessartine-almandine diffusion couples, evaluation of effective binary diffusion coefficients, and applications: Contributions to Mineralogy and Petrology, v. 111, p. 74–86, doi:10.1007/BF00296579.

Chiarenzelli, J.R., and McLelland, J.M., 1991, Age and Regional Relationships of Granitoid Rocks of the Adirondack Highlands: The Journal of Geology, v. 99, p. 571–590, doi:10.1086/629518.

Chiarenzelli, J., Selleck, B., Lupulescu, M., Regan, S., Bickford, M.E., Valley, P., and McLelland, J., 2017, Lyon Mountain ferroan leucogranite suite: Magmatic response to extensional thinning of overthickened crust in the core of the Grenville orogen: GSA Bulletin, doi:10.1130/B31697.1.

Clark, C., Taylor, R.J.M., Johnson, T.E., Harley, S.L., Fitzsimons, I.C.W., and Oliver, L., 2019, Testing the fidelity of thermometers at ultrahigh temperatures: Journal of Metamorphic Geology, v. 37, p. 917–934, doi:10.1111/jmg.12486.

Coble, M.A., Vazquez, J.A., Barth, A.P., Wooden, J., Burns, D., Kylander-Clark, A., Jackson, S., and Vennari, C.E., 2018, Trace Element Characterisation of MAD-559 Zircon Reference Material for Ion Microprobe Analysis: Geostandards and Geoanalytical Research, v. 42, p. 481–497, doi:10.1111/ggr.12238.

Connolly, J.A.D., 2005, Computation of phase equilibria by linear programming: A tool for geodynamic modeling and its application to subduction zone decarbonation: Earth and Planetary Science Letters, v. 236, p. 524–541, doi:10.1016/j.epsl.2005.04.033.

Corfu, F., 2003, Atlas of Zircon Textures: Reviews in Mineralogy and Geochemistry, v. 53, p. 469–500, doi:10.2113/0530469.

Dasgupta, S., Bose, S., Bhowmik, S.K., and Sengupta, P., 2017, The Eastern Ghats Belt, India, in the context of supercontinent assembly: Geological Society, London, Special Publications, v. 457, p. 87–104, doi:10.1144/SP457.5.

Ewing, T.A., Hermann, J., and Rubatto, D., 2013, The robustness of the Zr-in-rutile and Ti-in-zircon thermometers during high-temperature metamorphism (Ivrea-Verbano Zone, northern Italy): Contributions to Mineralogy and Petrology, v. 165, p. 757–779, doi:10.1007/s00410-012-0834-5.

Ferri, F., Cesare, B., Bartoli, O., Ferrero, S., Palmeri, R., Remusat, L., and Poli, S., 2020, Melt inclusions at MT. Edixon (Antarctica): Chemistry, petrology and implications for the evolution of the Lanterman range: Lithos, v. 374–375, p. 105685, doi:10.1016/j.lithos.2020.105685.

Ferry, J.M., and Watson, E.B., 2007, New thermodynamic models and revised calibrations for the Ti-in-zircon and Zr-in-rutile thermometers: Contributions to Mineralogy and Petrology, v. 154, p. 429–437, doi:10.1007/s00410-007-0201-0.

Fuhrman, M.L., and Lindsley, D.H., 1988, Ternary-feldspar modeling and thermometry: American Mineralogist, v. 73, p. 201–215.

Gates, A.E., Valentino, D.W., Chiarenzelli, J.R., Solar, G.S., and Hamilton, M.A., 2004, Exhumed Himalayan-type syntaxis in the Grenville orogen, northeastern Laurentia: Journal of Geodynamics, v. 37, p. 337–359, doi:10.1016/j.jog.2004.02.011.

Geraghty, 1978, SE Portion Blue Mountain 15' Quadrangle, New York: New York State Geological Survey.

Ghiorso, M.S., and Gualda, G.A.R., 2015, An H2O–CO2 mixed fluid saturation model compatible with rhyolite-MELTS: Contributions to Mineralogy and Petrology, v. 169, p. 53, doi:10.1007/s00410-015-1141-8.

Gianola, O., Bartoli, O., Ferri, F., Galli, A., Ferrero, S., Capizzi, L.S., Liebske, C., Remusat, L., Poli, S., and Cesare, B., 2020, Anatectic melt inclusions in ultra high temperature granulites: Journal of Metamorphic Geology, p. jmg.12567, doi:10.1111/jmg.12567.

Groppo, C., Rolfo, F., and Indares, A., 2012, Partial melting in the higher Himalayan crystallines of Eastern Nepal: the effect of decompression and implications for the 'channel flow' model: Journal of Petrology, v. 53, p. 1057–1088, doi:10.1093/petrology/egs009.

Gualda, G.A.R., Ghiorso, M.S., Lemons, R.V., and Carley, T.L., 2012, Rhyolite-MELTS: a Modified Calibration of MELTS Optimized for Silica-rich, Fluid-bearing Magmatic Systems: Journal of Petrology, v. 53, p. 875–890, doi:10.1093/petrology/egr080.

Hamilton, M.A., McLelland, J., Selleck, B., and Tollo, R., 2004, SHRIMP U-Pb zircon geochronology of the anorthosite-mangerite-charnockite-granite suite, Adirondack Mountains, New York: Ages of emplacement and metamorphism: Memoirs-Geological Society of America, p. 337–356.

Harley, S.L., 2004, Extending our understanding of Ultrahigh temperature crustal metamorphism: Journal of Mineralogical and Petrological Sciences, v. 99, p. 140–158, doi:10.2465/jmps.99.140.

Harley, S.L., 2008, Refining the P–T records of UHT crustal metamorphism: Journal of Metamorphic Geology, v. 26, p. 125–154, doi:10.1111/j.1525-1314.2008.00765.x.

Harley, S.L., 1998, Ultrahigh temperature granulite metamorphism (1050 °C, 12 kbar) and decompression in garnet (Mg70)–orthopyroxene–sillimanite gneisses from the Rauer Group, East Antarctica: Journal of Metamorphic Geology, v. 16, p. 541–562, doi:10.1111/j.1525-1314.1998.00155.x.

Hasalová, P., Štípská, P., Powell, R., Schulmann, K., Janoušek, V., and Lexa, O., 2007, Transforming mylonitic metagranite by open-system interactions during melt flow: Journal of Metamorphic Geology, doi:10.1111/j.1525-1314.2007.00744.x.

Heimann, A., Spry, P.G., and Teale, G.S., 2005, Zincian spinel associated with metamorphosed proterozoic base-metal sulfide occurrences, Colorado: A re-evaluation of gahnite composition as a guide in exploration: The Canadian Mineralogist, v. 43, p. 601–622, doi:10.2113/gscanmin.43.2.601.

Holland, T.J.B., Green, E.C.R., and Powell, R., 2018, Melting of Peridotites through to Granites: A Simple Thermodynamic Model in the System KNCFMASHTOCr: Journal of Petrology, v. 59, p. 881–900, doi:10.1093/petrology/egy048.

Holland, T., and Powell, R., 2011, An improved and extended internally consistent thermodynamic dataset for phases of petrological interest, involving a new equation of state for solids: Journal of Metamorphic Geology, v. 29, p. 333–383, doi:10.1111/j.1525-1314.2010.00923.x.

Hollis, J.A., Harley, S.L., White, R.W., and Clarke, G.L., 2006, Preservation of evidence for prograde metamorphism in ultrahigh-temperature, high-pressure kyanite-bearing granulites, South Harris, Scotland: Journal of Metamorphic Geology, v. 24, p. 263–279, doi:10.1111/j.1525-1314.2006.00636.x.

Hoskin, P.W.O., and Schaltegger, U., 2003, The Composition of Zircon and Igneous and Metamorphic Petrogenesis: Reviews in Mineralogy and Geochemistry, v. 53, p. 27–62, doi:10.2113/0530027.

Indares, A., White, R.W., and Powell, R., 2008, Phase equilibria modelling of kyanite-bearing anatectic paragneisses from the central Grenville Province: Journal of Metamorphic Geology, v. 26, p. 815–836, doi:10.1111/j.1525-1314.2008.00788.x.

Ireland, T.R., and Williams, I.S., 2003, Considerations in Zircon Geochronology by SIMS: Reviews in Mineralogy and Geochemistry, v. 53, p. 215–241, doi:10.2113/0530215.

Isachsen, C., Livi, K., and Muller, P., 2004, Unraveling growth history of zircon in anatectites from the northeast Adirondack Highlands, New York: Constraints on pressure-temperature-time paths: Proterozoic Tectonic Evolution of the Grenville Orogen in North America, p. 267.

Jamieson, R.A., and Beaumont, C., 2011, Coeval thrusting and extension during lower crustal ductile flow - implications for exhumation of high-grade metamorphic rocks: Coeval thrusting and extension: Journal of Metamorphic Geology, v. 29, p. 33–51, doi:10.1111/j.1525-1314.2010.00908.x.

Jamieson, R.A., Beaumont, C., Nguyen, M.H., and Culshaw, N.G., 2007, Synconvergent ductile flow in variable-strength continental crust: Numerical models with application to the western Grenville orogen: NUMERICAL MODEL FOR GRENVILLE OROGEN: Tectonics, v. 26, p. n/a-n/a, doi:10.1029/2006TC002036.

JMP, 2019, Cary, NC, SAS Institute Inc.

Johnson, D.M., Hooper, P.R., and Conrey, R.M., 1999, XRF Analysis of Rocks and Minerals for Major and Trace Elements on a Single Low Dilution Li-tetraborate Fused Bead: v. 2, p. 25.

Kelsey, D.E., and Hand, M., 2015, On ultrahigh temperature crustal metamorphism: Phase equilibria, trace element thermometry, bulk composition, heat sources, timescales and tectonic settings: Geoscience Frontiers, v. 6, p. 311–356, doi:10.1016/j.gsf.2014.09.006.

Kelsey, D.E., Morrissey, L.J., Hand, M., Clark, C., Tamblyn, R., Gaehl, A.A., and Marshall, S., 2017, Significance of post-peak metamorphic reaction microstructures in the ultrahigh temperature Eastern Ghats Province, India: Journal of Metamorphic Geology, v. 35, p. 1081–1109, doi:10.1111/jmg.12277.

Kendrick, J., and Indares, A., 2018, The reaction history of kyanite in high- *P* aluminous granulites: Journal of Metamorphic Geology, v. 36, p. 125–146, doi:10.1111/jmg.12286.

Kotková, J., and Harley, S.L., 2010, Anatexis during High-pressure Crustal Metamorphism: Evidence from Garnet–Whole-rock REE Relationships and Zircon–Rutile Ti–Zr Thermometry in Leucogranulites from the Bohemian Massif: Journal of Petrology, v. 51, p. 1967–2001, doi:10.1093/petrology/egq045.

Lechler, P.J., and Desilets, M.O., 1987, A review of the use of loss on ignition as a measurement of total volatiles in whole-rock analysis: Chemical Geology, v. 63, p. 341–344, doi:10.1016/0009-2541(87)90171-9.

Li, X., White, R.W., and Wei, C., 2019, Can we extract ultrahigh-temperature conditions from Fe-rich metapelites? An example from the Khondalite Belt, North China Craton: Lithos, v. 328–329, p. 228–243, doi:10.1016/j.lithos.2019.01.032.

Ludwig, K.R., 2009, Squid 2, A user's manual: Berkeley Geochronology Center Special Publication 5, 110 p.:

Ludwig, K.R., 2012, User's manual for Isoplot 3.75: A geochronological toolkit for Microsoft Excel, Berkeley Geochronology Center Special Publication 5, 75 p.:

Lupulescu, M.V., Chiarenzelli, J.R., Pullen, A.T., and Price, J.D., 2011, Using pegmatite geochronology to constrain temporal events in the Adirondack Mountains: Geosphere, v. 7, p. 23–39, doi:10.1130/GES00596.1.

McDonough, W.F., and Sun, S. -s., 1995, The composition of the Earth: Chemical Geology, v. 120, p. 223–253, doi:10.1016/0009-2541(94)00140-4.

McLelland, J.M., Bickford, M.E., Hill, B.M., Clechenko, C.C., Valley, J.W., and Hamilton, M.A., 2004, Direct dating of Adirondack massif anorthosite by U-Pb SHRIMP analysis of igneous zircon: Implications for AMCG complexes: Geological Society of America Bulletin, v. 116, p. 1299–1317, doi:10.1130/B25482.1.

McLelland, J., Daly, J.S., and McLelland, J.M., 1996, The Grenville Orogenic Cycle (ca. 1350-1000 Ma): an Adirondack perspective: Tectonophysics, v. 265, p. 1–28, doi:10.1016/S0040-1951(96)00144-8.

McLelland, J., Hamilton, M., Selleck, B., McLelland, J., Walker, D., and Orrell, S., 2001, Zircon U-Pb geochronology of the Ottawan Orogeny, Adirondack Highlands, New York: regional and tectonic implications: Precambrian Research, v. 109, p. 39–72, doi:10.1016/S0301-9268(01)00141-3.

McLelland, J.M., and Selleck, B.W., 2011, Megacrystic Gore Mountain–type garnets in the Adirondack Highlands: Age, origin, and tectonic implications: Geosphere, v. 7, p. 1194–1208, doi:10.1130/GES00683.1.

McLelland, J.M., Selleck, B.W., and Bickford, M.E., 2013, Tectonic Evolution of the Adirondack Mountains and Grenville Orogen Inliers within the USA: Geoscience Canada, v. 40, p. 318, doi:10.12789/geocanj.2013.40.022.

Metzger, E.F., 1980, Investigation of Partial Melting at Ledge Mountain, Central Adirondacks, New York: [M.S. Thesis]: Syracuse: Syracuse University, 105 p.,.

Metzger, E., Leech, M., Swanson, B., Reeder, J., and Waring, H., in press, First evidence of high-pressure/ultrahigh temperature granulite-facies metamorphism in the Adirondack Highlands: Geosphere,.

Montel, J.-M., Weber, C., and Pichavant, M., 1986, Biotite-sillimanite-spinel assemblages in high-grade metamorphic rocks : occurrences, chemographic analysis and thermobarometric interest: Bulletin de Minéralogie, v. 109, p. 555–573, doi:10.3406/bulmi.1986.7958.

Nachit, H., Ibhi, A., Abia, E.H., and Ben Ohoud, M., 2005, Discrimination between primary magmatic biotites, reequilibrated biotites and neoformed biotites: Comptes Rendus Geoscience, v. 337, p. 1415–1420, doi:10.1016/j.crte.2005.09.002.

O'Brien, P.J., 2008, Challenges in high-pressure granulite metamorphism in the era of pseudosections: reaction textures, compositional zoning and tectonic interpretation with examples from the Bohemian Massif: Journal of Metamorphic Geology, v. 26, p. 235–251, doi:10.1111/j.1525-1314.2007.00758.x.

Peck, W.H., Selleck, B.W., Regan, S.P., Howard, G.E., and Kozel, O.O., 2018, In-situ dating of metamorphism in Adirondack anorthosite: American Mineralogist, v. 103, p. 1523–1529, doi:10.2138/am-2018-6481.

Postel, A.W., 1952, Geology of the Clinton County magnetite district, New York: United States Government Printing Office, 88 p.

Reeder, J.V., 2017, Formation of Kyanite-bearing migmatites in the Central Adirondacks: San Francisco State University, 96 p.

Regan, S., Lupulescu, M., Jercinovic, M., Chiarenzelli, J., Williams, M., Singer, J., and Bailey, D., 2019a, Age and Origin of Monazite Symplectite in an Iron Oxide-Apatite Deposit in the Adirondack Mountains, New York, USA: Implications for Tracking Fluid Conditions: Minerals, v. 9, p. 65, doi:10.3390/min9010065.

Regan, S.P., Walsh, G.J., Williams, M.L., Chiarenzelli, J.R., Toft, M., and McAleer, R., 2019b, Syn-collisional exhumation of hot middle crust in the Adirondack Mountains (New York, USA): Implications for extensional orogenesis in the southern Grenville province: Geosphere, v. 15, p. 1240–1261, doi:10.1130/GES02029.1.

Rey, P.F., Teyssier, C., Kruckenberg, S.C., and Whitney, D.L., 2011, Viscous collision in channel explains double domes in metamorphic core complexes: Geology, v. 39, p. 387–390, doi:10.1130/G31587.1.

Rey, P.F., Teyssier, C., and Whitney, D.L., 2009, The role of partial melting and extensional strain rates in the development of metamorphic core complexes: Tectonophysics, v. 477, p. 135–144, doi:10.1016/j.tecto.2009.03.010.

Rivers, T., 2015, Tectonic Setting and Evolution of the Grenville Orogen: An Assessment of Progress Over the Last 40 Years: Geoscience Canada, v. 42, p. 77–124, doi:10.12789/geocanj.2014.41.057.

Rivers, T., 2009, The Grenville Province as a large hot long-duration collisional orogen – insights from the spatial and thermal evolution of its orogenic fronts: Geological Society, London, Special Publications, v. 327, p. 405–444, doi:10.1144/SP327.17.

Rivers, T., 2012, Upper-crustal orogenic lid and mid-crustal core complexes: signature of a collapsed orogenic plateau in the hinterland of the Grenville Province (B. Murphy, Ed.): Canadian Journal of Earth Sciences, v. 49, p. 1–42, doi:10.1139/e11-014.

Rubatto, D., 2002, Zircon trace element geochemistry: partitioning with garnet and the link between U–Pb ages and metamorphism: Chemical Geology, v. 184, p. 123–138, doi:10.1016/S0009-2541(01)00355-2.

Santosh, M., Kusky, T., and Wang, L., 2011, Supercontinent cycles, extreme metamorphic processes, and changing fluid regimes: International Geology Review, v. 53, p. 1403–1423, doi:10.1080/00206814.2010.527682.

Sarkar, T., and Schenk, V., 2014, Two-stage granulite formation in a Proterozoic magmatic arc (Ongole domain of the Eastern Ghats Belt, India): Part 1. Petrology and pressure–temperature evolution: Precambrian Research, v. 255, p. 485–509, doi:10.1016/j.precamres.2014.07.026.

Sawyer, E.W., 2008, Atlas of Migmatites: Canadian Science Publishing, doi:10.1139/9780660197876.

Schiller, D., and Finger, F., 2019, Application of Ti-in-zircon thermometry to granite studies: problems and possible solutions: Contributions to Mineralogy and Petrology, v. 174, p. 51, doi:10.1007/s00410-019-1585-3.

Selleck, B.W., McLelland, J.M., and Bickford, M.E., 2005, Granite emplacement during tectonic exhumation: The Adirondack example: Geology, v. 33, p. 781, doi:10.1130/G21631.1.

Shinevar, W., Jagoutz, O., and VanTongeren, J., 2020, Gore mountain garnet amphibolite records UHT conditions: implications for the rheology of the lower continental crust during orogenesis, *in* p. 352783, doi:10.1130/abs/2020AM-352783.

Spear, F.S., and Markussen, J.C., 1997, Mineral Zoning, P-T-X-M Phase Relations, and Metamorphic Evolution of some Adirondack Granulites, New York: Journal of Petrology, v. 38, p. 757–783, doi:10.1093/petroj/38.6.757.

Stacey, J.S., and Kramers, J.D., 1975, Approximation of terrestrial lead isotope evolution by a two-stage model: Earth and Planetary Science Letters, v. 26, p. 207–221, doi:10.1016/0012-821X(75)90088-6.

Storm, L.C., and Spear, F.S., 2005, Pressure, temperature and cooling rates of granulite facies migmatitic pelites from the southern Adirondack Highlands, New York: Journal of Metamorphic Geology, v. 23, p. 107–130, doi:10.1111/j.1525-1314.2005.00565.x.

Suggate, S.M., and Hall, R., 2014, Using detrital garnet compositions to determine provenance: a new compositional database and procedure: Geological Society, London, Special Publications, v. 386, p. 373–393, doi:10.1144/SP386.8.

Touret, J.L.R., Santosh, M., and Huizenga, J.M., 2016, High-temperature granulites and supercontinents: Geoscience Frontiers, v. 7, p. 101–113, doi:10.1016/j.gsf.2015.09.001.

Valentino, D.W., Chiarenzelli, J.R., and Regan, S.P., 2019a, Spatial and temporal links between Shawinigan accretionary orogenesis and massif anorthosite intrusion, southern Grenville province, New York, U.S.A.: Journal of Geodynamics, v. 129, p. 80–97, doi:10.1016/j.jog.2018.04.001.

Valentino, D.W., Chiarenzelli, J.R., and Regan, S.P., 2019b, Spatial and temporal links between Shawinigan accretionary orogenesis and massif anorthosite intrusion, southern Grenville province, New York, U.S.A.: Journal of Geodynamics, v. 129, p. 80–97, doi:10.1016/j.jog.2018.04.001.

Valley, P.M., Hanchar, J.M., and Whitehouse, M.J., 2011, New insights on the evolution of the Lyon Mountain Granite and associated Kiruna-type magnetite-apatite deposits, Adirondack Mountains, New York State: Geosphere, v. 7, p. 357–389, doi:10.1130/GES00624.1.

Vanderhaeghe, O., 2009, Migmatites, granites and orogeny: Flow modes of partially-molten rocks and magmas associated with melt/solid segregation in orogenic belts: Tectonophysics, v. 477, p. 119–134, doi:10.1016/j.tecto.2009.06.021.

Vermeesch, P., 2018, IsoplotR: A free and open toolbox for geochronology: Geoscience Frontiers, v. 9, p. 1479–1493, doi:10.1016/j.gsf.2018.04.001.

Walsh, A.K., Kelsey, D.E., Kirkland, C.L., Hand, M., Smithies, R.H., Clark, C., and Howard, H.M., 2015, P–T–t evolution of a large, long-lived, ultrahigh-temperature Grenvillian belt in central Australia: Gondwana Research, v. 28, p. 531–564, doi:10.1016/j.gr.2014.05.012.

Waters, D.J., 2001, The significance of prograde and retrograde quartz-bearing intergrowth microstructures in partially melted granulite-facies rocks: Lithos, v. 56, p. 97–110, doi:10.1016/S0024-4937(00)00061-X.

Watson, E.B., and Harrison, T.M., 1983, Zircon saturation revisited: temperature and composition effects in a variety of crustal magma types: Earth and Planetary Science Letters, v. 64, p. 295–304, doi:10.1016/0012-821X(83)90211-X.

White, R.W., Holland, T.J.B., Powell, R., and Worley, B.A., 2000, The effect of TiO_2 and Fe_2O_3 on metapelitic assemblages at greenschist and amphibolite facies conditions: mineral equilibria calculations in the system K_2O-FeO-MgO-Al_2O_3-SiO_2-H_2O-TiO_2-Fe_2O_3: Journal of Metamorphic Geology, v. 18, p. 497–511, doi:10.1046/j.1525-1314.2000.00269.x.

White, R.W., Powell, R., and Clarke, G.L., 2002, The interpretation of reaction textures in Fe-rich metapelitic granulites of the Musgrave Block, central Australia: constraints from mineral equilibria calculations in the system K_2O-FeO-MgO-Al_2O_3-SiO_2-H_2O-TiO_2-Fe_2O_3: Reaction textures musgrave block granulites: Journal of Metamorphic Geology, v. 20, p. 41–55, doi:10.1046/j.0263-4929.2001.00349.x.

White, R.W., Powell, R., and Halpin, J.A., 2005, Spatially-focussed melt formation in aluminous metapelites from Broken Hill, Australia: Journal of Metamorphic Geology, v. 22, p. 825–845, doi:10.1111/j.1525-1314.2004.00553.x.

White, R.W., Powell, R., and Holland, T.J.B., 2007, Progress relating to calculation of partial melting equilibria for metapelites: Journal of Metamorphic Geology, v. 25, p. 511–527, doi:10.1111/j.1525-1314.2007.00711.x.

White, R.W., Powell, R., Holland, T.J.B., Johnson, T.E., and Green, E.C.R., 2014a, New mineral activity-composition relations for thermodynamic calculations in metapelitic systems: Journal of Metamorphic Geology, v. 32, p. 261–286, doi:10.1111/jmg.12071.

White, R.W., Powell, R., and Johnson, T.E., 2014b, The effect of Mn on mineral stability in metapelites revisited: new *a* - *x* relations for manganese-bearing minerals: Journal of Metamorphic Geology, v. 32, p. 809–828, doi:10.1111/jmg.12095.

Whitney, D.L., and Evans, B.W., 2010, Abbreviations for names of rock-forming minerals: American Mineralogist, v. 95, p. 185–187, doi:10.2138/am.2010.3371.

Whitney, D.L., Teyssier, C., and Vanderhaeghe, O., 2004, Gneiss domes and crustal flow: Gneiss domes in orogeny, v. 380, p. 15.

Williams, I.S., 1997, U-Th-Pb Geochronology by Ion Microprobe, *in* Applications of Microanalytical Techniques to Understanding Mineralizing Processes, Society of Economic Geologists, v. 7, p. 0, doi:10.5382/Rev.07.01.

Wong, M.S., Williams, M.L., McLelland, J.M., Jercinovik, M.J., and Kowalkoski, J., 2012, Late Ottawan extension in the eastern Adirondack Highlands: Evidence from structural studies and zircon and monazite geochronology: Geological Society of America Bulletin, v. 124, p. 857–869, doi:10.1130/B30481.1.

Appendix A: Kanaya-Okayama Ranges

If the electron beam probes an area within a grain that is further than its K-O range from another mineral, then the shade of gray there will be directly related to the average atomic number of that grain. However, if the beam probes a spot that is within its K-O range of another material, then the effective atomic number will be a combination of multiple minerals, and the Z-contrast at that location cannot be used to accurately identify a mineral. Edge effects also occur near grain boundaries where electrons are backscattered by the adjacent material causing brighter rims or absorbed by the adjacent material causing darker rims. Probing on cracks, voids or even boundaries between two minerals can cause a darker or lighter contrast as electrons are able to penetrate deep into the specimen before entering resulting fewer BSE arriving at the detector, or arrive at the material at near vertical angles causing more electrons to backscatter resulting in more BSE arriving at the detector.

Appendix B: Methodology for Zircon Analysis (from Metzger et al., in press)

U-Pb geochronology and trace element analyses of zircon were conducted on the Stanford-USGS SHRIMP-RG. Zircon grains were mounted in epoxy, polished, and imaged using cathodoluminescence (CL), backscattered electron (BSE) and scanning electron (SEM) microscopy to identify internal structure, inclusions and physical defects. Before SHRIMP analysis, CL and BSE images were used to identify different compositional zones within individual grains to be tested and areas with inclusions and cracks to be avoided. SEM images were used to identify physical defects in the "topography" of the mounts to avoid and flat areas to target. Grains were re-imaged after analysis to evaluate for errors with the beam spot location. The mounted grains were washed with a 1N HCl solution and thoroughly rinsed in distilled water, dried in a vacuum oven, and coated with gold prior to analysis. The mounts were stored at high pressure (10^{-7} torr) for several hours before being moved into the source chamber of the SHRIMP-RG to minimize degassing of the epoxy and isobaric hydride interferences and masses 204-208.

Secondary ions were sputtered from the target spot using an O_2-primary ion beam, which had an intensity varying from 2.0 to 2.3 nA. The primary ion beam spot had an ellipse-shape approximately 22 x 24 microns and a depth of ~1.0 micron for the analyses performed in this study. Before every analysis, the sample surface was cleaned by rastering the primary beam for 60 seconds, and the primary and secondary beams were auto-tuned to maximize transmission. The acquisition routine includes analysis of $^{30}Si^{16}O^+$, $^{48}Ti^+$, $^{49}Ti^+$, $^{56}Fe^+$, $^{89}Y^+$, 9-REE ($^{139}La^+$, $^{140}Ce^+$, $^{146}Nd^+$, $^{147}Sm^+$, $^{153}Eu^+$, $^{155}Gd^+$, $^{162}Dy^{16}O^+$, $^{166}Er^{16}O^+$, $^{172}Yb^{16}O^+$), a high mass normalizing species ($^{90}Zr_2{}^{16}O^+$), followed by $^{180}Hf^{16}O^+$, $^{204}Pb^+$, a background measured at 0.045 mass units above the $^{204}Pb^+$ peak, $^{206}Pb^+$, $^{207}Pb^+$, $^{208}Pb^+$, $^{232}Th^+$, $^{238}U^+$, $^{232}Th^{16}O^+$, and $^{238}U^{16}O^+$, $^{238}U^{16}O^{2+}$.

Trace element measurements (Ti, Fe, Y, Hf, REE) are measured briefly (typically 1 to 5 sec/mass) immediately before the geochronology peaks, and in mass order. For the first session, $^{232}Th+$ was not measured. All peaks are measured on a single EPT® discrete-dynode electron multiplier operated in pulse counting mode with 5 scans (peak-hopping cycles from mass 46 through 270). The counting times on each peak are varied according to the sample age and the U and Th concentrations to improve counting statistics and age precision. Measurements are made at mass resolutions of $M/\Delta M$ = 8600-9000 (10% peak height), which eliminate1s interfering molecular species, particularly for the REE.

Zircon concentration data for U, Th and all measured trace elements are calculated relative to MAD (4196 ppm U; Barth and Wooden, 2010). Calculated model ages for zircon are standardized relative to R33 (419 Ma; Black et al., 2004), which were analyzed repeatedly throughout the duration of the analytical session. Data reduction for geochronology follows the methods described by Williams (1997), and Ireland and Williams (2003), and uses the MS Excel add-in programs Squid2.51 and Isoplot3.764 of Ken Ludwig (2009, 2012). Calculations of weighted mean ages included in this paper used IsoplotR (Vermeesch, 2018).

The measured $^{206}Pb/^{238}U$ was corrected for common Pb using ^{207}Pb, whereas $^{207}Pb/^{206}Pb$ was corrected using ^{204}Pb. The common-Pb correction was based on a model Pb composition from Stacey and Kramers (1975). All reported $^{206}Pb/^{238}U$ and $^{207}Pb/^{206}Pb$ model ages and 18 uncertainties (2σ) include error summed in quadrature from the external reproducibility of the standard Temora-2 during an individual analytical session (~24 hours).

Data reduction for the trace element concentrations are performed in MS Excel. Average count rates of each element of interest are ratioed to $^{30}Si^{16}O$ to account for any primary current

drift, and the derived ratios for the unknowns are compared to an average of those for the standards to determine concentrations. Spot to spot precisions (as measured on the standards) vary according to elemental ionization efficiency and concentration. For the MADDER zircon, precisions generally range from about ±3% for Hf, ±5-10% for the Ti, Fe, Y and HREE, ±10-15%, and up to ±40% for La which is present most often at the ppb level (all values at 2σ; Coble et al., 2018).

Fe is naturally low in zircon (<~10 ppm). Trace element analyses with high concentrations of Fe (>~50 ppm) as well as high concentrations of Ti likely result from errors in measurement and were omitted from data analysis. In addition, high common Pb and topographical variation on zircon grains due to cracks or beam spots overlapping with inclusions were criteria used to omit unreliable analyses (age, compositional, temperature analyses from the same beam location) as these analyses do not accurately reflect the zircon composition.

The trace element composition of zircon is largely dependent on the other mineral phases present in the rock or melt at the time of crystallization and other factors like bulk rock chemistry, the pressure temperature relationships, and the tectonic setting of the rocks. I measured a set of rare earth elements (REEs) and Ti-in-zircons with the SHRIMP-RG. Measured trace element compositions were chondrite normalized using McDonough and Sun (1995). Normalized concentrations were plotted against atomic number on a spider diagram, to see compositional trends (enrichment/depletion, the steepness of positive or negative slopes or plateaus) or anomalous elemental concentrations. Rare earth element concentrations for zircon show enrichment in heavy rare earths (HREEs), suggesting post-peak metamorphic zircon growth without garnet. Zircon is typically depleted in light REEs (LREEs) and displays a

positive Ce anomaly and negative Eu anomaly relative to chondrite values typical for zircon (Rubatto, 2002; Hoskin and Schaltegger, 2003).

Th/U can be useful when distinguishing between igneous and metamorphic zircons, but should not be considered definitive. Igneous zircons are typically high Th/U (>0.1) while metamorphic are low Th/U (<0.1; Hoskin and Schaltegger, 2003). The Th/U ratios of zircon involved in this study agreed with the textural analysis; all the high Th/U oxides were in igneous zones and all low Th/U analyses were from metamorphic zones. The samples with complex zoning were low Th/U like the metamorphic zircon with the exception of one sample (HW006A-34.2, 1123±14 Ma), which is most likely is inherited magmatic zircon.

Appendix C: Ti-in-Zircon Thermometry Error Analysis

Standard Errors

Assuming t-values of 1.960 for two-tailed 95% confidence interval (α=0.5) then the standard errors for E and D are $S_{\bar{E}} = 86/1.960 = 44$ and $S_{\bar{D}} = 0.072/1.960 = 0.037$. Uncertainty for ^{48}Ti amounts are reported as ±10% (2 standard deviations) from the measured value. The standard error of the concentration of ^{48}Ti (P, in ppm) is estimated as:

$$\boldsymbol{S_{\bar{P}} = \frac{P*0.10}{2} = 0.05P} \qquad \text{[Equation 9]}$$

Standard error for the activity of rutile is:

$$\boldsymbol{S_{\overline{A_{TiO_2}}} = \frac{S_{A_{TiO_2}}}{\sqrt{N}}} \qquad \text{[Equation 10]}$$

Analytical Error Propagation through calculation of corrected temperatures

I propagate error through Equation 8 to determine standard error of the corrected temperatures ($S_{\overline{T_c}}$) using a generalized first order approximation:

$$S_{\overline{T_c}} = \sqrt{\begin{array}{c}\left(\frac{\partial T_c}{\partial E}S_{\bar{E}}\right)^2 + \left(\frac{\partial T_c}{\partial P}S_{\bar{P}}\right)^2 + \left(\frac{\partial T_c}{\partial D}S_{\bar{D}}\right)^2 + \left(\frac{\partial T_c}{\partial A_{TiO_2}}S_{\overline{A_{TiO_2}}}\right)^2 \\ +2\frac{\partial T_c}{\partial E}S_{\bar{E}}\left(\frac{\partial T_c}{\partial P}S_{\bar{P}}r_{E,P} + \frac{\partial T_c}{\partial D}S_{\bar{D}}r_{E,D} + \frac{\partial T_c}{\partial A_{TiO_2}}S_{\overline{A_{TiO_2}}}r_{E,A_{TiO_2}}\right) \\ +2\frac{\partial T_c}{\partial P}S_{\bar{P}}\left(\frac{\partial T_c}{\partial D}S_{\bar{D}}r_{P,D} + \frac{\partial T_c}{\partial A_{TiO_2}}S_{\overline{A_{TiO_2}}}r_{P,A_{TiO_2}}\right) \\ +2\frac{\partial T_c}{\partial D}S_{\bar{D}}\left(\frac{\partial T_c}{\partial A_{TiO_2}}S_{\overline{A_{TiO_2}}}r_{D,A_{TiO_2}}\right)\end{array}} \qquad \text{[Equation 11]}$$

where r terms are Pearson's correlation, given in general form as:

$$r_{x,y} = \frac{\sum[(x-\bar{x})(y-\bar{y})]}{\sum(x-\bar{x})^2\sum(y-\bar{y})^2\,]} \qquad \text{[Equation 12]}$$

Terms E and D are given as constants with error (Ferry and Watson, 2007) so I do not have individual measurements of E or D in $(E-\bar{E})$ or $(D-\bar{D})$ terms. My estimate for Pearson's correlation correlated terms containing E or D is zero. Therefore Equation 11 becomes

$$S_{\overline{T_c}} =$$

$$\sqrt{\left(\frac{\partial T_c}{\partial E} S_{\overline{E}}\right)^2 + \left(\frac{\partial T_c}{\partial P} S_{\overline{P}}\right)^2 + \left(\frac{\partial T_c}{\partial D} S_{\overline{D}}\right)^2 + \left(\frac{\partial T_c}{\partial A_{TiO_2}} S_{\overline{A_{TiO_2}}}\right)^2 + 2\frac{\partial T_c}{\partial P} S_{\overline{P}} \left(\frac{\partial T_c}{\partial A_{TiO_2}} S_{\overline{A_{TiO_2}}} r_{P,A_{TiO_2}}\right)}$$ [Equation 13]

where

$$r_{P,A_{TiO_2}} = \frac{\sum[(P-\bar{P})(A_{TiO_2}-\overline{A_{TiO_2}})]}{\sum(P-\bar{P})^2 \sum(A_{TiO_2}-\overline{A_{TiO_2}})^2}$$ [Equation 14]

Partial derivative calculations:

To make calculations of partial derivates neater I define the following:

$$f(T_o, P, A_{SiO_2}, D) = \left(\log_{10} P + \frac{kA_{TiO_2}}{T_o} - D\right)^{-1}$$ [Equation 15]

and Equation 8 can be rewritten as:

$$T_c = E \bullet f$$ [Equation 16]

$\frac{\partial T_c}{\partial E}$ calculation

By application of the product rule for derivatives

$$\frac{\partial T_c}{\partial E} = E \bullet \frac{\partial f}{\partial E} + \frac{\partial E}{\partial E} \bullet f = E \bullet \frac{\partial f}{\partial E} + f$$ [Equation 17]

The partial derivative of f with respect to E is:

$$\frac{\partial f}{\partial E} = \left(\log_{10} P + \frac{kA_{TiO_2}}{T_o} - D\right)^{-2} \bullet KA_{TiO_2} T_o^{-2} * \frac{\partial T_o}{\partial E}$$ [Equation 18]

Recall from Equation 3: $T_o = \frac{E}{\log_{10} P - D}$, and the partial derivative of T_o with respect to E is:

$$\frac{\partial T_o}{\partial E} = \frac{1}{\log_{10} P - D} \quad \text{[Equation 19]}$$

Substituting Equation 18 into Equation 17 gives:

$$\frac{\partial f}{\partial E} = \left(\log_{10} P + \frac{kA_{TiO_2}}{T_o} - D\right)^{-2} \bullet \frac{kA_{TiO_2}}{T_o^2} \bullet \frac{1}{\log_{10} P - D} = \left(\log_{10} P + \frac{kA_{TiO_2}}{T_o} - D\right)^{-2} \bullet \frac{kA_{TiO_2}}{T_o^2} \bullet \frac{T_o}{E} = \frac{kA_{TiO_2}}{T_o E\left(\log_{10} P + \frac{kA_{TiO_2}}{T_o} - D\right)^2} \quad \text{[Equation 20]}$$

Substituting Equation 19 and 14 into Equation 16, followed by substitution of Equation 3 gives:

$$\boldsymbol{\frac{\partial T_c}{\partial E} = \frac{kA_{TiO_2}}{\left(\frac{E}{\log_{10} P - D}\right)\left(\log_{10} P + \frac{kA_{TiO_2}}{\left(\frac{E}{\log_{10} P - D}\right)} - D\right)^2} + \frac{1}{\log_{10} P + \frac{kA_{TiO_2}}{\left(\frac{E}{\log_{10} P - D}\right)} - D}} \quad \text{[Equation 21]}$$

Other partial derivates are determined as follows with detailed steps outlined at the end of Appendix C:

$$\boldsymbol{\frac{\partial T_c}{\partial D}} = \frac{(E - kA_{TiO_2})}{\left(\log_{10} P + \frac{kA_{TiO_2}}{\left(\frac{E}{\log_{10} P - D}\right)} - D\right)^2} \quad \text{[Equation 22]}$$

$$\boldsymbol{\frac{\partial T_c}{\partial P}} = -\frac{E + kA_{TiO_2}}{P ln(10)\left(\log_{10} P + \frac{kA_{TiO_2}}{\left(\frac{E}{log_{10} P - D}\right)} - D\right)^2} \quad \text{[Equation 23]}$$

$$\frac{\partial T_c}{\partial A_{TiO_2}} = \frac{-k}{\left(\frac{1}{\log_{10} P - D}\right)\left(\log_{10} P + \frac{kA_{TiO_2}}{\left(\frac{E}{\log_{10} P - D}\right)} - D\right)^2} \quad \text{[Equation 24]}$$

Error Analysis

Total standard error $\boldsymbol{S_{\bar{T}}}$ (Equation 13) is calculated using JMP statistical modeling software (JMP, 2019) using Equations 21 – 24, he determined standard errors from literature for $S_{\bar{E}}$ and $S_{\bar{D}}$ (Ferry and Watson, 2007), the calculated standard error from reported standard deviations for $S_{\bar{P}}$ (Equation 9; Metzger et al., in review), the calculated standard error from

modeled affinities of rutile (Equation 10), and Pearson's correlation between P and $\boldsymbol{A_{TiO_2}}$(Equation 14).

Table 7 provides a summary of error analysis for each term and the total percent contribution to error for each term E, D, P, and A_{TiO2}. E and D are values reported in literature (Ferry and Watson, 2007; Schiller and Finger, 2019) and account for 48% and 36% of the error respectively and 84% of the error collectively. The amount of ^{48}Ti accounts for 13% of the error, and the activity of rutile accounts for 3% of the error. These results are significant because most of the error is coming from reported values in literature rather than the seemingly highly variable measured terms A_{TiO2} and P. The most effective way to reduce uncertainty in Ti-in-zircon temperatures is to improve the experimental design of the Watson and Harrison (1983) zircon saturation experiments.

Monte Carlo Simulations to evaluate $S_{\overline{T_c}}$

Monte Carlo simulations randomly select values from normal distributions of variables to simulate the variability in a calculation. Random normal distributions with $N = 10^5$ of E, D, P, and $A_{TiO_2}$and standard deviations equal to the determined standard errors were generated and values were randomly assigned to Equation 4 for T_c using JMP statistical modeling software (*JMP*, 2019). The standard deviation of T_c in the Monte Carlo simulation should agree with the analytical standard error for T_C (Equation 13). I also run simulations where only one term varies while all others are help constant. The standard deviation of the distributions for each temperature calculated with only one varied term should agree with uncorrelated terms from Equation 13 ($\frac{\partial T_c}{\partial E} S_{\overline{E}}$, $\frac{\partial T_c}{\partial P} S_{\overline{P}}$, $\frac{\partial T_c}{\partial D} S_{\overline{D}}$, and $\frac{\partial T_c}{\partial A_{TiO_2}} S_{\overline{A_{TiO_2}}}$). Monte Carlo simulated values and the analytical results are within <0.7% of each other.

Table 7: Summary of Sensitivities of T_c, Error, and Percentage of Error Contributions.

Spot Name	Sensitivity of T_c to terms				Pearson's Corr.	Uncorrelated Errors				Correlated Error	Total Error[2]	Percentage of error contribution from each term.			
	$\frac{\partial T_c}{\partial E}$	$\frac{\partial T_c}{\partial D}$	$\frac{\partial T_c}{\partial P}$	$\frac{\partial T}{\partial A}$	$r_{P,A_{TiO_2}}$	$\left(\frac{\partial T}{\partial E}S_{\bar{E}}\right)^2$	$\left(\frac{\partial T_c}{\partial D}S_{\bar{D}}\right)^2$	$\left(\frac{\partial T_c}{\partial P}S_{\bar{P}}\right)^2$	$\left(\frac{\partial T}{\partial A}S_{\overline{A_{TiO_2}}}\right)^2$	$2\frac{\partial T_c}{\partial P}\overline{S_P}\frac{\partial T_c}{\partial A_{TiO_2}}S_{\overline{A_{TiO_2}}}r_{P,A_{TiO_2}}$	$S_{\bar{T}_c}^2$	**E%**	**D%**	**P%**	**A%**
HW001-1.1	0.223	-242.726	6.337	0.012	5.6E-05	95.79	79.50	28.67	4.58	0.00	209	**46**	**38**	**14**	**2**
HW005A-19.1	0.222	-241.194	6.485	0.012	3.1E-04	95.24	78.50	28.28	4.45	0.01	206	**46**	**38**	**14**	**2**
HW005A-9.1	0.213	-220.309	9.300	0.011	6.8E-05	87.40	65.50	23.39	3.74	0.00	180	**49**	**36**	**13**	**2**
HW005B-37.1	0.213	-219.454	9.442	0.011	4.9E-05	87.08	64.99	23.19	1.61	0.00	177	**49**	**37**	**13**	**1**
HW006A-34.2	0.215	-223.447	8.670	0.011	-2.0E-04	88.76	67.38	23.99	3.56	0.00	184	**48**	**37**	**13**	**2**
HW006A-36.2	0.211	-216.930	9.913	0.011	2.7E-05	86.12	63.50	22.64	1.30	0.00	174	**50**	**37**	**13**	**1**
HW006B-30.1	0.224	-244.847	6.143	0.012	2.2E-05	96.54	80.90	29.22	4.74	0.00	211	**46**	**38**	**14**	**2**
HW006B-8.1	0.244	-307.192	3.318	0.015	1.4E-07	114.78	127.34	50.43	7.53	0.00	300	**38**	**42**	**17**	**3**
HW008A-2.1	0.208	-209.693	11.491	0.011	1.2E-05	83.31	59.34	21.13	0.65	0.00	164	**51**	**36**	**13**	**0**
HW001-33.1	0.212	-225.589	10.337	0.012	-6.1E-06	86.28	68.67	26.18	19.36	0.00	201	**43**	**34**	**13**	**10**
HW004-10.1	0.208	-209.212	11.609	0.011	1.1E-05	83.12	59.06	21.03	0.62	0.00	164	**51**	**36**	**13**	**0**
HW004-13.1	0.211	-215.623	10.169	0.011	2.2E-05	85.62	62.74	22.36	1.12	0.00	172	**50**	**37**	**13**	**1**
HW004-24.1	0.210	-212.952	10.733	0.011	1.6E-05	84.58	61.20	21.80	0.88	0.00	168	**50**	**36**	**13**	**1**
HW004-27.1	0.211	-224.652	10.502	0.012	-5.3E-06	85.97	68.10	25.94	19.26	0.00	199	**43**	**34**	**13**	**10**
HW005A-10.1	0.211	-216.070	10.083	0.011	2.4E-05	85.79	63.00	22.46	1.22	0.00	172	**50**	**37**	**13**	**1**
HW005A-24.1	0.214	-221.485	9.088	0.011	1.2E-04	87.86	66.20	23.64	1.87	0.00	180	**49**	**37**	**13**	**1**
HW005A-6.1	0.208	-210.169	11.375	0.011	1.2E-05	83.49	59.61	21.22	0.67	0.00	165	**51**	**36**	**13**	**0**
HW005B-15.1	0.209	-211.116	11.152	0.011	1.3E-05	83.86	60.14	21.42	0.77	0.00	166	**50**	**36**	**13**	**0**
HW005B-3.1	0.210	-212.952	10.733	0.011	1.6E-05	84.58	61.20	21.80	0.88	0.00	168	**50**	**36**	**13**	**1**
HW005B-34.1	0.210	-213.412	10.635	0.011	1.7E-05	84.76	61.46	21.89	0.95	0.00	169	**50**	**36**	**13**	**1**
HW005B-9.1	0.214	-221.485	9.088	0.011	1.2E-04	87.86	66.20	23.64	1.87	0.00	180	**49**	**37**	**13**	**1**
HW006A-34.1	0.212	-225.168	10.423	0.012	-5.7E-06	86.12	68.42	26.08	19.33	0.00	200	**43**	**34**	**13**	**10**
HW006A-36.1	0.209	-211.116	11.152	0.011	1.3E-05	83.86	60.14	21.42	16.36	0.00	182	**46**	**33**	**12**	**9**
HW006B-31.1	0.211	-224.652	10.502	0.012	-5.3E-06	85.97	68.10	25.94	19.26	0.00	199	**43**	**34**	**13**	**10**
HW006B-33.1	0.213	-220.675	9.225	0.011	7.7E-05	87.55	65.71	23.46	1.74	0.00	178	**49**	**37**	**13**	**1**
HW007A-1.1	0.214	-222.252	8.856	0.011	3.1E-04	88.32	66.66	23.72	3.41	0.01	182	**48**	**37**	**13**	**2**
HW007A-14.1	0.216	-227.341	8.115	0.012	-4.2E-05	90.17	69.74	24.91	17.69	0.00	203	**45**	**34**	**12**	**9**
HW007A-19.1	0.217	-228.069	8.012	0.012	-3.7E-05	90.45	70.19	25.08	4.10	0.00	190	**48**	**37**	**13**	**2**
HW007A-24.1	0.213	-220.675	9.225	0.011	7.7E-05	87.55	65.71	23.46	1.74	0.00	178	**49**	**37**	**13**	**1**
HW007A-28.1	0.209	-211.582	11.044	0.011	1.4E-05	84.05	60.41	21.51	0.79	0.00	167	**50**	**36**	**13**	**0**
HW007A-29.1	0.217	-229.169	7.865	0.012	-3.3E-05	90.85	70.87	25.34	4.22	0.00	191	**47**	**37**	**13**	**2**
HW007A-3.1	0.212	-225.168	10.423	0.012	-5.7E-06	86.12	68.42	26.08	19.33	0.00	200	**43**	**34**	**13**	**10**
HW007A-35.1	0.208	-210.169	11.375	0.011	1.2E-05	83.49	59.61	21.22	0.67	0.00	165	**51**	**36**	**13**	**0**
HW007A-8.1	0.213	-220.267	9.296	0.011	6.5E-05	87.40	65.47	23.37	1.68	0.00	178	**49**	**37**	**13**	**1**
HW007B-1.1	0.209	-212.504	10.835	0.011	1.5E-05	84.41	60.94	21.71	0.88	0.00	168	**50**	**36**	**13**	**1**
HW007B-1.2	0.211	-215.197	10.259	0.011	2.1E-05	85.45	62.49	22.27	16.70	0.00	187	**46**	**33**	**12**	**9**
HW007B-13.1	0.214	-222.252	8.856	0.011	3.1E-04	88.32	66.66	23.72	3.41	0.01	182	**48**	**37**	**13**	**2**
HW007B-18.1	0.213	-219.874	9.370	0.011	5.7E-05	87.24	65.24	23.28	1.68	0.00	177	**49**	**37**	**13**	**1**
HW007B-19.1	0.214	-222.252	8.856	0.011	3.1E-04	88.32	66.66	23.72	3.41	0.01	182	**48**	**37**	**13**	**2**
HW007B-2.1	0.213	-220.675	9.225	0.011	7.7E-05	87.55	65.71	23.46	1.74	0.00	178	**49**	**37**	**13**	**1**
HW007B-23.1	0.213	-219.874	9.370	0.011	5.7E-05	87.24	65.24	23.28	1.68	0.00	177	**49**	**37**	**13**	**1**
HW007B-24.2	0.211	-224.224	10.591	0.012	-5.0E-06	85.80	67.84	25.84	19.22	0.00	199	**43**	**34**	**13**	**10**
HW007B-26.1	0.216	-227.341	8.115	0.012	-4.2E-05	90.17	69.74	24.91	17.69	0.00	203	**45**	**34**	**12**	**9**
HW007B-3.1	0.213	-220.267	9.296	0.011	6.5E-05	87.40	65.47	23.37	1.68	0.00	178	**49**	**37**	**13**	**1**
HW008A-10.1	0.208	-209.693	11.491	0.011	1.2E-05	83.31	59.34	21.13	0.64	0.00	164	**51**	**36**	**13**	**0**
HW008A-25.1	0.210	-213.862	10.538	0.011	1.7E-05	84.93	61.72	21.99	0.99	0.00	170	**50**	**36**	**13**	**1**
HW008A-3.1	0.216	-226.177	8.271	0.012	-5.0E-05	89.76	69.03	24.63	3.88	0.00	187	**48**	**37**	**13**	**2**
HW008A-5.1	0.217	-228.452	7.963	0.012	-3.6E-05	90.58	70.43	25.17	4.16	0.00	190	**48**	**37**	**13**	**2**
HW008B-19.1	0.213	-219.874	9.370	0.011	5.7E-05	87.24	65.24	23.28	1.68	0.00	177	**49**	**37**	**13**	**1**
HW008B-2.1	0.215	-223.837	8.610	0.011	-1.3E-04	88.90	67.61	24.08	3.61	0.00	184	**48**	**37**	**13**	**2**
HW008B-25.1	0.216	-226.952	8.166	0.012	-4.4E-05	90.04	69.51	24.81	3.99	0.00	188	**48**	**37**	**13**	**2**
HW008B-32.1	0.214	-222.252	8.856	0.011	3.1E-04	88.32	66.66	23.72	3.41	0.01	182	**48**	**37**	**13**	**2**
HW008B-39.1	0.216	-225.785	8.325	0.012	-5.4E-05	89.62	68.79	24.54	3.83	0.00	187	**48**	**37**	**13**	**2**
mean	0.214	-222.607	9.405	0.012	3.9E-05	87.84	24.24	67.14	5.40	0.001	185	**48**	**36**	**13**	**3**

Sensitivity calculations

Calculation of $\frac{\partial T_c}{\partial D}$

$$T_c = E * f$$

$$\frac{\partial T_c}{\partial D} = E * \frac{df}{dD}$$

$$\frac{\partial f}{\partial D} = -\frac{1}{\left(\log_{10} P + \frac{kA_{TiO_2}}{T_o} - D\right)^2} * \left(-\frac{kA_{TiO_2}}{T_o^2} * \frac{\partial T_o}{\partial D} - 1\right)$$

$$T_o = \frac{E}{\log_{10} P - D}$$

$$\frac{\partial T_o}{\partial D} = \frac{-E}{(\log_{10} P - D)^2}$$

$$\frac{\partial f}{\partial D} = -\frac{1}{\left(\log_{10} P + \frac{kA_{TiO_2}}{T_o} - D\right)^2} * \left(-\frac{kA_{TiO_2}}{T_o^2} * \frac{-E}{(\log_{10} P - D)^2} - 1\right)$$

$$\frac{\partial f}{\partial D} = -\frac{\left(\frac{kA_{TiO_2}}{E} - 1\right)}{\left(\log_{10} P + \frac{kA_{TiO_2}}{\left(\frac{E}{\log_{10} P - D}\right)} - D\right)^2}$$

$$\boldsymbol{\frac{\partial T_c}{\partial D}} = \frac{(E - kA_{TiO_2})}{\left(\log_{10} P + \frac{kA_{TiO_2}}{\left(\frac{E}{\log_{10} P - D}\right)} - D\right)^2}$$

Calculation of $\frac{\partial T_c}{\partial P}$

$$\boldsymbol{T_c = E * f}$$

$$\frac{\partial T_c}{\partial P} = E * \frac{\partial f}{\partial P}$$

$$\boldsymbol{\frac{\partial f}{\partial P} = -\left(log_{10} P + \frac{kA_{TiO_2}}{T_o} - D\right)^{-2} * \left(\frac{1}{Pln(10)} - \frac{kA_{TiO_2}}{T_o^2} * \frac{\partial T_o}{\partial P}\right)}$$

$$\boldsymbol{T_o = \frac{E}{log_{10} P - D}}$$

$$\boldsymbol{\frac{\partial T_o}{\partial P} = -\frac{E}{(log_{10} P - D)^2}\left(\frac{1}{P ln(10)}\right) = \frac{-E}{(log_{10} P - D)^2 * P * ln(10)}}$$

$$\frac{\partial f}{\partial P} = -\left(\log_{10} P + \frac{kA_{TiO_2}}{T_o} - D\right)^{-2} * \left(\frac{1}{Pln(10)} - \frac{kA_{TiO_2}}{T_o^2} * \frac{-E}{(log_{10} P - D)^2 * P * ln(10)}\right)$$

$$= -\frac{1}{\left(\log_{10} P + \frac{kA_{TiO_2}}{T_o} - D\right)^2}\left(\frac{1}{Pln(10)} + \frac{kA_{TiO_2}}{T_o (log_{10} P - D) P\, ln(10)}\right)$$

$$\frac{\partial T_c}{\partial P} = -\frac{\mathrm{E}}{\left(\log_{10} P + \frac{kA_{TiO_2}}{T_o} - D\right)^2}\left(\frac{1}{Pln(10)} + \frac{kA_{TiO_2}}{T_o (log_{10} P - D) P\, ln(10)}\right)$$

$$\frac{\partial T_c}{\partial P} = -\frac{E + kA_{TiO_2}}{Pln(10)\left(\log_{10} P + \frac{kA_{TiO_2}}{\left(\frac{E}{log_{10} P - D}\right)} - D\right)^2}$$

Calculation of $\frac{\partial T_c}{\partial A_{TiO_2}}$

$$T_c = E * f$$

$$\frac{\partial T_c}{\partial A_{TiO_2}} = E * \frac{df}{dA_{TiO_2}}$$

$$\frac{df}{dA_{TiO_2}} = -\frac{k}{T_o\left(\log_{10} P + \frac{kA_{TiO_2}}{T_o} - D\right)^2}$$

$$\frac{\partial T_c}{\partial A_{TiO_2}} = \frac{-k}{\left(\frac{1}{\boldsymbol{\log_{10} P - D}}\right)\left(\log_{10} P + \frac{kA_{TiO_2}}{\left(\frac{E}{\boldsymbol{\log_{10} P - D}}\right)} - D\right)^2}$$